Design of a Robot for Gait Rehabilitation

ARCHIVES
MASSACHUSETTS INSTITUTE OF TECHNOLOGY
MAY 0 1 2009
LIBRARIES

by

Caitlyn Joyce Bosecker

B.S., Mechanical Engineering (2006)

Northeastern University

Submitted to the Department of Mechanical Engineering in Partial Fulfillment of the Requirements for the Degree of Master of Science in Mechanical Engineering

at the

Massachusetts Institute of Technology

February 2009

© 2009 Massachusetts Institute of Technology
All rights reserved

Signature of Author.....
Department of Mechanical Engineering
January 16, 2008

Certified by.....
Hermano Igo Krebs
Principle Research Scientist and Lecturer
Thesis Supervisor

Accepted by.....
David E. Hardt
Professor and Graduate Officer
Department of Mechanical Engineering

Design of a Robot for Gait Rehabilitation

by

Caitlyn Joyce Bosecker

Submitted to the Department of Mechanical Engineering
on January 16, 2009 in Partial Fulfillment of the Requirements for the
Degree of Master of Science in Mechanical Engineering

Abstract

The ability to walk is important for independent living and when this capacity is affected by injury, gait therapy is the traditional approach to re-train the nervous system, to re-build muscle strength, to improve balance, and to re-train kinematics in order to reduce the stresses applied to bones and muscles. The importance of this problem is illustrated by the approximately 5.8 million stroke survivors alive in the US today and an estimated 700,000 strokes occurring each year. In fact, for stroke survivors with mild to moderate impairment, only 37% regain the ability to walk within one week post-stroke and 73% fall within the first six months. Falls are a leading cause of injury among Americans over 65 years old with over one third of this population experiencing a fall each year and an unsteady gait increases this risk. This growing population will require gait therapy.

This thesis presents the design, development, fabrication, and proof-of-concept testing for a novel device to deliver gait therapy. While robotic devices exist, none of them take advantage of the concept of passive walkers and most focus on reproducing gait kinematics for impaired patients. Yet research has found that appropriate neural input is an important factor in efficacious therapy. For gait, this input would be the collision between the foot and the ground at heel-strike. The goal of this novel device is to allow patients to begin gait therapy before they are able to independently walk overground while maximizing the amount interface driven neural input during stepping in a safe environment.

Thesis Supervisor: Hermano Igo Krebs
Title: Principle Research Scientist and Lecturer, Mechanical Engineering

Table of Contents

1 Chapter 1: Introduction 8
1.1 Motivation 8
1.2 Thesis Overview 8
2 Chapter 2: Background 10
2.1 Stroke and Spinal Cord Injury 10
2.2 Gait Basics 11
2.2.1 Gait Kinematics 12
2.2.2 Pathological Gait 14
2.3 Central Pattern Generator 19
2.4 Gait Therapy 20
2.4.1 Physiotherapy 21
2.4.2 Robotic Therapy 22
3 Chapter 3: Design Concepts and Selection 30
3.1 TRIZ – Theory of Inventive Problem Solving 31
3.2 K'nex Proof-of-Concept 32
3.3 Functional Requirements 33
3.3.1 Treadmill 36
3.3.2 Body Weight Support 39
3.4 Actuation Design 40
3.4.1 Lead and Ball Screws 40
3.4.2 Lever 42
3.4.3 Cam 43
3.4.4 Hydraulic Actuator with Return Spring 44
3.4.5 Hydraulic Bi-Directional Actuator 46
3.4.6 Pneumatic Bi-Directional Actuator 46
3.4.7 Linear Actuator 47
3.5 Cam vs. Hydraulic Actuation 48
3.5.1 Cam Design Requirements 48
3.5.2 Hydraulic System Requirements 50
3.6 Body Weight Support System 55
4 Chapter 4: Detailed Design and Device Assembly 58
4.1 Cam Design 58
4.1.1 Cam Profile Development 59
4.1.2 Pressure Angle 68
4.1.3 Cam Surface Coordinates 70
4.2 Camshaft Material Selection 73
4.3 Camshaft Bearing Selection 75
4.3.1 Ball Bearings 75
4.3.2 Angular Contact Bearings 76
4.3.3 Cylindrical Roller Bearings 76
4.3.4 Needle Roller Bearings 77
4.3.5 Tapered Roller Bearings 77
4.4 Full Cam System 79
4.5 Treadmill Modifications 81

4.6 Body Weight Support (BWS) Design 82
4.6.1 BWS Frame 82
4.6.2 BWS Subject Interface 86
5 Chapter 5: Device Troubleshooting and Healthy Subject Testing 92
5.1 Motor Gear Reduction 92
5.2 Treadmill Speed Reduction 94
5.3 Fully Assembled System 96
5.4 Healthy Subject Testing 98
5.4.1 Electromyography 98
5.4.2 Healthy Subject Test Results 101
5.4.3 Mannequin Testing 108
6 Chapter 6: Conclusions 112
6.1 Project Evaluation 112
6.2 Future Work 112
References 115
Appendix A 119
Appendix B: Kinematic Robot-Based Evaluation Scales and Clinical Counterparts to Measure Upper Limb Motor Performance in Patients with Chronic Stroke 128
B1 Introduction 128
B2 Methods 129
B3 Results 134
B4 Discussion 138
B5 Investigating Shoulder/Elbow Score of the Fugl-Meyer Assessment 140
B6 Principle Component Analysis 142
Appendix B References 145
Appendix C: MRI-Compatible Wrist Robot: Seal Redesign and Phantom Testing 148
C1 Internal Leakage Troubleshooting 148
C2 Seal Redesign 151
C3 Leakage and Friction Testing 154
C4 Phantom Testing 158
C5 Conclusions 162
Appendix C References 164

List of Figures

Figure 2-1. Spinal cord levels and corresponding function. 11
Figure 2-2. Normal human gait cycle at about 3 ft/sec (1 m/sec) [5]. 12
Figure 2-3. Anatomical planes of the human body (axial also known as the frontal plane). 12
Figure 2-4. Trajectory of hip movement during gait. 13
Figure 2-5. Trajectory of hip and knee during gait (side view). 13
Figure 2-6. Anterior trunk bending. 15
Figure 2-7. Posterior trunk bending. 16
Figure 2-8. Circumduction. 16
Figure 2-9. Hip hiking. 17
Figure 2-10. Steppage. 18
Figure 2-11. Vaulting. 18
Figure 2-12. Golgi tendon organ. 20
Figure 2-13. LiteGait, a) coupled with a treadmill, b) for overground training. 24
Figure 2-14. Gait Trainer I. 25
Figure 2-15. Haptic Walker. 26
Figure 2-16. KineAssist™. 27
Figure 2-17. Lokomat®. 28
Figure 3-1. Two-legged passive walker [34]. 30
Figure 3-2. K'nex scaled proof-of-concept, a) system with 12" mannequin, b) close-up of treadmill concept. 33
Figure 3-3. Anthropometrics a) 99% Male, b) 1% Female [37]. 35
Figure 3-4. Foot clearance and time requirements for treadmill actuation. 36
Figure 3-5. Angles during a healthy gait cycle at about 3.3 ft/sec of, a) the hip, b) knee, and c) ankle. 37
Figure 3-6. a) BowFlex® TreadClimber®, b) TreadClimber® in Use. 38
Figure 3-7. Lead screw example. 40
Figure 3-8. Ball screw. 41
Figure 3-9. Lead screw design configuration. 41
Figure 3-10. Lead screw jamming under a moment load. 41
Figure 3-11. Lead screw configuration to reduce overturning load. 42
Figure 3-12. Mechanical advantage of a lever. 42
Figure 3-13. Lever design concept. 43
Figure 3-14. Cam design concept, a) cam design side view, b) front view. 44
Figure 3-15. Hydraulic actuator with return spring. 45
Figure 3-16. Bi-directional hydraulic actuator. 46
Figure 3-17. Bi-directional pneumatic actuator. 46
Figure 3-18. Linear actuators. 47
Figure 3-19. Determining required camshaft speed from stride length. 48
Figure 3-20. Motor torque/speed curve. 50
Figure 3-21. Device to test the mechanics of running under simulated low gravity [41]. 56
Figure 3-22. Honda leg assist device. 56
Figure 4-1. a) Radial Cam, b) Axial Cam [39]. 58
Figure 4-2. Timing Diagram for Both Treadmills. 60
Figure 4-3. Naïve cam SVAJ diagram [39]. 60

Figure 4-4. Double-Dwell cycloidal position SVAJ diagram. 62
Figure 4-5. Single-Dwell cycloidal position SVAJ diagram. 63
Figure 4-6. Single-Dwell double harmonic SVAJ diagram. 65
Figure 4-7. Single-Dwell polynomial SVAJ diagram. 67
Figure 4-8. Cycloidal, double harmonic, and polynomial position functions. 67
Figure 4-9. Prime radius for a cam roller follower [39]. 68
Figure 4-10. Pressure angle of an oscillating roller follower [39]. 69
Figure 4-11. Pressure angle for a cam with R_p = 5.75 inches. 70
Figure 4-12. Cam profile of an oscillating roller follower [39]. 71
Figure 4-13. Cam surface coordinates. 72
Figure 4-14. Loading of camshaft. 73
Figure 4-15. a) Conrad ball bearing, b) filling slot ball bearing [46]. 75
Figure 4-16. Angular contact bearing. 76
Figure 4-17. Cylindrical roller bearing [46]. 77
Figure 4-18. Needle roller bearing [46]. 77
Figure 4-19. a) cone geometry of tapered roller bearing, b) tapered roller bearing cone, c) cup. 78
Figure 4-20. Method for preloading tapered roller bearings [47]. 78
Figure 4-21. Cam system for treadmill actuation. 79
Figure 4-22. Detail of bearing pre-load design. 80
Figure 4-23. Assembled cam subsystem. 80
Figure 4-24. Treadmill height modification. 81
Figure 4-25. Treadmill motor height modification. 81
Figure 4-26. 80/20, 3030 aluminum extrusion, a) front view and dimensions, b) isometric view [48]. 82
Figure 4-27. BWS frame, a) front view, b) side view, c) isometric view. 83
Figure 4-28. BWS frame base member bending, a) location of beam in frame, b) force diagram. 84
Figure 4-29. BWS subject interface attachment member bending, a) location of beam in frame, b) force diagram. 84
Figure 4-30. BWS frame cross member bending, a) location of beam in frame, b) force diagram. 85
Figure 4-31. BWS frame column buckling, a) location of beam in frame, b) force diagram. 85
Figure 4-32. a) body weight support subject interface, b) subject harness. 86
Figure 4-33. a) loading on bicycle seat, b) diagram of cantilever bending. 87
Figure 4-34. Added BWS vertical stability, a) side view, b) detailed view. 88
Figure 4-35. Vertical DOF in bicycle seat, a) bicycle seat, b) cross-sectional view of nesting pipes. 88
Figure 4-36. Vertical DOF in upper body support, a) upper body support, b) cross-sectional view of nesting pipes. 89
Figure 4-37. BWS pelvic rotation degree of freedom. 90
Figure 4-38. Back support, a) front view, b) vertical back support, and c) back support at 20°. 90
Figure 5-1. 20:1 ratio gear reducer. 93
Figure 5-2. Camshaft gear reduction, a) side view, b) top view. 94
Figure 5-3. Schematic of pulley reduction and belt length. 95
Figure 5-4. Treadmill pulley, a) original 4.3:1 reduction, b) modified 6:1 reduction 96
Figure 5-5. Model of full system. a) side view, b) front view 97

Figure 5-6. Fully assembled system, a) front view, b) side view. 97
Figure 5-7. Tibialis anterior [52]. 99
Figure 5-8. Soleus [52]. 99
Figure 5-9. Rectus femoris [52]. 100
Figure 5-10. Semitendinosus [52]. 101
Figure 5-11. Subject EMG placement. 101
Figure 5-12. Muscle activity during one gait cycle [51]. 102
Figure 5-13. Average healthy subject walking EMG data [51]. 102
Figure 5-14. Healthy subject normal treadmill walking TA EMG. 103
Figure 5-15. Healthy subject normal treadmill walking soleus EMG. 104
Figure 5-16. Healthy subject normal treadmill walking rectus femoris EMG. 104
Figure 5-17. Healthy subject normal treadmill walking semitendinosus EMG. 105
Figure 5-18. Healthy subject actuated treadmill walking TA EMG. 106
Figure 5-19. Healthy subject actuated treadmill soleus EMG. 107
Figure 5-20. Healthy subject actuated treadmill rectus femoris. 107
Figure 5-21. Healthy subject actuated treadmill walking semitendinosus EMG. 108
Figure 5-22. Mannequin test, a) at toe-off, b) swing phase, c) heel-strike. 109
Figure 5-23. Mannequin goniometer placement. 109
Figure 5-24. Mannequin hip angle. 110
Figure 5-25. Mannequin knee angle. 110

List of Tables

Table 3-1. Subject anthropometrics [37]. 34
Table 3-2. Motor torque and speed characteristics. 50
Table 4-1. Boundary Conditions for Single-Dwell Polynomial Functions. 66
Table 4-2. 80/20 3030 extrusion material characteristics [48]. 83

Acknowledgements

I would like to thank my advisor, Dr. Igo Krebs, for allowing me to pursue three different research projects which I enjoyed while learning a great amount from the experience.

Current and former members of the Newman Lab have been willing to answer my questions on many topics, attempted to pass on expertise, and made Journal Club a fun and rewarding experience. In no particular order I would like to thank: Steven Charles, Jooeun Ahn, Yun Seong Song, Shelly Levy-Tzedek, Benedetta Cesqui, Laura Dipietro, Emilio Gonzalez, Domenico Formica, Patrick Ho, Hyunglae Lee, Mohammad Rastgaar, and Nevan Hanumara.

I would not have been able to complete the machining for my projects without the help and advice from Mark Belanger in the Edgerton Student Shop. Whether I had to modify a life-size wooden mannequin, or machine more common parts, Mark had great patience and a sense of humor.

In order to ensure that the MRI wrist motor material selection would not cause image distortion, I needed to run a phantom test in an MRI. The staff at McLean hospital was extremely helpful and generous with their time and knowledge including Jennifer Britton and Mike Rohan.

Numerous friends and family members provided unwavering support throughout these past two years and their encouragement kept me on track. I would not have been able to achieve my dream of receiving a degree from MIT without the life-long love and support from my mother and father who taught me to always do my best. Finally, Jon Hastie, who has enriched my life every day for over five and a half years, helped me learn from my frustrations and celebrate my successes. :o)

Chapter 1: Introduction

1.1 Motivation

The goal of this project was to design a novel device that can be used to safely and effectively deliver efficacious gait therapy. While several robotic devices exist, none take advantage of the concept of passive walkers. This design will improve on these options by allowing gait therapy to begin before the patient can independently walk overground without restricting the movement to a rigid, repetitive kinematic profile, maximizing the amount of weight bearing steps with ecological heel strike that the patient makes, and having a compact design that can be implemented in a variety of settings.

1.2 Thesis Overview

This thesis contains six chapters and an Appendix A covering the development, design, fabrication, and testing of a novel proof-of-concept device for gait rehabilitation. Chapter 2 presents relevant background information about the populations this device may benefit, the fundamentals of human gait, and the available conventional and robotic therapy options. Chapter 3 defines the device functional requirements, discusses design concepts for both the walking surface and body weight support components of the device, and describes the design selected to build the proof-of-concept prototype. Chapter 4 details the design calculations for the material selection, component selection, and the assembly of the entire device. Chapter 5 addresses assembling both components of the device and testing its functionality with healthy subjects and a passive mannequin. Finally, Chapter 6 provides a summary for this project with items for future work required for this device to be able to be tested with affected patients in a clinical setting.

Work completed for two additional projects is presented in Appendix B and C. Appendix B contains a draft of a paper currently under review for publication that summarizes work with

MIT-Manus robot-derived metrics and four common clinical scales for 111 chronic stroke patients. The goal was to use the robot metrics to estimate the clinical scores. Appendix C documents work completed with an MRI compatible wrist device for rehabilitation. This device uses a single-vane motor and fluid to transmit power, but the seals around the vane were causing very high rotational friction while still allowing an unacceptable level of leakage around the vane. A new seal design was chosen, and a hollow cross-section as opposed to a solid seal was employed. The material selection of the vane motor was tested inside an MRI to check for image distortion and phantom signals.

Chapter 2: Background

This chapter will present relevant background information for this project including characteristics of stroke and spinal cord injury (SCI) subjects, human gait, common gait patterns adopted to compensate for injury, the conjecture of a central pattern generator, and finally conventional and currently available robotic therapy options.

2.1 Stroke and Spinal Cord Injury

Stroke is the third leading cause death and the leading cause of permanent disability in the United States, with about 5.8 million stroke survivors alive today and an estimated 700,000 strokes occurring each year [1]. A stroke occurs when a blood vessel that delivers oxygen and nutrients to the brain bursts (hemorrhagic) or becomes blocked (ischemic). Ischemic strokes are the most common [1]. Without oxygen and nutrients, the nerve cells in the affected area can die within minutes, and the functions the area controlled will be greatly affected or no longer work. Depending on the location affected, this can lead to decreased speech, behavior, memory, and motor skills. Weakness on one side of the body, called hemiparesis, is common. The effect of stroke on the ability to walk is significant with only 37% of stroke survivors regaining the ability to walk within one week post-stroke and a 73% incidence of falls within the first six months in individuals with mild to moderate impairment [2]. With the "baby-boomer" generation reaching their early 60's in 2008, the population at highest risk for stroke is expected to greatly increase as stroke incidence increases with age. This will add to the population in need of special care and therapy.

A second important population that requires physical therapy is patients with spinal cord injuries (SCI). Over 250,000 people in the United States have an SCI with an estimated 11,000 new injuries each year [3]. In contrast to the stroke population, the average age of SCI individuals is 31, with 56% of the injuries occurring between the ages of 16 and 30 [3]. The most common causes of injury are vehicular accidents (37%), followed by violence (28%), and falls (21%).

There are two main types of injuries, complete and incomplete. A complete injury results in the patient having no motor or sensory function below the injury while a patient with an incomplete injury may retain some sensory or movement function. Figure 2-1 shows the spinal cord and the corresponding areas of the body for each level. Approximately 52% of SCI patients are classified as paraplegic, with the injury occurring in the thoracic region, and 47% as quadriplegic, with the injury occurring in the cervical region [3]. Individuals with incomplete injuries may be able to regain function through physical therapy and this is an active area of research.

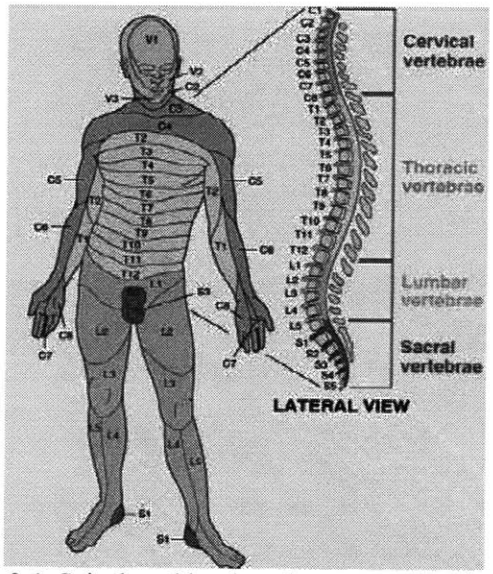

Figure 2-1. Spinal cord levels and corresponding function.

2.2 Gait Basics

Locomotion is the process through which an organism moves itself from one place to another. Although many methods exist, the majority of mammals are quadrupeds while humans are bipeds. Studies have shown that at slow speeds quadrupeds coordinate their limbs so that three feet remain on the ground and provide the stability of a tripod while one limb advances [4]. This behavior is also seen in crawling babies. Bipedal walking does not have this stability and requires greater neural control to maintain balance while advancing [4].

2.2.1 Gait Kinematics

Human walking is simply described as a process where an erect body is first supported by one leg and as the moving body passes over this leg the other is swinging forward in order to be the next support [4]. Figure 2-2 shows the distribution of swing and stance phases for a healthy human walking at an average speed of about 3 ft/sec (~1 m/s) and Figure 2-3 illustrates the anatomical planes of the body which will be used to describe the kinematics.

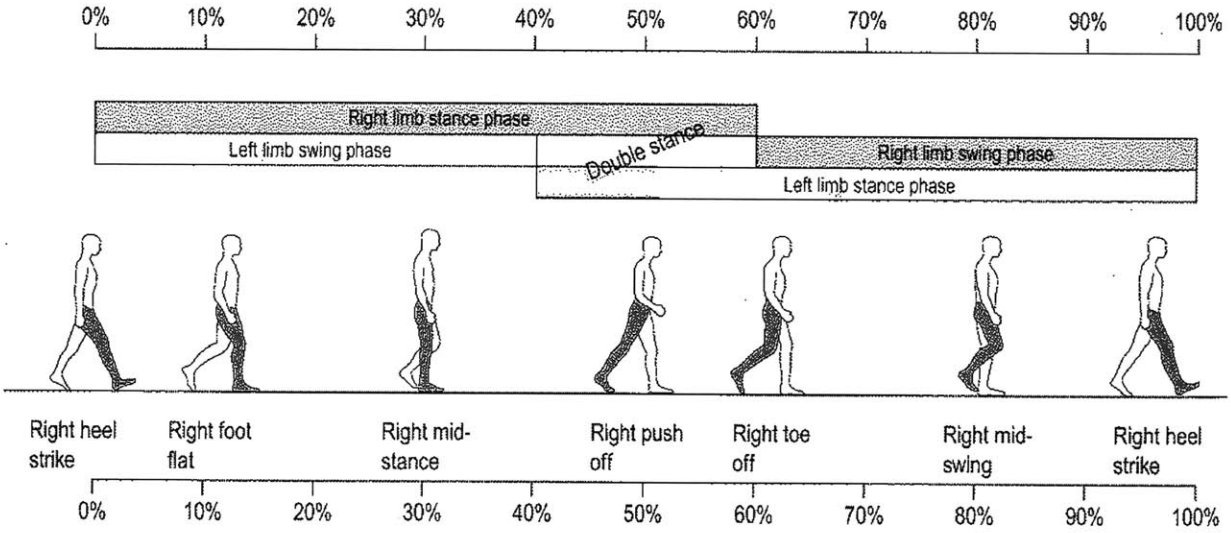

Figure 2-2. Normal human gait cycle at about 3 ft/sec (1 m/sec) [5].

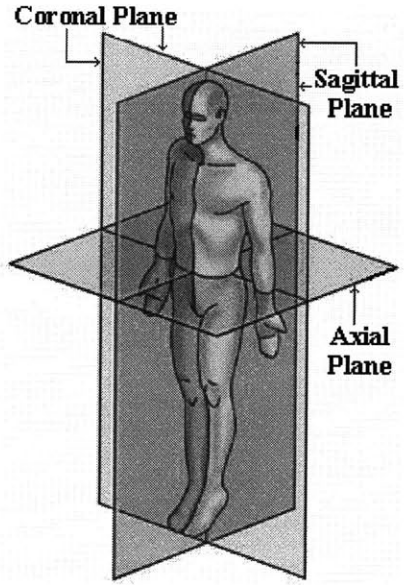

Figure 2-3. Anatomical planes of the human body (axial also known as the frontal plane).

Inman describes the six determinants of gait as: pelvic rotation, pelvic tilt, knee flexion in stance phase, ankle motion, foot contact, and lateral displacement of the body [4]. In normal, level walking, the pelvis rotates about the vertical axis about 4° on the non-weight-bearing side for a total of about 8° over a full cycle, and this rotation increases with gait speed (Figure 2-4). This rotation reduces the distance the center of mass must be lifted when the body passes over the stance leg and thus reduces the amount of energy required. The second determinant, pelvic tilt, is approximately 5° downward in the coronal plane at normal walking speed and reduces the clearance available for the swing leg. This requires the third determinant, knee flexion, in order for the foot to clear during swing phase. These first three determinants work together to reduce the vertical displacement of the center of mass resulting in a center of mass with the path shown in Figure 2-5. Normally, the vertical motion of the center of mass is about +/- 2 in (~5 cm) [4].

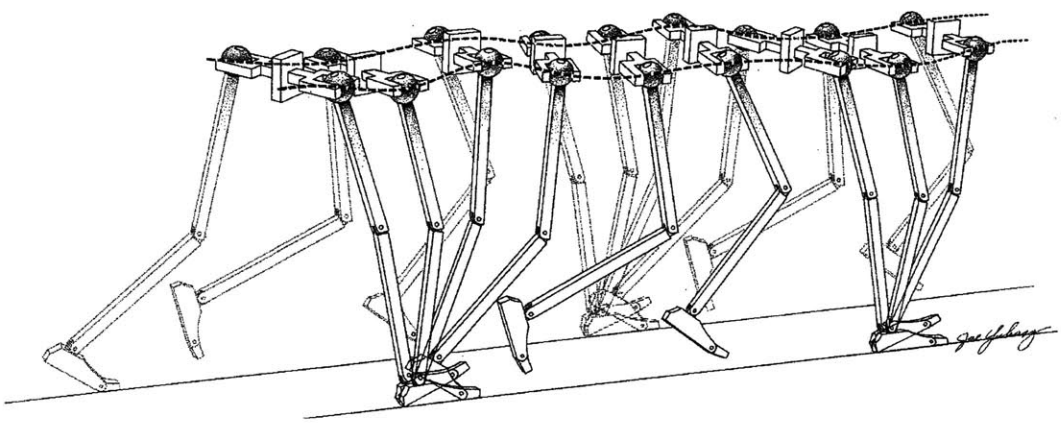

Figure 2-4. Trajectory of hip movement during gait.

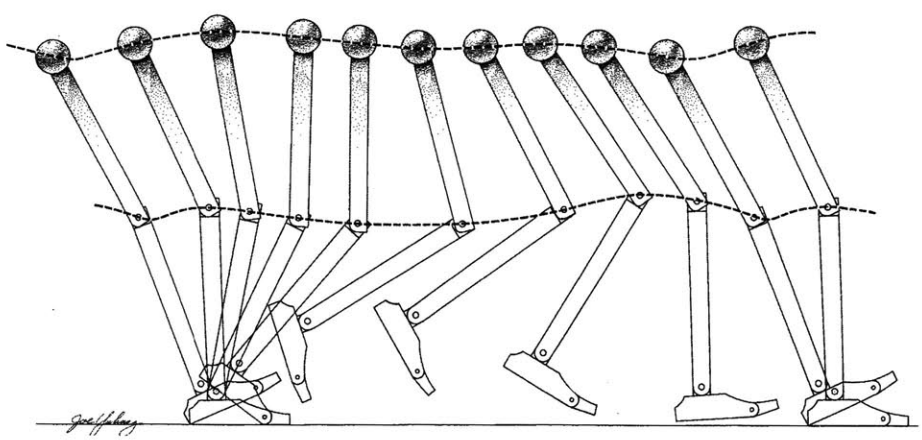

Figure 2-5. Trajectory of hip and knee during gait (side view).

The ankle and foot work together to prevent high stresses by cushioning the impact of the foot. During stance, the contact area of the foot reduces the deviation of the knee's path from horizontal. Ankle dorsiflexion and plantar flexion further smooth the path of the knee, reducing the impact load. The final element, lateral displacement of the body, occurs because the body shifts over the weight bearing leg with each step to increase stability. Over a full stride, this displacement is about 1.5 – 2 in (4 – 5 cm) and it increases as the width of the stance increases [4].

2.2.2 Pathological Gait

In order for an individual to be able to walk without aide, they must be able to do a minimum of four things [6]:

1) Each leg in turn must be able to support the full body weight without collapsing.
2) Balance must be maintained during single-leg stance.
3) The swing leg must be able to advance in order to transition into support stance.
4) Sufficient power must be provided to make the necessary limb and forward trunk movements.

When this is not possible, the individual may adopt abnormal movements, or use an aid such as a cane, crutches, or a gait orthosis. The following is a brief description of common pathological gait behaviors.

Lateral Trunk Bending

Lateral trunk bending, also known as ipsilateral lean or Trendelenburg gait, occurs when an individual bends their trunk towards the side of the supporting limb in an effort to reduce the forces on both the abductor muscles and hip joint of the swing leg during single-leg stance. This pattern is adopted for a variety of reasons which may include hip pain, hip abductor weakness, an

abnormal hip joint, or unequal leg length. This behavior produces the gait pattern commonly referred to as waddling [6].

Anterior and Posterior Trunk Bending

Anterior trunk bending occurs when the individual flexes their trunk forward early in stance phase and is a compensation for inadequate knee extensors (Figure 2-6) [6]. During normal gait, the ground reaction force vector at heel strike passes behind the knee joint and creates a moment that tries to produce knee flexion. This moment is opposed by contraction of the quadriceps. If the quadriceps are unable to resist this moment, leaning the trunk forward moves the ground reaction force vector in front of the knee which further extends the knee and prevents it from buckling due to the reduced quadriceps force [6].

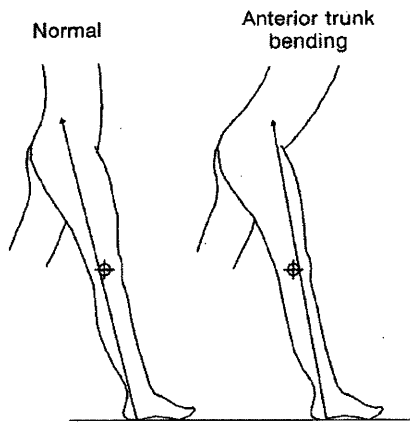

Figure 2-6. Anterior trunk bending.

Posterior trunk bending is the opposite of anterior bending where the individual leans their trunk backwards and is a compensation for inadequate hip flexors (Figure 2-7). The ground reaction force during normal gait passes in front of the hip joint which creates a moment that tries to flex the trunk forward on the thigh. This moment is opposed by contraction of the hip extensors, most importantly the gluteus maximus. By leaning the trunk back, the ground reaction force vector is shifted to behind the hip joint, thus reducing the force required by the hip extensors [6].

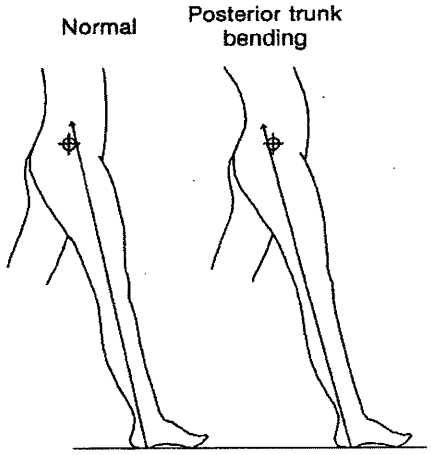

Figure 2-7. Posterior trunk bending.

Circumduction

When an individual is unable to create enough clearance for the swing leg to advance using a normal gait pattern, this clearance is sometimes achieved by swinging the leg out to the side (Figure 2-8). Often, this gait pattern is used when only one leg is affected, as in hemiparesis, and the healthy leg completes a normal swing phase. In this case, circumduction is used to compensate for weak hip flexors [6].

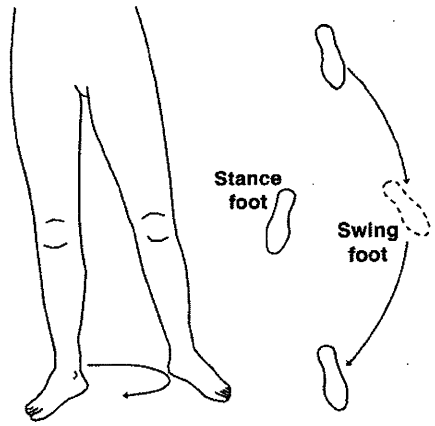

Figure 2-8. Circumduction.

Hip Hiking

Another strategy to create leg swing clearance is hip hiking. The individual lifts or "hikes" the side of the pelvis of the swinging leg by contracting the spinal muscles and the lateral abdominal wall (Figure 2-9) [6]. This behavior affects both the pelvic rotation and pelvic tilt determinants of gait presented previously. Hip hiking is often employed to overcome weak hamstrings which allow the knee to extend making the leg too long to clear during the swing phase [6].

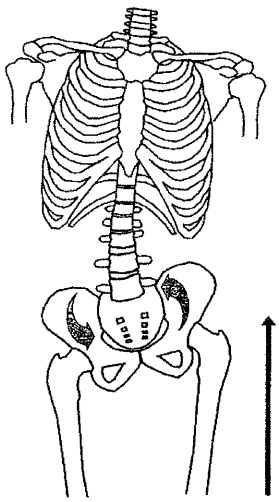

Figure 2-9. Hip hiking.

Steppage

Steppage is another strategy used to increase the clearance during the swing phase through increasing the knee and hip flexion to lift the foot higher than normal (Figure 2-10). This is most common when the individual is compensating for a plantarflexed ankle, commonly known as "drop foot" [6].

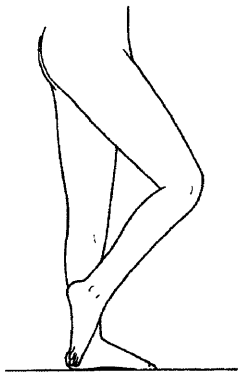

Figure 2-10. Steppage.

Vaulting

In an additional effort to produce sufficient ground clearance during the swing phase, rising up on the toes of the stance phase leg is called vaulting (Figure 2-11). Vaulting is similar to circumduction, hip hiking, and steppage in how it attempts to increase the clearance of the swing leg, but unlike those behaviors it involves the stance leg as opposed to the swing leg. It is employed to counteract weak hamstrings or to provide clearance of the prosthesis of an above-knee amputee [6].

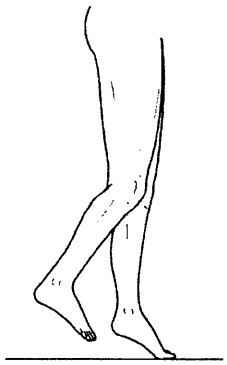

Figure 2-11. Vaulting.

Although the preceding was not meant to be a comprehensive list of all gait pathologies, a common trait of many of the compensation behaviors was to overcome a decrease in the amount of ground clearance during swing phase. This clearance is a cause of several pathologies which prevents normal gait and should be addressed when delivering therapy [6].

2.3 Central Pattern Generator

The human body can exhibit different types of movements. The simplest type of movement is reflexes, such as knee jerk, which are involuntary and occur when the stimulus is large enough to activate the required sensory pathway [7]. In contrast, rhythmic motor patterns like walking are much more complex and are subject to continuous voluntary control [7]. Hooper defines a central pattern generators (CPGs) as, "...neural networks that can endogenously (i.e. without rhythmic sensory or central input) produce rhythmic patterned outputs; these networks underlie the production of most rhythmic motor patterns" [7]. Additional research, commonly with spinal cats, has shown that the generation of rhythmic patterns does not require the action of the entire nervous system, but rather only the CPG's small, autonomous neural network [7]. Studies have shown that spinal cats that underwent intense treadmill training were able to regain gait function even though the spinal injury did not completely heal. There is still a large debate on whether CPGs play and similar role in humans.

Dietz found in a study of six patients with complete spinal cord injury that when EMG data was recorded of treadmill gait training with 70% body weight support and therapists lifting and placing the legs that the electromyography (EMG) patterns were comparable to healthy subjects, but with smaller amplitudes [8]. While individuals with complete spinal cord injuries have not regained gait function, the training has positive effects on the cardiovascular and musculoskeletal systems [9]. Both complete and incomplete SCI patients have also shown significant increases in EMG activity during gait training which indicates that the isolated human spinal cord contains both the capacity to generate a locomotor pattern and to "learn" [9]. Harkema et al. observed that for spinal patients the EMG signal amplitude was highly correlated with the phase of the gait cycle and was independent of loading [10].

EMG responses in affected patients are hypothesized to be due to the Golgi tendon organs (Figure 2-12). These receptors are located at the intersections of muscle fibers and tendons and interpret loading. Providing stimulation to these receptors is theorized to be critical to improving the outcome of gait rehabilitation for SCI patients and highlights the importance of load-bearing stepping during therapy [8-9].

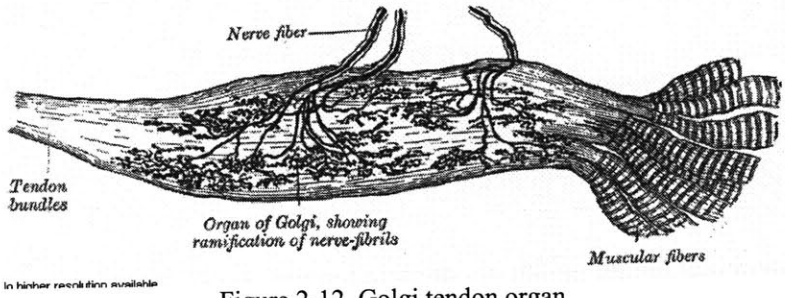

Figure 2-12. Golgi tendon organ.

EMG activity has also been studied in hemiparetic stroke patients, and Kirker et al. reported amplitude and onset latency in hip abductors and adductors of seventeen patients in response to sideways pushing [11]. This study also found that the hemiparetic subjects exhibited normal muscle activation patterns during stepping compared to age-matched controls, despite poor standing balance control. Kirker concluded that hemiparetic patients should be able to start gait training before they regain full balance [11]. Beginning gait training sooner may improve the outcome and build muscles to also improve balance.

2.4 Gait Therapy

The ability to walk is very important for an individual to be independent. Falls are a leading cause of injury among Americans over 65 years old with over one third of this population experiencing a fall each year [12]. An unsteady gait increases this risk which may result in further injury. Gait therapy aims at re-training the nervous system, re-building muscles, improving balance, and teaching proper kinematics to reduce the stresses applied to bones and muscles.

There are two main methods of providing gait therapy – traditional physiotherapy and robotic therapy. Both types are discussed below.

2.4.1 Physiotherapy

There are different schools of thought and methods for delivering physiotherapy. One of these was developed by Bobath and it suggests that before a patient is instructed to take a step they must prepare by training trunk balance by both sitting and standing, modify motor responses of the lower limb including contraction of the hip and ankle muscles, and alternate responses of antagonist muscles including knee flexors and extensors [13]. These tasks are meant to reduce the amount of compensatory behavior required to execute a gait cycle since poor habits are often hard to break once they have been adopted. The Bobath method states that, "all the various phases of walking can be prepared for in standing" [14]. Before full gait training is started, subjects practice transitioning from a seated to a standing position with full weight balanced over both feet without using any aids or their arms to complete the task [15]. Bobath developed this method to treat cerebral palsy patients but the benefits observed for that population have not been reported with stroke patients.

Once standing has been accomplished, therapists may provide the necessary support to facilitate stepping. This support includes the therapist standing on the patient's affected side and placing their hands on either side of the patient's pelvis and the thumbs or balls of the hand to facilitate hip extension and avoid hyperextension of the knee. For each step, the therapist guides the weight over the stance in preparation for the following swing phase. The emphasis is placed on completing proper movements rather than speed and distance [15].

While there are other training schools, some advocating the opposite approach compared to the Bobath method, delivering therapy is very labor intensive for the therapist(s) involved where patients can easily outweigh the clinician. This creates a serious limitation on how long the therapy can be delivered without causing injury to the therapist or their fatigue becoming a safety risk for the patient.

2.4.2 Robotic Therapy

Mechanical devices can be employed to alleviate therapist exertion, but there are potential disadvantages: a machine can decrease the amount of time the therapist is in contact with the patient. Another potential handicap is that a machine may provide too much aid allowing the patients to be "lazy" and not attempt to move or activate load receptors. The common mechanical device employed to assist in gait therapy is the treadmill. It reduces the space needed and assists the therapist in completing part of the movement.

Overground vs. Treadmill Walking

Utilizing mechanical devices to deliver therapy is not a new idea and several have been developed for gait therapy. One method of reducing the amount of space required for therapy and to encourage patients to maintain a constant gait velocity is to conduct the therapy on a treadmill. Numerous studies have been completed with both healthy and impaired subjects to compare gait kinematics between treadmill and overground walking and the effect of body weight supported treadmill training (BWSTT) on functional outcome. Riley et al. studied 33 healthy subjects and compared their overall gait kinematics for overground and treadmill walking and concluded that the kinematics were very similar but that the ground reaction forces were significantly larger ($P<0.05$) for the overground walking compared to the treadmill [16]. Similarly, Lee et al., Stolze et al., and Matsas et al. observed small differences in joint kinematics for healthy subjects, but concluded that treadmill walking did not show any negative effects on gait [17-19]. In studies that included hemiparetic patients, Nilsson found no difference in walking ability, balance, or sensorimotor performance between the BWSTT group and the subjects that completed overground training [20]. Hesse et al. found a significant difference ($P<0.05$) between BWSTT and conventional Bobath physiotherapy concluding that treadmill training was superior with regard to restoring gait function [21].

To evaluate if providing BWS effected the outcome of gait training, Visintin et al. studied a population of 100 stroke patients that were randomly selected to complete treadmill gait therapy either with 40% BWS or without BWS for six weeks [22]. The results showed that the BWS

group scored significantly ($P<0.05$) higher than the no-BWS group for functional balance, motor recovery, overground walking speed, and overground walking endurance. This significant difference continued at the 3 month follow-up evaluation with the BWS having significantly higher scores for overground walking speed and motor recovery.

An additional advantage of using a treadmill for gait training is the ability to control and increase the speed at which therapy is being completed. Pohl et al. studied a group of 60 stroke patients randomly chosen to receive either structured speed-dependent treadmill training (STT) (with the use of an interval paradigm to increase the treadmill speed), limited progressive treadmill training (LTT) (speed increased no more than 5% per session), and conventional gait training (CGT) (Bobath techniques) [23]. After a 4-week training period, the STT group scored significantly higher ($P<0.01$) than the LTT and CGT groups for overground walking speed, cadence, stride length, and Functional Ambulation Category scores [23]. Lamontagne et al. also found a positive result from increasing gait speed without any observed negative effects and the increased speed induced improvements in body and limb kinematics and muscle activation patterns [24].

Treadmill training has not been found to have a detrimental impact and in some studies subjects that completed therapy with a treadmill regained more function compared to traditional physiotherapy. With the added benefit of BWSTT reducing the strain on the therapists, this method is safe and acceptable.

The following are examples of devices designed for delivering gait therapy. It is not meant to be a complete listing, but rather an illustration of devices commercially available and in development.

LiteGait®

LiteGait® is a body weight support device that can either be coupled with a treadmill or used for overground training (Figure 2-13). While it increases the safety of gait training by providing support in case of a fall, the therapist must still bend over in order to access the patient's legs to

aid with providing swing clearance and proper foot placement. This device does have the advantage of being simple and easy to maneuver and able to be used in both treadmill and overground therapies.

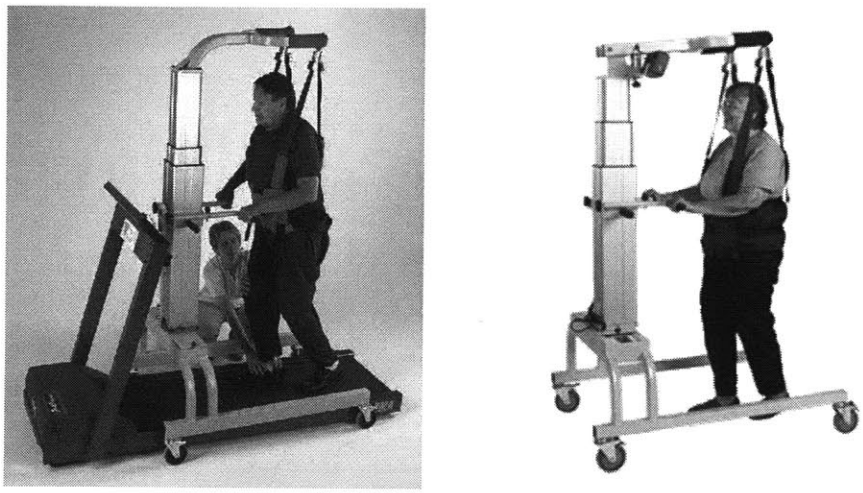

a) b)

Figure 2-13. LiteGait, a) coupled with a treadmill, b) for overground training.

Robotic Devices –

While treadmill training improves efficiency, it still requires a therapist to monitor pelvis movement and propel the leg forwards. Robotic devices were built in an attempt to automate the therapy process. The following are a sample of these robots.

Gait Trainer I

The Gait Trainer I incorporates an adjustable BWS and driven foot plates that simulate stance and swing which are secured to the patient's feet (Figure 2-14). While it eliminates the need for therapist intervention after the patient is secured in the device, the motorized foot plates do not require any action by the patient. This motion may not adequately stimulate muscle load receptors and by actively moving the patient's feet, the patient is allowed to be "lazy". A multi-center study, DEutsche GAngtrainerStudie (DEGAS), with 155 non-ambulatory, sub-acute stroke patients compared outcomes from traditional physiotherapy alone and combined

physiotherapy and use of the Gait Trainer I over a four week period [25]. After the study, approximately 53% of the group that received the combined therapy was able to walk independently compared to approximately 22% of the physiotherapy group. This improvement remained at the six-month follow-up with 70% of the combined therapy group and 36% of the physiotherapy group able to walk independently [25].

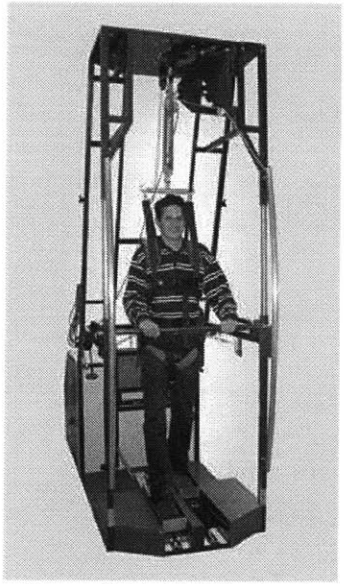

Figure 2-14. Gait Trainer I.

Peurala et al. completed a study with 45 ambulatory chronic stroke patients separated into three therapy groups: 1) Gait Trainer I, 2) Gait Trainer I with functional electric stimulation, and 3) walking overground (without robotic aides) [26]. All groups also received traditional physiotherapy and the study lasted three weeks. Evaluations conducted at the conclusion of the study and at six-month follow-up showed that all groups improved walking and dynamic balance, and the best result was obtained in the Gait Trainer I with electric stimulation group [26].

Haptic Walker

Developed by Henning Schmidt and the Rehabilitation Robotics Group at the Fraunhofer Institute, the Haptic Walker (Figure 2-15) is a walking simulator for patients with affected central nervous systems (i.e. stroke) [27]. This device includes body weight support and two

platforms, one for each of the patient's feet to be attached. The platforms have programmed motion patterns including simulating normal walking and stair climbing and move the patient's legs. This device is not yet commercially available and further testing will be required to see if patient's benefit from this type of therapy and if the programmed gait patterns provide adequate activation of the muscle load receptors.

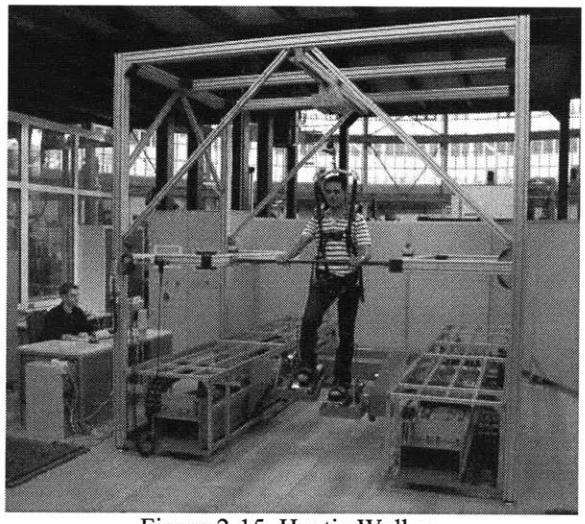

Figure 2-15. Haptic Walker.

KineAssist™

KineAssist is designed for overground use with the goals of maximizing patient safety while allowing therapists easy access to the patient's legs (Figure 2-16). This device is compact and designed to be able to fit through standard doors. The patient attachment supports the back and the pelvis but still allows rotation about the vertical axis, lateral bending, and pelvic hike [2]. Designers included these degrees of freedom so that the patient could be challenged and would not be able to depend on a rigid structure. KineAssist is able to support a patient in the event of a fall which allows therapists to safely challenge patients.

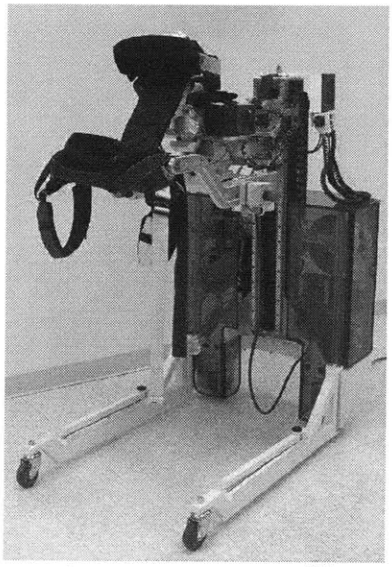

Figure 2-16. KineAssist™.

Lokomat®

The Lokomat BWSTT system is widely adopted and is currently used in over 130 rehabilitation centers worldwide (Figure 2-17) [28]. It includes a treadmill, an adjustable and active BWS designed to provide a constant level of support throughout the gait cycle, and a robotic orthosis with four degrees of freedom (left and right knee and hip joints) [29]. The device allows vertical movements during gait, but prevents lateral movements which are a major limitation as it prevents weight shifting from one leg to the other. It also monitors hip and knee angles and imposes a fixed gait pattern determined from testing with healthy subjects. Under this condition, the subject can remain completely passive and the actuators of the gait orthosis provide the necessary power. Additional schemes are being developed in an attempt to allow a more interactive experience.

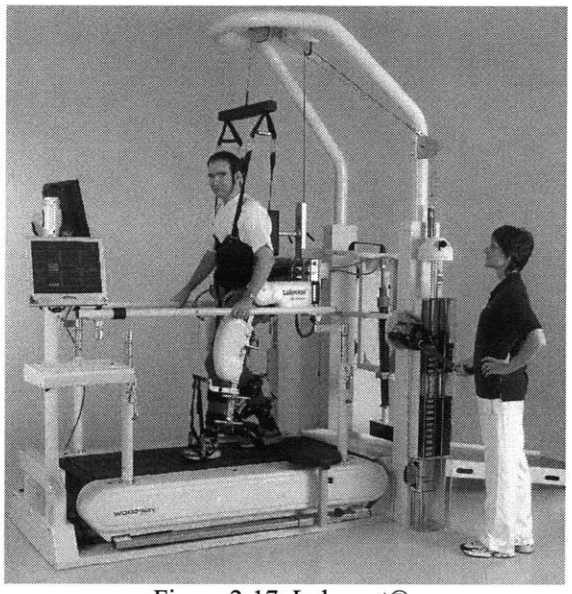

Figure 2-17. Lokomat®.

Several studies have been completed with the Lokomat to investigate the effects of gait training with a predetermined gait pattern. Mayr et al. conducted a randomized blinded pilot study with 16 subjects in an ABA or BAB design (A = 3 weeks of Lokomat training and B = 3 weeks of conventional physical therapy) [30]. Both therapy groups improved their walking function significantly over the trial, but the most improvement for both groups was observed after the completion of a Lokomat training block [30]. These findings were not replicated in larger studies by Hornby et al. [31] and Hidler et al. [32] who completed studies comparing Lokomat training to conventional therapy for stroke patients and found no advantage of the Lokomat training.

Due to the fact that the robotic orthosis limits degrees of freedom, muscle activation patterns may differ compared to normal treadmill walking and Hidler et al. [28] observed significant differences in the spatial and temporal muscle activation patterns of healthy subjects. Specifically, quadriceps and hamstring activity was significantly higher during the swing phase for Lokomat training and ankle flexor and extensor muscle activity was reduced throughout most of the gait cycle. A recent study completed by Hidler et al. to investigate kinematic trajectories of healthy subjects walking in the Lokomat compared to normal treadmill walking showed that the range of motion of the ankle and amount of ankle extension is significantly greater in the Lokomat and peak ankle flexion occurred 11.7% earlier in the gait cycle [28]. Similar results

were found with the hip muscles indicating that subjects begin the swing phase earlier compared to treadmill walking. Another finding was that the robotic orthosis shifted during gait, which is significant because the Lokomat applied gait pattern relies heavily on the angular measurements which are assumed to be recorded from the subject's joint center. Misalignments of up 0.78 in (2 cm) were observed at the knee during swing and up to 1.5 in (4 cm) were measured at the hip during stance [28].

While the Lokomat greatly reduces the strain on therapists and provides a safe environment for patients to practice walking, especially during the early stages of rehabilitation, it also allows patients to be "lazy". Furthermore, as patients regain walking ability, the limited degrees of freedom do not require balance or weight shifting which are necessary for adaptation to daily living [30].

The next chapter will present the design concept development for a novel device for gait rehabilitation that will safely incorporate the needs of maximizing foot-ground collisions during therapy and provide adequate body weight support while keeping the subject actively engaged in the therapy.

Chapter 3: Design Concepts and Selection

This chapter will discuss the design process beginning with the brainstorming phase and through the design concept formulation and selection. It will also outline the functional requirements for this device.

The goal of this system is to allow patients to begin treadmill gait therapy before they are able to walk independently overground, but contrary to existing devices, it will not specify a rigid kinematic pattern that must be followed. In addition, this device will address the need of allowing proper neural input provided by heel strike. If patients can be trained earlier in the recovery process, it may reduce the amount of compensatory behavior (i.e. "bad habits") they develop including hip hike and circumduction as discussed in Chapter 2. This project was inspired by the passive walking devices which are purely mechanical with no actuators, sensors, or controllers that are able to "walk" down slopes (Figure 3-1) [34]. The device in Figure 3-1 is able to walk down a 3.1° slope at a speed of about 1.67 ft/sec (0.51 m/s). In order for this concept to be applied to human gait, a method to create the required ground clearance for swing must be developed.

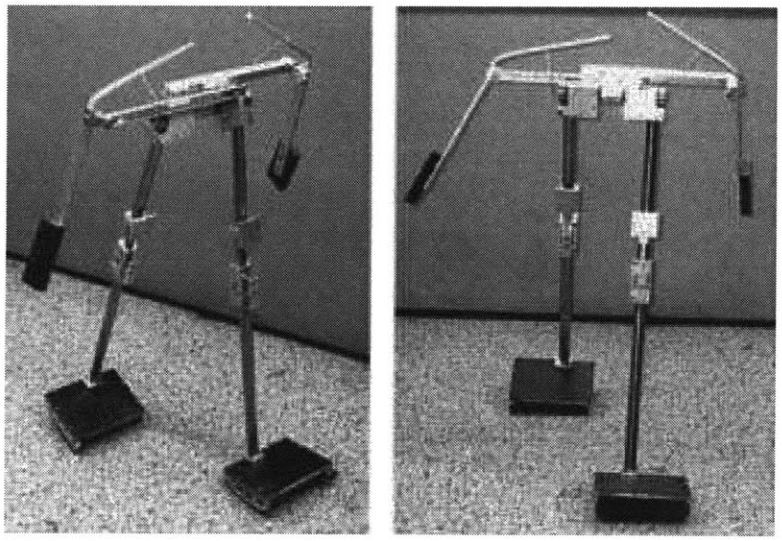

Figure 3-1. Two-legged passive walker [34].

3.1 TRIZ – Theory of Inventive Problem Solving

TRIZ is an acronym in Russian which translates to, "The Theory of Inventor's Problem Solving," and was developed by Genrich Altshuller beginning in 1946 [35]. Altshuller received his first certificate of authorship (Russian equivalent of a patent) at age 15 for an underwater breathing apparatus, and his next at 20 for a method for escaping a submarine without diving gear. In the late 1940s, he began work in the Inventions Inspection department of the Russian Navy, and by 1969 had reviewed about 40,000 patent abstracts in order to determine if an invention had been developed [35].

From this experience, he developed 40 principles which he noticed were common traits employed in successful inventions [35]. An example of these principles is "Phase Change" and this principle utilizes the properties of material phase transitions in the design solution. One example is the construction of space shuttles which use layers of material that will evaporate as they reenter the atmosphere to absorb the intense heat and keep the shuttle cooler [36].

Altshuller recognized that one of the keys to the success of inventive ideas was that many problems stem from contradictions between two or more components or desired traits. One simple example is the desire to produce a car that is both fast and affordable. In order to make the car travel faster, a larger engine is often needed, but this increases the price of the car. He defined inventing as identifying and eliminating the contradiction.

During the beginning stages of brainstorming for this project, the contradiction encountered was that while a walking surface is necessary for gait therapy, this surface inhibits the leg during the swing phase and requires intervention to overcome. In conventional physiotherapy, this intervention is the therapist lifting the patient's leg, and for the Lokomat the robotic orthosis provides the foot clearance. It is also the reason that patients develop compensatory behavior when they are unable to produce adequate swing clearance. These solutions are employed above the walking surface and do not attempt to alter it.

Two TRIZ principles applicable to this problem are "Do it in Reverse" and "Periodic Action" [36]. "Do it in Reverse" applies an opposite action. A stationary lap pool uses this principle by moving the water while the swimmer remains in place. This allows the pool to be compact without restricting the swimmer [36]. For this project, altering the walking surface is the opposite of previous devices and instead of lifting the patient's leg, lowering the walking surface would also provide swing clearance. The second principle, "Periodic Action" replaces a continuous action or process with a periodic one [36]. This principle is already employed in therapy where the patient's leg is lifted only when floor clearance is needed. For this project, the walking surface could remain stationary during foot contact and only lower during the swing phase.

A treadmill was chosen to employ these principles because it has positive characteristics of delivering therapy in a confined space, providing a constant, controllable gait speed, is a proven device for gait therapy, and the surface height can be made adjustable. A scaled proof-of-concept of this idea was developed and is presented next.

3.2 K'nex Proof-of-Concept

In order to quickly and inexpensively determine if actuating the walking surface was a feasible solution, a model was made using the construction toy K'nex and a 12 inch (30.5 cm) wooden mannequin (Figure 3-2). The mannequin was altered so that its legs would swing freely and it was crudely supported above the treadmill (note: this method of body weight support is not suggested as a viable solution!). The treadmills were constructed from rubber bands and were hinged and driven by the same motor so the height of one was independent of the other.

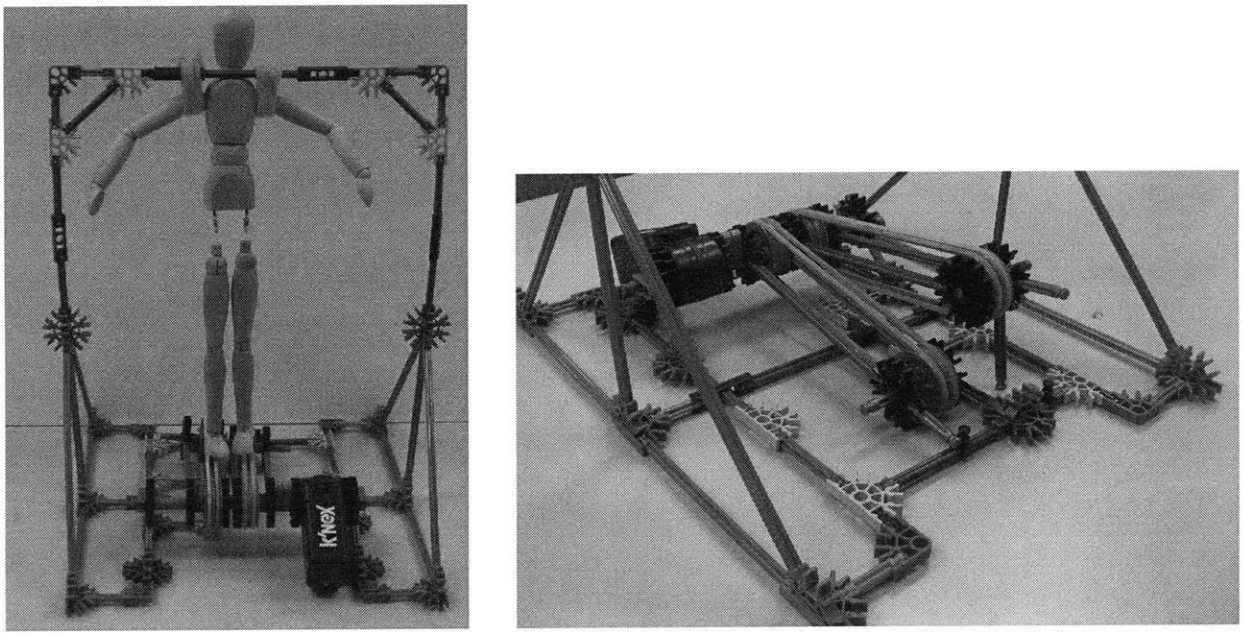

a) b)

Figure 3-2. K'nex scaled proof-of-concept, a) system with 12" mannequin, b) close-up of treadmill concept.

The motor drove both "treadmills" at the same speed and they were "actuated" by hand. Even though the mannequin's legs had additional degrees of freedom compared to the average human (namely rotation about the vertical axis), by keeping the treadmill surface parallel to the ground during foot contact and then lowering to allow free swing, the mannequin was able to maintain a gain pattern. This concept appears to be a feasible solution and will be developed and scaled for human subjects.

The functional requirements for a rehabilitation device that employs this idea will be discussed next.

3.3 Functional Requirements

In order for this device to be able to effectively and safely deliver gait therapy it must be adjustable to accommodate a range of patients. Figure 3-3 shows the measurements of the 99th percentile male and the 1st percentile female and Table 3-1 lists the measurements that will be considered when determining the amount of necessary leg swing clearance and the dimensions of

the BWS. The requirements for both the treadmill unit and BWS unit are outlined in the following sections.

	99% Man	1% Woman
Height (in) [cm]	75.6 [192]	58.1 [147.5]
Weight (lbs) [kg]	244 [111]	93 [42]
Chest width (in) [cm]	14.1 [35.6]	8.8 [22.4]
Average Stride (in) [cm]	27.4 [69.6]	20.2 [51.3]
Hip Width (in) [cm]	16.9 [42.9]	11.2 [28.4]
Ground to hip (in) [cm]	40.1 [101.8]	29.6 [75.2]
Ground to armpit (in) [cm]	60.6 [153.9]	45.4 [115.3]
Ground to crotch (in) [cm]	36 [91.4]	27 [68.6]

Table 3-1. Subject anthropometrics [37].

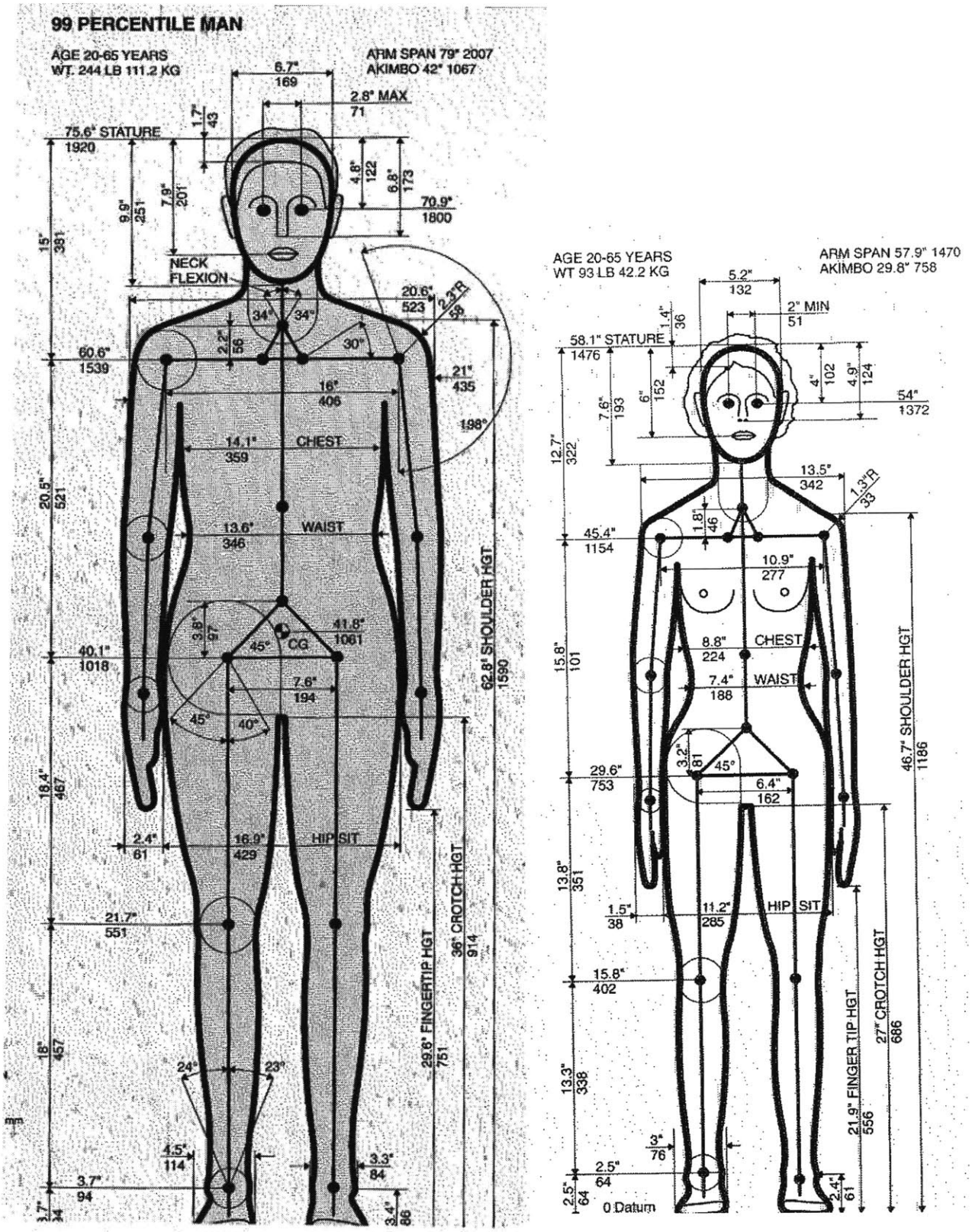

a) b)

Figure 3-3. Anthropometrics a) 99% Male, b) 1% Female [37].

3.3.1 Treadmill

In order for the treadmill to meet the requirements to deliver therapy, it must provide a stable walking surface that is parallel to the ground, allow adequate clearance for a leg to swing without knee flexion, and return to the parallel position in time for the heel strike of the next stride. The average walking speed of a healthy individual is 3.3 ft/sec (1 m/s), but studies with stroke patients are often completed at speeds between 0.29 and 1.17 ft/sec (0.09 – 0.36 m/s) [38]. An appropriate treadmill must be able to operate in this range for use by affected subjects. Figure 3-4 shows the required foot clearance for the 99th percentile male and 1st percentile female for both a 10° and 15° toe-off angles.

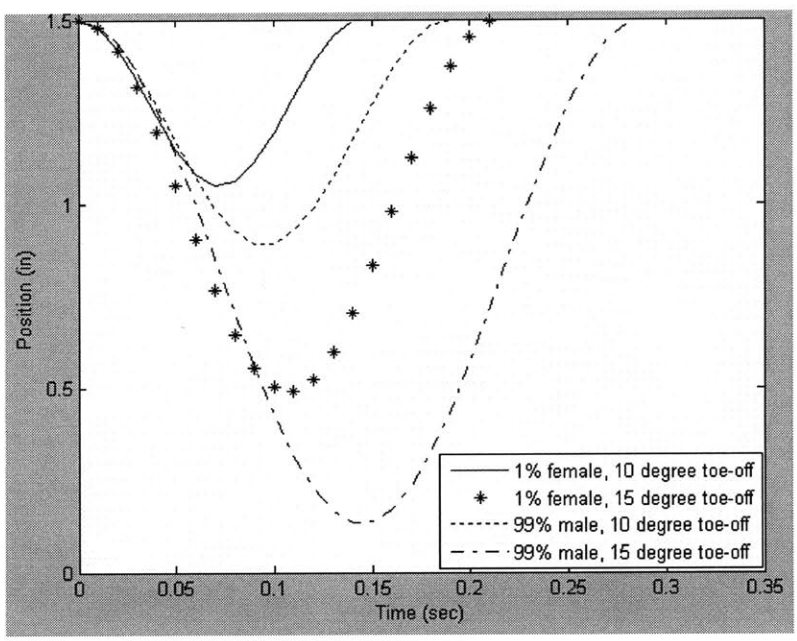

Figure 3-4. Foot clearance and time requirements for treadmill actuation.

While 10° is the common angle for healthy individuals walking at about 3.3 ft/sec (1 m/s), 15° was included as a factor of safety. These trajectories were calculated by treating the leg and heel as a simple pendulum acting under gravity with Equations 3.1 – 3.3:

$$T = 2\pi\sqrt{\frac{L}{g}} \quad \text{(eq. 3.1)}$$

$$\theta(t) = \theta_o \cos\left(\sqrt{\frac{g}{L}}t\right) \quad \text{(eq. 3.2)}$$

$$MaxClearance = L\left(1 - \cos\theta_o\right) \quad \text{(eq. 3.3)}$$

Where T is the full period of the leg (a swing phase would be ¼ of the full period of a pendulum), $\theta(t)$ is the angle of the leg at time t, θ_o is the toe-off angle, L is the length of the leg, and g is the gravity constant (32.2 ft/sec^2 or 9.81 m/s^2). For the 99th percentile male with a 15° toe-off, 1.5 inches (3.8 cm) of swing clearance will be adequate. Also, for the 1st percentile female, the treadmill must be actuated in 0.14 seconds in order to provide swing clearance and return to parallel in time for foot strike.

Figure 3-5 shows the angles of the hip, knee, and ankle throughout a healthy gait cycle [5].

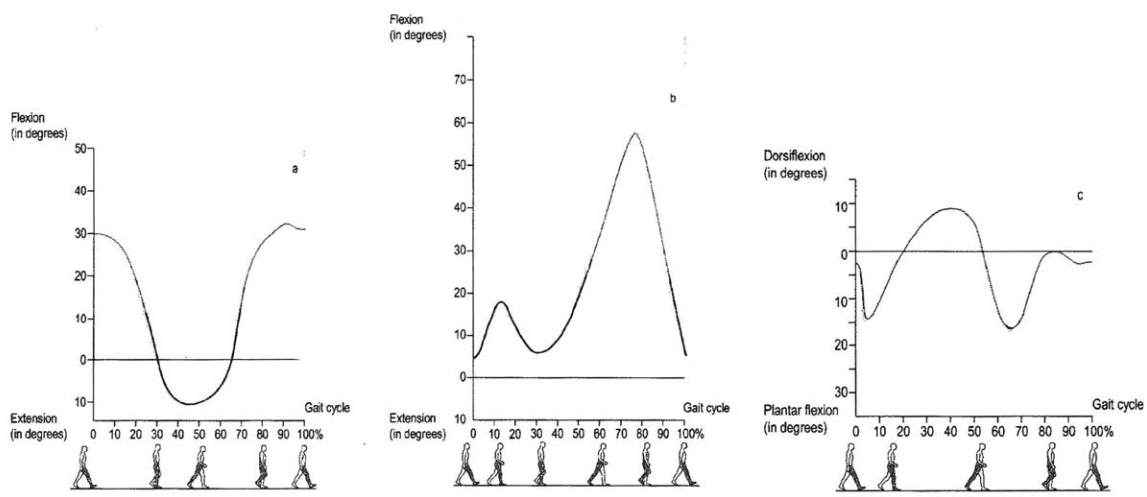

a) b) c)

Figure 3-5. Angles during a healthy gait cycle at about 3.3 ft/sec of, a) the hip, b) knee, and c) ankle.

The walking surface of the treadmill must be long enough for the subject to be able to complete a normal stride, with an allowance for missteps, and the width must accommodate stance width. The recommended minimum treadmill length is about 60 in (150 cm) with a width of 25 in (60

cm) [38]. It should be noted that the width of the treadmill should not exceed 29.5 in (75 cm) because this will require the therapist to lean forward in order to access the subject's legs [15].

BowFlex® TreadClimber®

A hinged, split treadmill is available on the market as an exercise machine called the BowFlex TreadClimber (Figure 3-6). This treadmill is similar to the K'nex proof-of-concept with two treadmills hinged at one end and driven by the same motor. Since this device is marketed for home use, it is designed for disassembly so that it can be shipped in flat, compact boxes. Another advantage of being designed for home use is that it has a small footprint compared to many treadmills with a width of 28.5 inches (72.4 cm) and a length of 46 inches (116.8 cm).

a) b)

Figure 3-6. a) BowFlex® TreadClimber®, b) TreadClimber® in Use.

In contrast to its use for exercise where the adjustable cylinders provide resistance as the user steps and pushes the treadmill down so it is parallel to the ground, a patient would be facing in the opposite direction and the treadmills would be externally actuated up and down. The cylinders, display support columns, and handles would be removed to accommodate this change and the display and controls would be relocated for easy access by a therapist.

The TreadClimber treadmill length is 40 inches (101.6 cm), which will be adequate for the testing of healthy patients and since the body weight support system will prevent the subject from shifting forward or backward along the treadmill. The total treadmill width is 18.5 inches (47 cm) which will allow the therapist easy access to the subject's legs.

A BowFlex TreadClimber TC3000 was chosen to serve as the base for the full scale proof-of-concept prototype. Additional product specifications are listed in Appendix A.

3.3.2 Body Weight Support

Many patients are not able to stand under their own weight when they begin physical therapy or they may need assistance maintaining balance. A body weight support (BWS) system needs to provide enough support to unload up to 100% of the patient's weight and keep the patient safe from falls while not interfering with the required ranges of motion. Using an upper limit of a 350 lbs (158.8 kg) patient, and a factor of safety of 3 for fall prevention, the BWS must be able to withstand up to about 1050 lbs (476.4 kg).

Providing too many degrees of freedom may make it difficult for a patient to maintain stability, but restricting all pelvic motion will not create a realistic walking environment. A BWS should allow enough vertical movement of the patient's center of gravity to permit normal gait without causing a loss of posture. As discussed in Chapter 2, a common rule of thumb is to allow +/- 2 in (5 cm). A study of 25 healthy men and 25 healthy women measured the average vertical displacement as 1.46 +/- 0.35 in (3.7 +/- 0.9 cm) and 1.06 +/- 0.24 in (2.7+/- 0.6 cm) respectively [38]. Pelvic tilt is also important to maintaining balance and about 5° is required on average. In addition, rotation about the vertical axis of +/- 4° is important for the swing phase and advancing the foot for the next step.

This structure must fit around the treadmill assembly which is 24 inches (61 cm) wide, but still be narrow enough to fit through a standard door frame which is 35 inches (89 cm) wide and 83 inches (211 cm) tall so it can be moved easily. The design chosen to actuate the treadmills will

determine the height above the ground the walking surface will be which will dictate the required height of the body weight support.

3.4 Actuation Design

The key to the success of this device is to actuate the treadmills so that they are parallel to the ground during foot stance, provide an adequate swing clearance of 1.5 inches (3.8 cm), and return to the parallel position for heel strike. Load calculations were completed using the 18 lb (8.2 kg) weight of the treadmill alone, and assuming the subject weighed 350 lbs (158.8 kg). The following are eight design configurations that are able to produce this required motion. Each concept's strengths and weaknesses are discussed.

3.4.1 Lead and Ball Screws

Lead screws are able to convert the rotary motion of a motor into precise linear motion and are capable of withstanding large axial loads. The two components of a lead screw are the screw and the nut (Figure 3-7). The screw diameter, pitch, and material are chosen by the loading conditions and speed requirements. The nut material is chosen to complement the screw and is often softer so that the threads are not quickly worn.

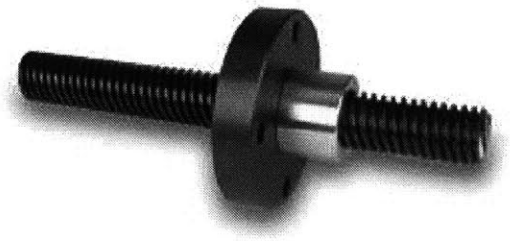

Figure 3-7. Lead screw example.

Ball screws are similar to lead screws, but they also contain ball bearings in the nut (Figure 3-8). These bearings reduce the friction between the screw and the nut, but also increase the cost.

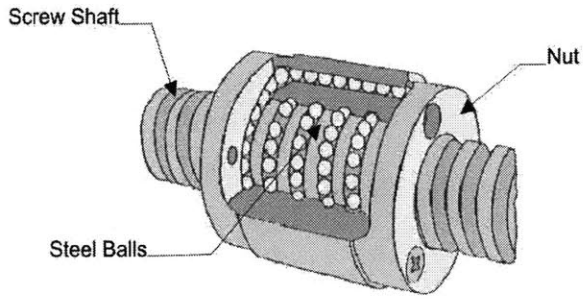

Figure 3-8. Ball screw.

Figure 3-9 shows a schematic with a lead screw and a motor actuating each of the treadmills.

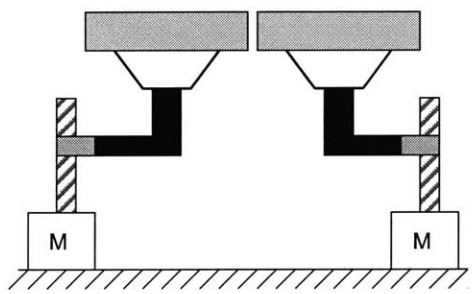

Figure 3-9. Lead screw design configuration.

In order for the required clearance between the treadmill and the lead screw, the screw is positioned to the side of the treadmill with a distance between the center of the treadmill and lead screw of about 6 inches (15.2 cm). This creates a moment or an overturning load (Figure 3-10) of 108 in-lb (12.2 Nm) for only the treadmill load and up to 2208 in-lb (249.5 Nm) if the treadmill is carrying the full weight of the user. This may cause the screw to jam.

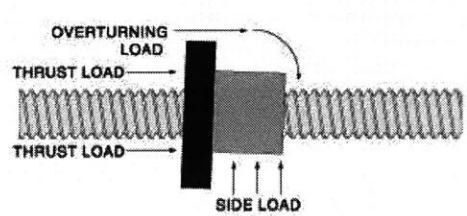

Figure 3-10. Lead screw jamming under a moment load.

Since lead screws inherently can only support axial loading, one design change that could greatly reduce this moment load is to have two lead screws for each treadmill (Figure 3-11). Although this makes the loading on the screws a thrust load, it doubles the number of components

required, thus increasing the cost, and the complexity of the control. If the two screws are not synchronized, both nuts will jam making this technology not optimal to actuate the treadmills.

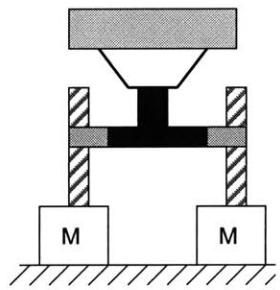

Figure 3-11. Lead screw configuration to reduce overturning load.

3.4.2 Lever

A second design concept utilizes the mechanical advantage of a lever (Figure 3-12).

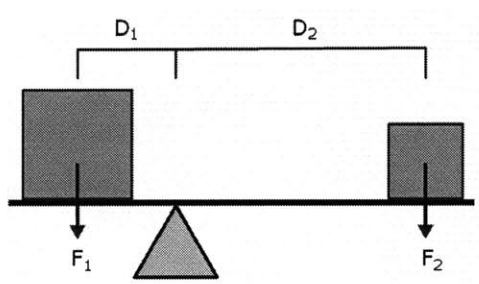

Figure 3-12. Mechanical advantage of a lever.

Equation 3.4 shows that by increasing the length of lever D_2, the amount of force, F_2, required to lift F_1 decreases. Forces and lever arms are inversely proportional and therefore a longer lever arm requires less force to lift a load.

$$F_1 D_1 = F_2 D_2 \quad \text{(eq. 3.4)}$$

Figure 3-13 shows a schematic of how this principle could be applied to the treadmill.

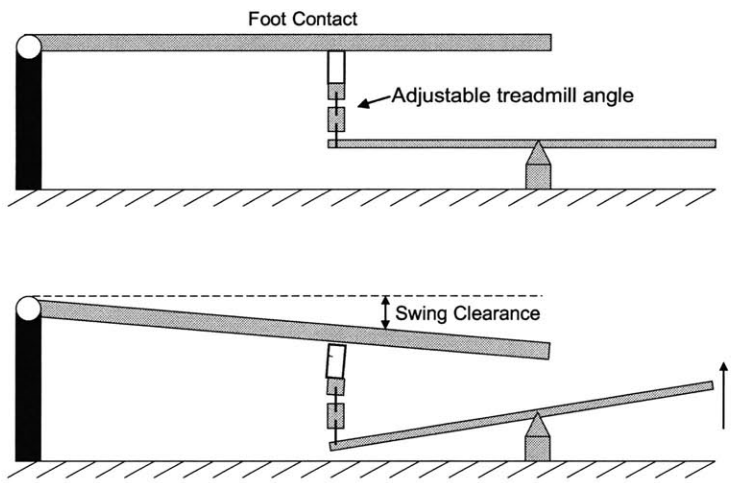

Figure 3-13. Lever design concept.

In order to use a mechanical advantage of even 2:1, the lever would have to extend past the end of the treadmill by 20 inches (50.8 cm) which increases the size of the required footprint. This figure does not include a power source which has many options including a cylinder, cam, or linear actuator. A positive aspect of this design is that the attachment between the treadmill and the lever could include treaded rods so that the angle of the treadmill could be adjusted as needed during therapy. This concept will not allow for a compact design and will not be considered further.

3.4.3 Cam

One method that is compact and could be applied under the treadmill is a cam. Figure 3-14 shows an illustration of this concept.

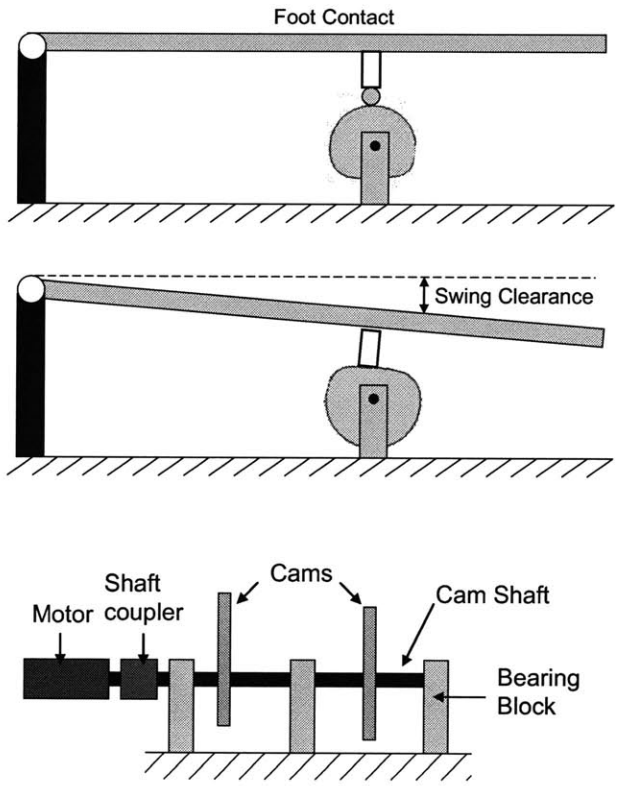

a)

b)

Figure 3-14. Cam design concept, a) cam design side view, b) front view.

While Figure 3-14b shows a single motor and camshaft for both cams, the cams could also be independently controlled with a dedicated motor and shaft. While this would increase the cost of the system, it would also provide flexibility to actuate each treadmill at a different rate, especially for stroke where often only one side is affected. Any motors used in this design would only have to be unidirectional which simplifies the control and reduces the cost. This design concept is very feasible.

3.4.4 Hydraulic Actuator with Return Spring

Hydraulic systems are often utilized for heavy load applications and are found throughout industry in construction equipment, manufacturing machinery, vehicles, and airplanes. Most hydraulic systems run at pressures up to 3000 psi (20.7 MPa) which is why they can support such

heavy loads. There are two main types of hydraulic actuators, spring return and bi-directional. Both options will be discussed.

Regardless of the type of actuator, a hydraulic system needs a reservoir to hold the required volume of hydraulic fluid, a pump to push the fluid into the actuators, an accumulator tank to prevent large changes in the fluid pressure, valves that can either be manually or electrically controlled which open and close to direct the fluid flow, and finally pipe or tubing with fittings to connect these components. By choosing a stiff pipe or tube, the amount of energy lost in the system from expanding the pipe walls is reduced. While flexible tubing is easiest to work with, it greatly decreases the efficiency of the system.

Figure 3-15 shows a schematic of a hydraulic actuator with a spring-aided return. For this configuration, a uni-directional actuator is filled when a valve from the reservoir is opened and fluid is pumped into the cylinder. This pushes the piston in the cylinder up against the spring force, lifting the load. When the treadmill reaches the desired height the valve closes to prevent the fluid from leaving the cylinder. To lower the treadmill, the valve opens to allow fluid flow and the spring forces the actuator down. While having a spring return increases the downward actuation speed, for this application both the raising and lowering stroke must occur in as little as 0.14 seconds total. An increase in spring stiffness increases the lowering speed, but will require larger pumps and valves in order to maintain the required raising speed. Due to this unbalance, this will not be an optimal design choice.

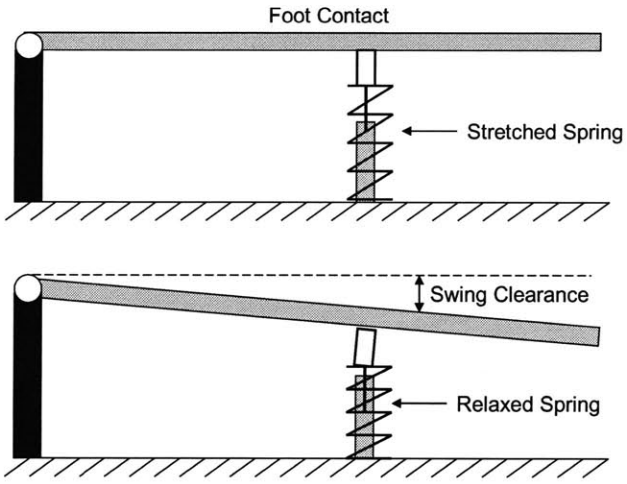

Figure 3-15. Hydraulic actuator with return spring.

3.4.5 Hydraulic Bi-Directional Actuator

A bi-directional actuator has two ports and an internal piston can be pushed either way depending on which port fluid is pumped into (Figure 3-16). This will be a better design than the spring return system because extra power will not be needed to overcome the spring for the rise stroke.

Figure 3-16. Bi-directional hydraulic actuator.

Since these actuators can easily fit under the treadmills and any remaining components can be located to the side, this actuation design is very feasible.

3.4.6 Pneumatic Bi-Directional Actuator

This design concept is very similar to using a hydraulic design, but has the advantage of using air instead of a "wet" fluid. Therefore, in the event of a leak, there would not be any mess. Figure 3-17 shows a bi-directional pneumatic valve which looks quite similar to the hydraulic actuator. A pneumatic system requires many of the same components as with a hydraulic: controllable valves, a reservoir, and tubing and fittings to connect the system. One difference is that a compressor is required instead of pumps in order to produce the required pressure. Most high pressure pneumatic systems run at 100 psi (0.69 MPa), which is 30 times smaller than common hydraulic pressure. This would require a large and loud compressor.

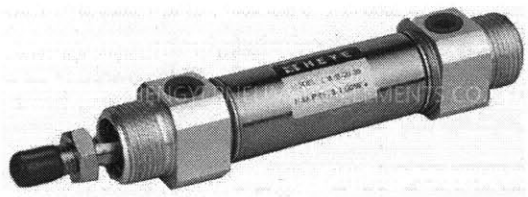

Figure 3-17. Bi-directional pneumatic actuator.

Although this technology could be used, the noise would create a negative environment for both the subject and therapist and will not be pursued further.

3.4.7 Linear Actuator

A solution that would require minimum design time is using off-the-shelf linear actuators (Figure 3-18). These actuators often use ball or worm screws to convert the rotary motion of a motor to vertical motion. A wide range of sizes, speeds, and load capabilities are available and the treadmill requirements are within that range. Position profiles for the actuators can be easily programmed and adjusted depending on the patient. One negative aspect of these actuators is that they often do not have a brake on the motor which means that if power was lost, both treadmills would fall which could cause injury to the subject. Brakes can be added, but this not only adds cost to the system, but it also increases the friction and therefore requires more power to drive. The conveniences of these actuators do come at a cost and an average system with two actuators and a controller for this application was quoted at about $10,000.

Figure 3-18. Linear actuators.

Although linear actuators could be easily implemented, the cost is too high for this prototype and they will not be chosen at this time.

Of the seven design concepts presented, the cam and bi-directional hydraulic actuator had the best balance of being compact, simple to control, straight forward to implement, while still being

low cost for this proof-of-concept prototype. Further detail for each design will be presented next before a final concept is chosen.

3.5 Cam vs. Hydraulic Actuation

In order to determine which actuation design to pursue to actuate the treadmills for the proof-of-concept prototype, both the cam and bi-directional hydraulic actuator design concepts will be examined in greater detail. How amount of power required, space needed both under and outside the treadmill footprint, safety, and ease of fabrication will be considered.

3.5.1 Cam Design Requirements

In order to determine the required speed of the camshaft, the time to complete a stride at different treadmill speeds for subjects at the extremes of the height range must be calculated. Figure 3-19 shows a simplified schematic assuming a 10° toe-off angle and 30° heal strike angle which is average for healthy gait [5]. Trigonometry was used to estimate the length of the stride.

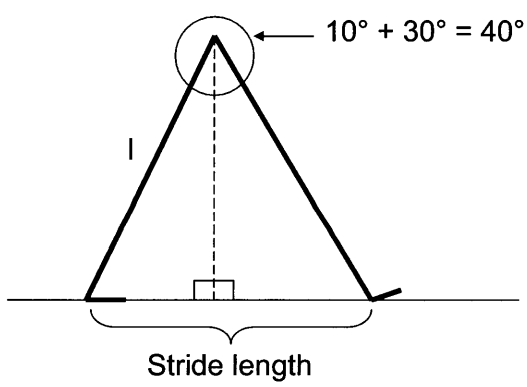

Figure 3-19. Determining required camshaft speed from stride length.

At the slowest treadmill speed, 1.03 ft/sec (0.3 m/s) the 99% male with a leg length of 40.1 inches (101.8 cm) has a stride length of 27.44 inches (70 cm) and each foot will be in stance for 2.22 seconds. Since 60% of gait is stance, then the 2.22 seconds accounts for 60% of the gait cycle time which is 3.7 seconds. The cam would have to rotate at 16.2 rpm (1.68 rad/sec) to

support this gait cycle. At average healthy walking speed, 3.28 ft/sec (1 m/s) the 1% female with a leg length of 29.6 inches (75.2 cm) has a stride length of 20.24 inches (51.4 cm) and each foot will be in stance for 0.51 seconds. The resulting gait cycle is 0.86 seconds and requires a camshaft speed of 70 rpm (7.33 rad/sec). This represents the expected camshaft operating speed range.

The amount of torque required to turn the camshaft in order to actuate the treadmills must be calculated in order to determine the required torque. Applying conservation of power [39]:

$$T\omega = Fv \quad \text{(eq. 3.5)}$$

Where T is the required camshaft torque, ω is the camshaft angular velocity, F is the load on the cam, and v is the linear or vertical velocity of the load. Since actuation only occurs during the swing phase, the cam must lift a load of 18 lbs (8.2 kg). For the 99% male at the slowest treadmill speed, the cam has to lift the treadmill 1.5 inches in 0.74 seconds. The average vertical velocity is 2 in/sec (5 cm/sec) and the approximate maximum velocity is 4 in/sec (10 cm/sec). The required torque is 42.86 in-lb (4.82 Nm). For the 1% female at normal walking speed of 3.28 ft/sec, the cam has to lift the treadmill 1.5 inches in 0.172 seconds. The average vertical velocity is 8.7 in/sec (22 cm/sec) and the approximate maximum velocity is 17.4 in/sec (44 cm/sec). The required torque for this configuration is 42.73 in-lb (4.83 Nm). Converting into horsepower [39],

$$HP = \frac{T\ [ft-lb] * \omega\ [rpm]}{5252} \quad \text{(eq. 3.6)}$$

At 16.2 rpm, 0.011 HP is required, and at 70 rpm, 0.047 HP is needed. If a factor of safety of 2 is included to account for bearing friction and efficiency, the required torque for both the slowest and fastest camshaft speeds is 85.72 in-lb (9.69 Nm) and 0.095 HP at 70 rpm.

Motors already available in the lab are Kollmorgen AC servomotors and their full specifications are listed in Appendix A. Table 3-2 lists the relevant characteristics for the torque/speed curve in Figure 3-20.

Specification	Value
Peak Stall Torque, T_{ps} (in-lb) [Nm]	85.6 [9.67]
Continuous Rated Torque, T_{cr} (in-lb) [Nm]	33.3 [3.76]
Maximum Speed, ω_{max} (rpm)	6000
Rated Speed, ω_r (rpm)	3000

Table 3-2. Motor torque and speed characteristics.

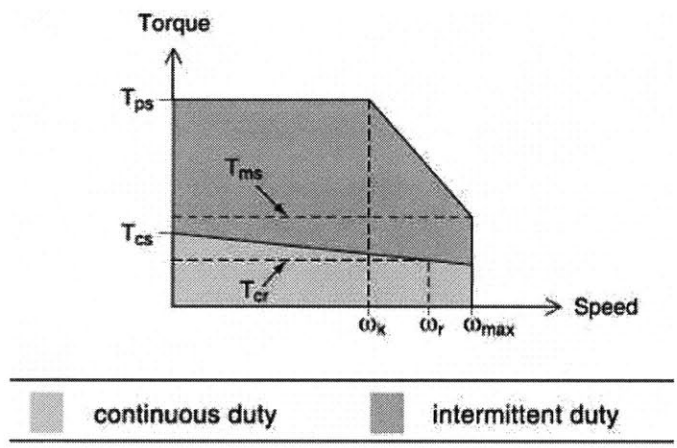

Figure 3-20. Motor torque/speed curve.

For the range of users, the camshaft speed will be between about 16-70 rpm, which is much slower than the 3000 rpm speed that the motor is rated at. Also, the continuous rated torque is only 33.3 in-lb (3.76 Nm), which is less than the estimated 42.86 in-lb (4.83 Nm) calculated before any safety factor was applied. A gear reduction will be required to both reduce the speed of the motor and increase the available output torque. A reduction of 5:1 would supply the required torque including the factor of safety, but a larger reduction will be required to for the desired cam speeds. Since a further gear reduction will increase the amount of output torque, this will not be a problem.

3.5.2 Hydraulic System Requirements

In order to determine the power requirements of a bi-directional hydraulic actuator for this application, the natural frequency of the cylinder, the volume of fluid that must be displaced, and the volumetric flow rate must be determined in order to correctly size the valves and pump. A 1 inch (2.54 cm) diameter bore with a 0.625 inch (1.59 cm) rod with a full stroke of 3 inches (7.62

cm) will be modeled. A stroke of 3 inches was chosen to allow for clearance so that the cylinder piston does not hit the ends of the cylinder during actuation.

Hydromechanical systems can be dynamically modeled as mass-spring systems, and therefore the natural frequency can be calculated [40]. This frequency is important because operating the system above this frequency will result in unstable behavior. The natural frequency, ω_o, of the cylinder is [40]:

$$\omega_o = \sqrt{\frac{E}{M}\left[\frac{A_p^2}{V_p} + \frac{A_n^2}{V_n}\right]} \quad \text{(eq. 3.7)}$$

Where E is the fluid bulk modulus ($2x10^5$ psi [1379 MPa] for oil-based fluids) M is the mass of the load, A_p is the piston area, A_n is the annular area, V_p is the total volume of oil between the valve and piston face, and V_n is the total volume of oil between the annual face and the valve. The load the actuator must lift is the 18 lb treadmill which has a mass of 0.56 slugs (8.17 kg).

The volumes on each side of the piston in Equation 3.7 depend on the position of the piston, and therefore the natural frequency of the actuator changes during the stroke. The natural frequency is at maximum when the piston is fully retracted and decreases to a minimum during the stroke before increasing again at the end of the stroke [38]. The minimum value is important in order to know the frequency limit of the system. This critical value, X_{crit}, of the stroke is calculated by [40]:

$$X_{crit} = \frac{\frac{A_n S}{\sqrt{A_n^3}} + \frac{V_{LR}}{\sqrt{A_n^3}} - \frac{V_{LP}}{\sqrt{A_p^3}}}{\frac{1}{\sqrt{A_n}} + \frac{1}{\sqrt{A_p}}} \quad \text{(eq. 3.8)}$$

Where S is the full stroke length of 3 inches, V_{LR} is the volume of oil in the tubing on the rod side, and V_{LP} is the volume of oil in the tubing on the piston face side. Estimating a total tubing length of 6 inches (15.2 cm) with an inner diameter of 0.75 inches (1.9 cm), the V_{LR} and V_{LP} both equal 2.65 in^3 (43.4 cm^3). The resulting X_{crit} is 3.32 inches (8.4 cm) which means that the

lowest frequency will be when the cylinder is at full stroke of 3 inches. The resulting natural frequency lifting the treadmill is 529.82 rad/sec or 84.32 Hz.

The previous calculation did not consider the compliance in the system, especially the expansion of the pipe under pressure. The rule of thumb is to divide the calculated natural frequency by 3 to account for the compliance resulting in a usable frequency of 176.6 rad/sec or 28.1 Hz [38]. This value is greater than the previously calculated maximum cam speed of 7.33 rad/sec by a factor of 24, so this hydraulic system would not have to operate near its natural frequency.

Another design consideration is the flow rate required to provide the actuation. Again, treating the actuator as a mass-spring system [40]:

$$v_{act} = v_{\max}\left(1 - e^{-\frac{t}{\tau}}\right) \quad \text{(eq. 3.9)}$$

$$\tau = \frac{1}{\omega_{crit}} \quad \text{(eq. 3.10)}$$

$$\omega_{crit} = \frac{\omega_{usable}}{3} \quad \text{(eq. 3.11)}$$

Where v_{act} is the actual velocity at any time t, v_{max} is the maximum required velocity, and τ is the system time constant. For this system, ω_{crit} = 58.9 rad/sec and τ = 0.017 seconds. After one time constant, $v_{act} = 0.63v_{max}$, and after six time constants or 0.102 seconds, the velocity will reach 99.75% of the maximum velocity and six time constants is used to approximate the time required to reach steady state [40]. The maximum required actuator velocity can now be calculated [40]:

$$v_{\max} = \frac{Stroke}{T_t - t_{stab}} \quad \text{(eq. 3.12)}$$

Where the stroke length is 1.5 inches, T_t is the total time allowed for the stroke, and t_{stab} is the time required to reach the maximum velocity (6τ). T_t equals 0.172 seconds which is the time required for actuation of a 1% female walking at 3.28 ft/sec (1 m/s). The resulting v_{max} is 21.43

in/sec (54.4 cm/sec) which is slightly faster than the 17.4 in/sec (44 cm/sec) required for the cam system under the same conditions.

The maximum velocity will determine the required flow rate of the system and is determined by [40]:

$$Q = v_{\max} A_p \quad \text{(eq. 3.13)}$$

Where Q is the volumetric flow rate, normally reported in gallons per minute (gpm). For a maximum velocity of 21.43 in/sec, the resulting required volumetric flow rate is 4.37 gpm (16.54 liter/min). Many off-the-shelf valves are rated for flow rates up to 16 gpm, so this flow rate would be able to be supported.

In order to calculate the required horsepower to drive this system, the acceleration that the load will experience and the force required to provide this acceleration must be found [40]:

$$a = \frac{\Delta v}{t_{stab}} \quad \text{(eq. 3.14)}$$

$$F_a = ma + mg \quad \text{(eq. 3.15)}$$

Where a is the acceleration, the Δv is equal to v_{max}, and F_a is the required force. The resulting acceleration is 17.5 ft/sec^2 (5.3 m/sec^2) and the force required to provide this acceleration against gravity is 27.8 lb (123.7 N). Another consideration is the losses due to seal friction, which is estimated as 0.3*load, which raises the required force to 33.2 lb (147.7 N) [40].

The pressure in the cylinder is the force divided by the piston area which is 42.3 psi. This pressure is well below the rated limit of 3000 psi for most hydraulic systems. Converting the pressure and volumetric flow rate into peak required horsepower [40]:

$$PeakHP = \frac{pQ}{1714} \quad \text{(eq. 3.16)}$$

The peak horsepower for this system to actuate the weight of the treadmill is 0.11 HP. Compared to the estimate of 0.095 HP for the cam system, the two concepts are very comparable in power required.

Additional considerations include the amount of space the system components will require and safety in case of component failure. The cam concept needs two motors, each with a gear reduction, and then two cams, camshafts, and sets of bearings. The cam assembly will be contained under the treadmill and the motors and gear reducers can be incorporated into the BWS frame. This makes the system very compact and simple to maneuver. For the hydraulic system, it may be possible to place all required components under the treadmill which include the pump, reservoir, accumulator, and all tubing. Both system footprints would be the same. In the event of a motor failing in the cam system, the treadmill will stop actuating and there is no risk to the subject. If a valve fails or a leak forms in the system, the actuator will retract, causing the treadmill to suddenly fall which could cause an injury.

Time to implement the design is also important. The cam design has minimal lead time because the motors and controller already exist in the lab, with machining of the cam, camshaft, and bearing supports to be completed. The hydraulic system would require off-the-shelf parts including tubing, fittings, valves, reservoir, and a pump along with machining to mount the components under the treadmill. In addition, a controller for the switching of the valves would have to be purchased and programmed. Both designs would require the treadmill and treadmill motor to be raised to accommodate the actuation mechanism.

Both the cam and hydraulic designs are feasible for this application, but since motors and a controller that are compatible to the cam design are available in the lab, the cam design will be chosen for this proof-of-concept prototype. The detailed design of this system including the cam profile and component material selection is presented in Chapter 4.

3.6 Body Weight Support System

Two basic types of body weight unloading methods exist – using a counterweight or spring-based system. Counterweights have the advantage of being relatively simple and have the ability to provide a constant level of body weight support over a large vertical displacement. One major disadvantage is if the subject experiences a rapid vertical acceleration, the inertia of the counterweight mass causes large perturbations in the support force and can suddenly pull the patient. This interferes with therapy and is the main reason counterweight systems are not an optimal solution.

Springs are able to provide a relatively constant force over a wide range of loads. A Hooke's Law spring for which $F = kx$, where the displacement x is proportional to the force F by the spring constant k, provides more support as the spring is stretched. This is very effective for fall prevention since the increased support is opposite to the fall direction. Different springs can be used to vary the provided support, or the length of a single long spring could be adjusted with a crank.

Once the method of providing the support is determined, it must be attached to the patient's body. Any harnesses used must not interfere with normal gait and harnesses with only one support point should be avoided because they can lead to excessive twisting and instability. As seen in Chapter 2, many devices employ overhead harnesses but one disadvantage is that his method greatly increases the height of the device. In addition, these harnesses require significant time to be put on the patient and are often uncomfortable due to the support straps digging into the skin. A second method is to support the subject from below the waist with a bicycle seat. Figure 3-21 shows a device designed to test the effect of low gravity on running [41]. The label "S" in the figure is a bicycle seat that is supporting the person and "B" is a wide belt to stabilize the person against the seat. This design was used to explore the kinematics of running under simulated low gravity [41], and was employed in the "Elvis-the-Pelvis" robot developed in the Newman lab which manipulates the pelvis during gait therapy [42- 43].

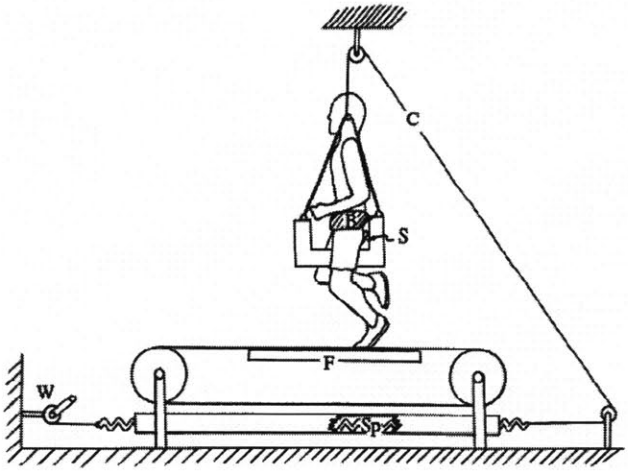

Figure 3-21. Device to test the mechanics of running under simulated low gravity [41].

A second example of bicycle seat style BWS is a leg-assist device currently being developed by Honda (Figure 3-22). The device attaches to the user's waist with a belt and the bicycle seat transmits the support force to the user through the shoes. This device does not provide 100% BWS, and is meant to reduce the amount of energy required for walking and repeated squatting and standing during factory work.

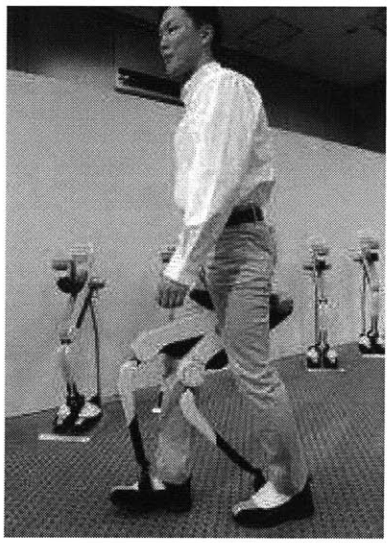

Figure 3-22. Honda leg assist device.

For this prototype, and in order to minimize the size of the device, a bicycle seat style BWS will be implemented. This will require a seat and separate upper body support in order to provide stability and keep the patient secured to the device. This design will require less time than fitting

a patient with a full body harness, will be able to accommodate a large range of subjects, and is similar to the one employed in Elvis-the-Pelvis [42].

The functional requirements of both systems for this device have been presented and the treadmill actuation and body weight support designs have been chosen. The next chapter will provide details of the design of each of these components.

Chapter 4: Detailed Design and Device Assembly

This chapter will provide details of the chosen cam design including the development of the cam profile, camshaft material selection, camshaft bearing selection, and assembly of the cam system. The BWS design and assembly will also be presented.

4.1 Cam Design

While cams are most often associated with automotive valve trains, they are also commonly used in automated assembly machines since they are compact and robust. Cam systems contain two main parts, the cam and the follower. The cam shape dictates the motion profile of the system and the follower, which is coupled to the system, transmits the motion. The treadmills will act as oscillating followers since they are hinged at one end and will oscillate as they are raised and lowered. Wheels bolted to the treadmills will interface with the cams to reduce the friction.

The direction of the follower's motion relative to the axis of cam rotation dictates whether the cam is radial or axial (Figure 4-1).

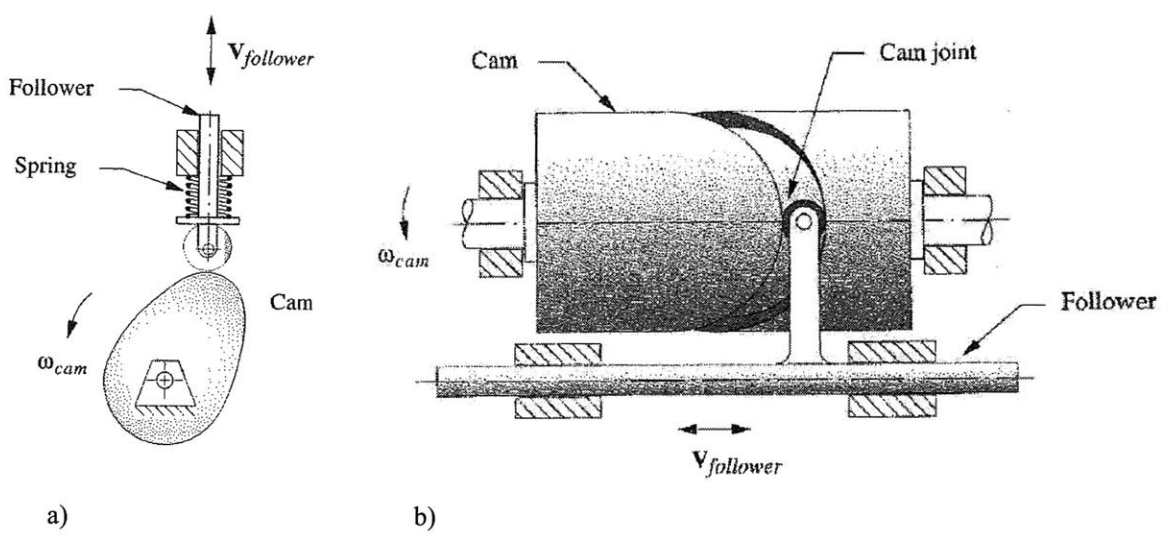

Figure 4-1. a) Radial Cam, b) Axial Cam [39].

This design will use radial cams to actuate the treadmills since they require motion perpendicular to the cam shaft and are less complicated and expensive to manufacture.

Cam motion has three main types: rise, dwell, and fall, often with separate functions for each. Rise and fall transmit motion to the system while dwell maintains a set position. Combining these motions results in two main profile categories: critical extreme position (CEP) and critical path motion (CPM) [39]. CEP is used when only the start and finish positions of the follower are specified and the design is not affected by the motion between these points. In contrast, CPM is constrained between the start and finish positions and this path is critical to the design. The treadmill actuation application requires CEP since the foot contact height and swing clearances are the critical points.

The optimal configuration of the cam profile to provide the swing clearance will be discussed below.

4.1.1 Cam Profile Development

In an average gait cycle, 60% is spent in stance and the remaining 40% spent in the swing phase. During stance, the treadmill should be parallel to the ground to provide a flat walking surface, and during swing the treadmill must lower to provide swing clearance and then rise before the next heel strike. This 60/40 split will be used to design the cam profile with 216° (or 60% of 360°) of high dwell and the remaining 144° for the fall, low dwell (if necessary), and rise. Figure 4-2 shows the timing diagram for both treadmills during one revolution of the cam shaft. The oval indicates the double stance part of the gait cycle where both treadmills are in dwell must be parallel to the ground.

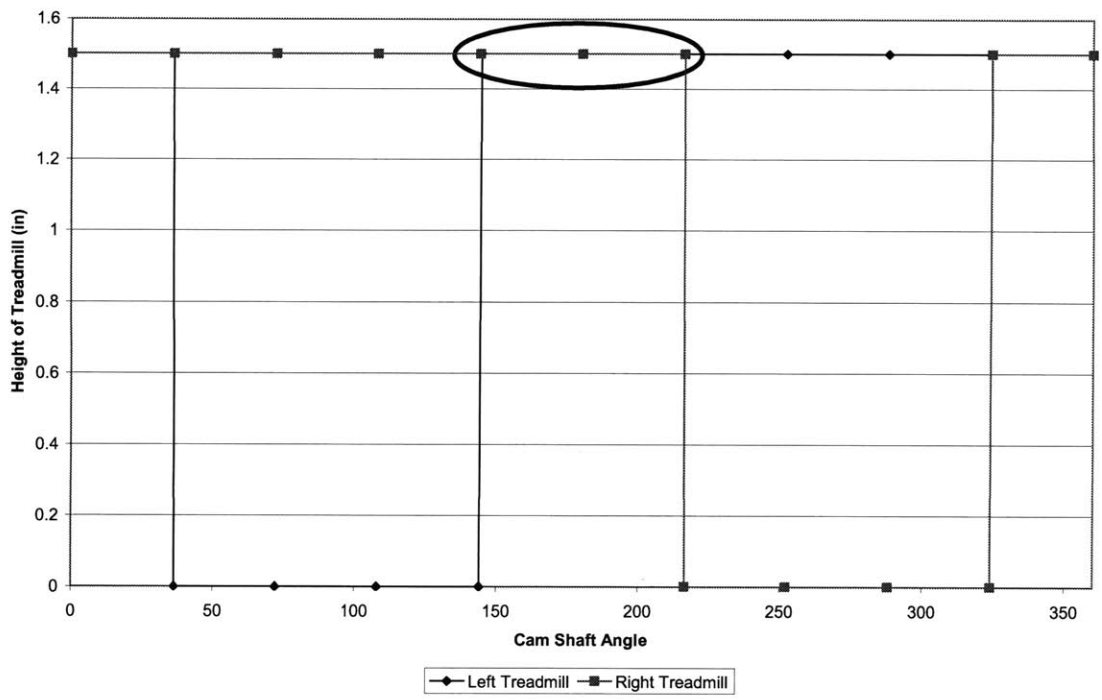

Figure 4-2. Timing Diagram for Both Treadmills.

The dynamics of a cam will be determined by its position (S), velocity (V), acceleration (A), and jerk (J) [39]. These values are often combined in an SVAJ diagram. A naïve SVAJ diagram for a double-dwell, CEP application is shown in Figure 4-3 [39].

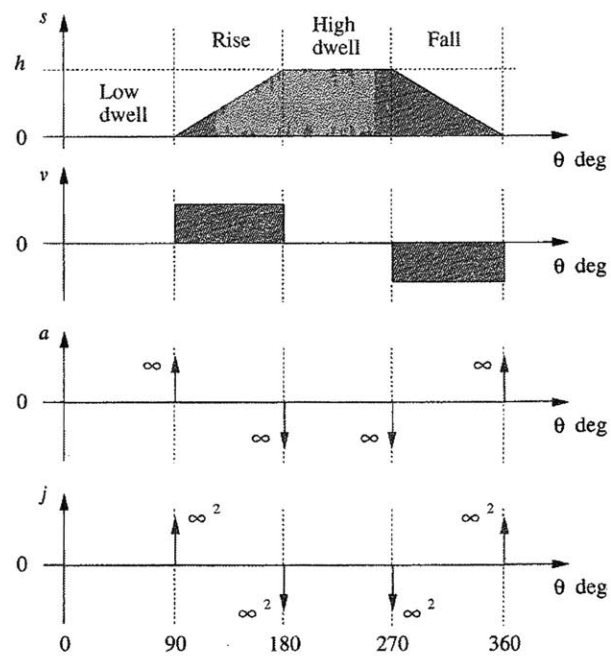

Figure 4-3. Naïve cam SVAJ diagram [39].

Although using straight lines to dictate the position profile does not appear to be a bad choice at first, the resulting derivatives encounter problems at the boundaries of the motion. The discontinuities in the velocity result in infinite spikes in acceleration. In order to achieve infinite acceleration, an infinite force would be required. Even though that is impossible, the sharp corners of the displacement diagram will create very large spikes in acceleration which will in turn create high stresses in the cam and cause rapid wear. The cam will then not retain the desired profile and the motion will change over time, both of which are unacceptable.

The problems with the position profile just presented lead to the fundamental law of cam design which states that the cam-follower function must be continuous through the first and second derivatives of displacement across the entire interval [39]. In addition, the jerk function must be finite across the entire interval. If the acceleration function has any discontinuity, this will cause infinite spikes in the jerk. In order to abide by this law, the displacement function must be at least a fifth-degree polynomial, which will result in a third degree acceleration function [39].

Double-Dwell vs. Single Dwell

A double-dwell motion profile would keep the position stationary both when the foot is in contact with the treadmill and again at the minimum of the treadmill drop for swing clearance resulting in a rise-dwell-fall-dwell motion. A single-dwell motion profile would only keep the position stationary when the foot is in contact with the treadmill and the rise would immediately follow the fall resulting in a rise-dwell-fall motion. Inserting an unnecessary dwell into a motion will result in higher velocities and accelerations which will be illustrated below.

Choosing a Displacement Function

A strategy for avoiding discontinuous derivatives is to use trigonometric functions. A common function used is the cycloidal displacement, or sinusoidal acceleration, and its SVAJ equations are shown below [39].

$$s = h\left[\frac{\theta}{\beta} - \frac{1}{2\pi}\sin\left(2\pi\frac{\theta}{\beta}\right)\right] \quad \text{(eq. 4.1)}$$

$$v = \frac{h}{\beta}\left[1 - \cos\left(2\pi\frac{\theta}{\beta}\right)\right] \quad \text{(eq. 4.2)}$$

$$a = 2\pi\frac{h}{\beta^2}\left[\sin\left(2\pi\frac{\theta}{\beta}\right)\right] \quad \text{(eq. 4.3)}$$

$$j = 4\pi^2\frac{h}{\beta^3}\left[\cos\left(2\pi\frac{\theta}{\beta}\right)\right] \quad \text{(eq. 4.4)}$$

These equations were applied to both double and single-dwell motion profiles. For the double-dwell, the rise occurred over 48° or cam shaft rotation, the first dwell over 216°, the fall 48°, and the second dwell 48°. All calculations were completed using a cam shaft speed of 7.33 rad/sec which is the speed previously calculated that is required for the 1% female walking at 3.28 ft/sec.

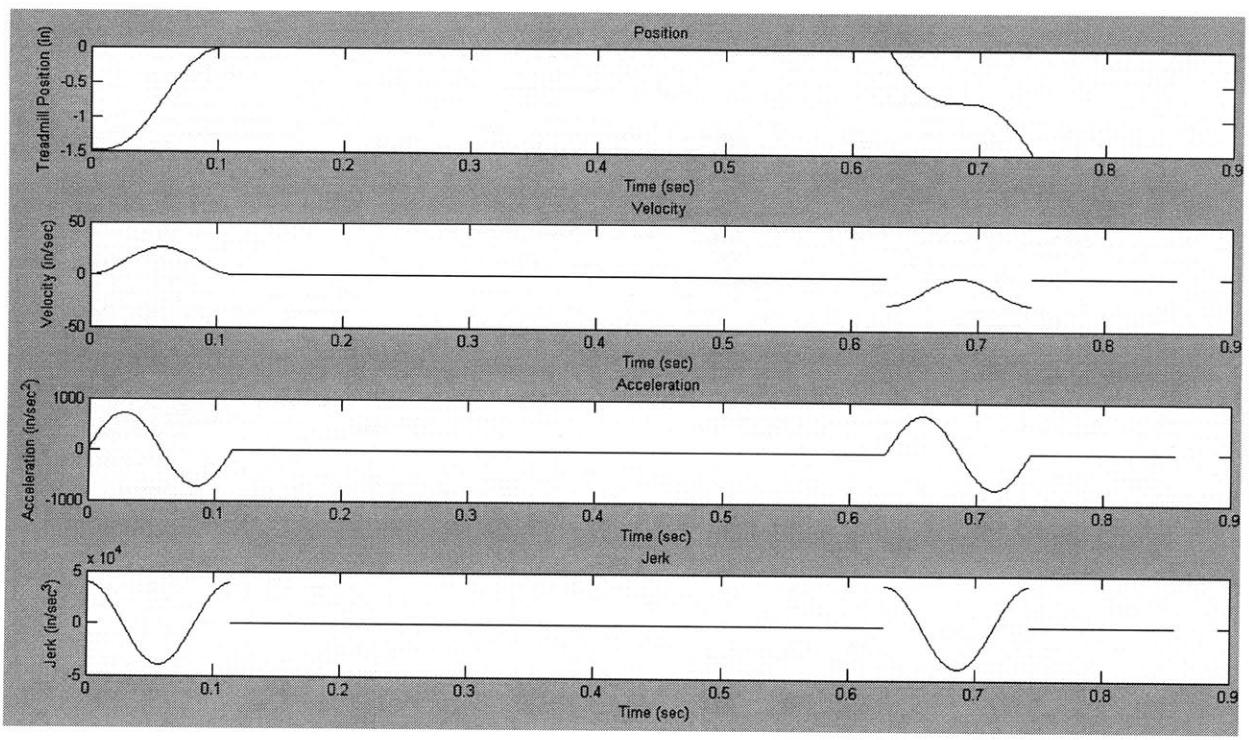

Figure 4-4. Double-Dwell cycloidal position SVAJ diagram.

Figure 4-4 shows that the unnecessary dwell caused a discontinuity in the velocity profile. The maximum resulting velocity is 26.25 in/sec, acceleration 721.5 in/sec^2, and jerk 3.97x104 in/sec^3. Although the jerk is discontinuous, it is finite throughout the motion.

Figure 4-5 shows the resulting SVAJ profile for the cycloidal position single-dwell motion.

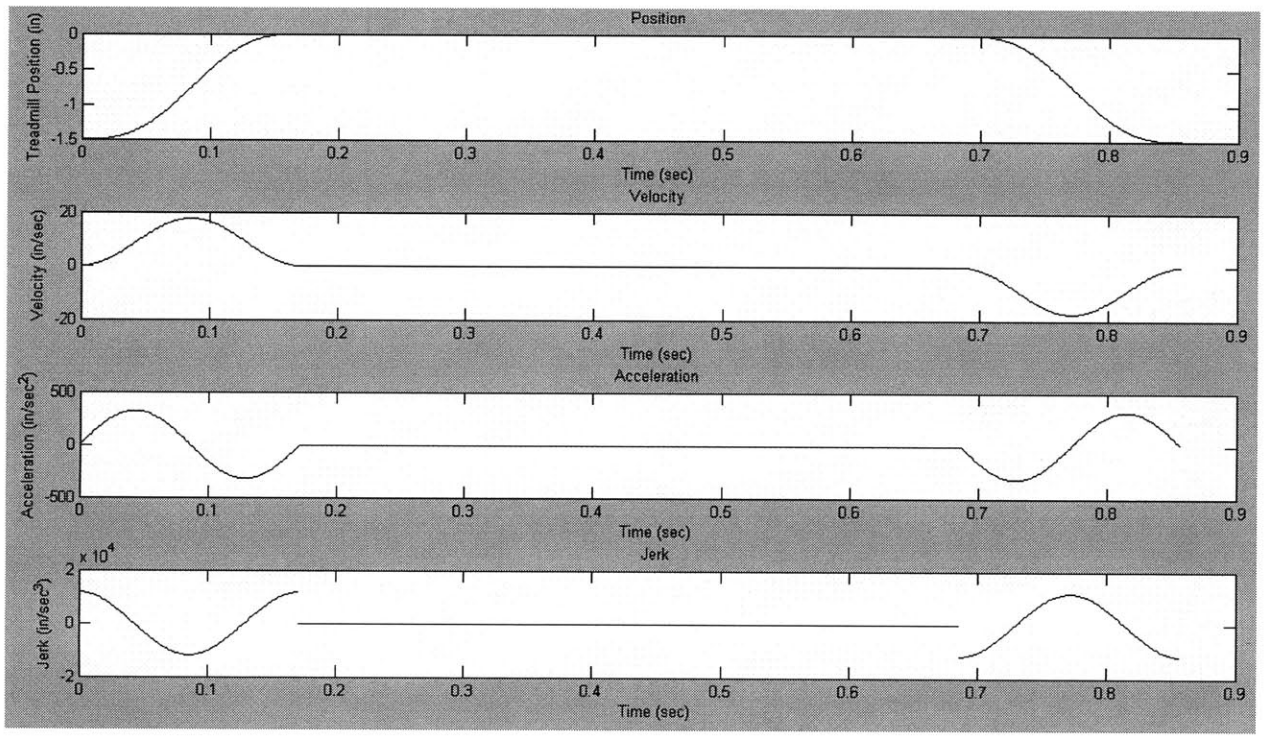

Figure 4-5. Single-Dwell cycloidal position SVAJ diagram.

The maximum resulting velocity is 17.5 in/sec, acceleration 320.7 in/sec^2, and jerk 1.18x10^4 in/sec^3. Clearly, by eliminating the second dwell, the system does not have to actuate the treadmill as quickly, resulting in lower velocity, acceleration, and jerk. There is also no longer a discontinuity in the velocity profile. Further analysis will be completed using single-dwell profiles.

Single-Dwell Double Harmonic

Double harmonic functions contain two cosine terms, one of which is half-period harmonic and a second which is full period harmonic (Equations 4.5 – 4.12) [39]. Figure 4.6 shows the results for the double harmonic functions.

Rise Double Harmonic Equations:

$$s = \frac{h}{2}\left\{\left[1-\cos\left(\pi\frac{\theta}{\beta}\right)\right]-\frac{1}{4}\left[1-\cos\left(2\pi\frac{\theta}{\beta}\right)\right]\right\} \quad \text{(eq. 4.5)}$$

$$v = \frac{\pi}{\beta}\frac{h}{2}\left[\sin\left(\pi\frac{\theta}{\beta}\right)-\frac{1}{2}\sin\left(2\pi\frac{\theta}{\beta}\right)\right] \quad \text{(eq. 4.6)}$$

$$a = \frac{\pi^2}{\beta^2}\frac{h}{2}\left[\cos\left(\pi\frac{\theta}{\beta}\right)-\cos\left(2\pi\frac{\theta}{\beta}\right)\right] \quad \text{(eq. 4.7)}$$

$$j = -\frac{\pi^3}{\beta^3}\frac{h}{2}\left[\sin\left(\pi\frac{\theta}{\beta}\right)-2\sin\left(2\pi\frac{\theta}{\beta}\right)\right] \quad \text{(eq. 4.8)}$$

Fall Double Harmonic Equations:

$$s = \frac{h}{2}\left\{\left[1+\cos\left(\pi\frac{\theta}{\beta}\right)\right]-\frac{1}{4}\left[1-\cos\left(2\pi\frac{\theta}{\beta}\right)\right]\right\} \quad \text{(eq. 4.9)}$$

$$v = -\frac{\pi}{\beta}\frac{h}{2}\left[\sin\left(\pi\frac{\theta}{\beta}\right)+\frac{1}{2}\sin\left(2\pi\frac{\theta}{\beta}\right)\right] \quad \text{(eq. 4.10)}$$

$$a = -\frac{\pi^2}{\beta^2}\frac{h}{2}\left[\cos\left(\pi\frac{\theta}{\beta}\right)+\cos\left(2\pi\frac{\theta}{\beta}\right)\right] \quad \text{(eq. 4.11)}$$

$$j = \frac{\pi^3}{\beta^3}\frac{h}{2}\left[\sin\left(\pi\frac{\theta}{\beta}\right)+2\sin\left(2\pi\frac{\theta}{\beta}\right)\right] \quad \text{(eq. 4.12)}$$

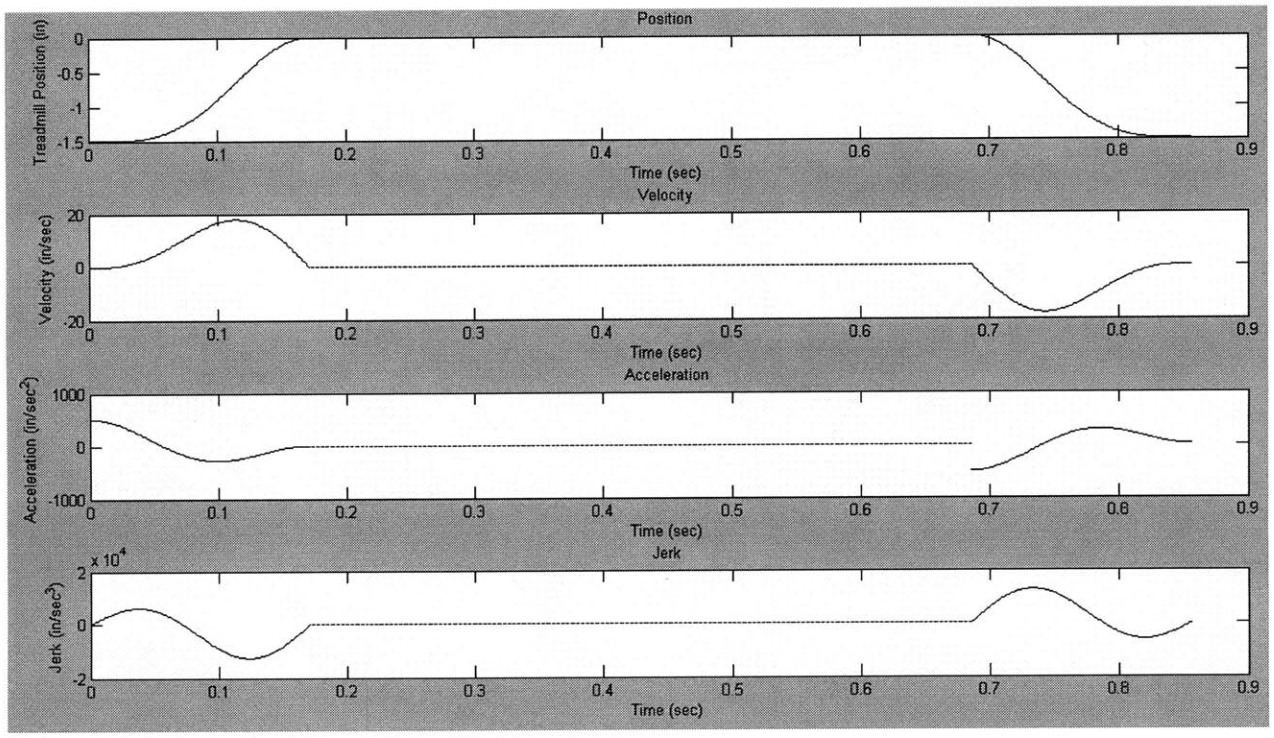

Figure 4-6. Single-Dwell double harmonic SVAJ diagram.

While the double harmonic functions ensured that the acceleration remained continuous between fall and rise, it created a discontinuity in the acceleration at the beginning and end of the dwell. With a maximum velocity of 17.85 in/sec, acceleration 503.7 in/sec^2, and jerk 1.26x10^4 in/sec^3, it is very comparable to the cycloidal results, but the discontinuity is unacceptable.

Single-Dwell Polynomial

Polynomial functions are very versatile and are able to be tailored to any design specification and ensure continuity between cam motions. The SVAJ polynomial equations are derived below in Equations 4.13 – 4.16 and Table 4.1 lists the boundary conditions applied for the rise and fall motions [39]. For the dwell, the velocity, acceleration, and jerk are all zero since the position is constant.

$$s = C_o + C_1\left(\frac{\theta}{\beta}\right) + C_2\left(\frac{\theta}{\beta}\right)^2 + C_3\left(\frac{\theta}{\beta}\right)^3 + C_4\left(\frac{\theta}{\beta}\right)^4 + C_5\left(\frac{\theta}{\beta}\right)^5 + C_6\left(\frac{\theta}{\beta}\right)^6 \quad \text{(eq. 4.13)}$$

$$v = \frac{1}{\beta}\left[C_1 + 2C_2\left(\frac{\theta}{\beta}\right) + 3C_3\left(\frac{\theta}{\beta}\right)^2 + 4C_4\left(\frac{\theta}{\beta}\right)^3 + 5C_5\left(\frac{\theta}{\beta}\right)^4 + 6C_6\left(\frac{\theta}{\beta}\right)^5\right] \quad \text{(eq. 4.14)}$$

$$a = \frac{1}{\beta^2}\left[2C_2 + 6C_3\left(\frac{\theta}{\beta}\right) + 12C_4\left(\frac{\theta}{\beta}\right)^2 + 20C_5\left(\frac{\theta}{\beta}\right)^3 + 30C_6\left(\frac{\theta}{\beta}\right)^4\right] \quad \text{(eq. 4.15)}$$

$$j = \frac{1}{\beta^3}\left[6C_3 + 24C_4\left(\frac{\theta}{\beta}\right) + 60C_5\left(\frac{\theta}{\beta}\right)^2 + 120C_6\left(\frac{\theta}{\beta}\right)^3\right] \quad \text{(eq. 4.16)}$$

Boundary Condition Imposed				
Function	θ	θ/β	Rise Boundary Condition	Fall Boundary Condition
s	0	0	-h	0
v	0	0	0	0
a	0	0	0	0
s	β	1	0	-h
v	β	1	0	0
a	β	1	0	0
s	β/2	0.5	-h/2	-h/2

Equation Resulting		
Exponent	Rise Coeffcient	Fall Coeffcient
0	-h	0
1	0	0
2	0	0
3	10h	-10h
4	-15h	15h
5	6h	-6h
6	0	0

Table 4-1. Boundary Conditions for Single-Dwell Polynomial Functions.

Figure 4-7 shows the resulting SVAJ diagram for the single-dwell polynomial functions.

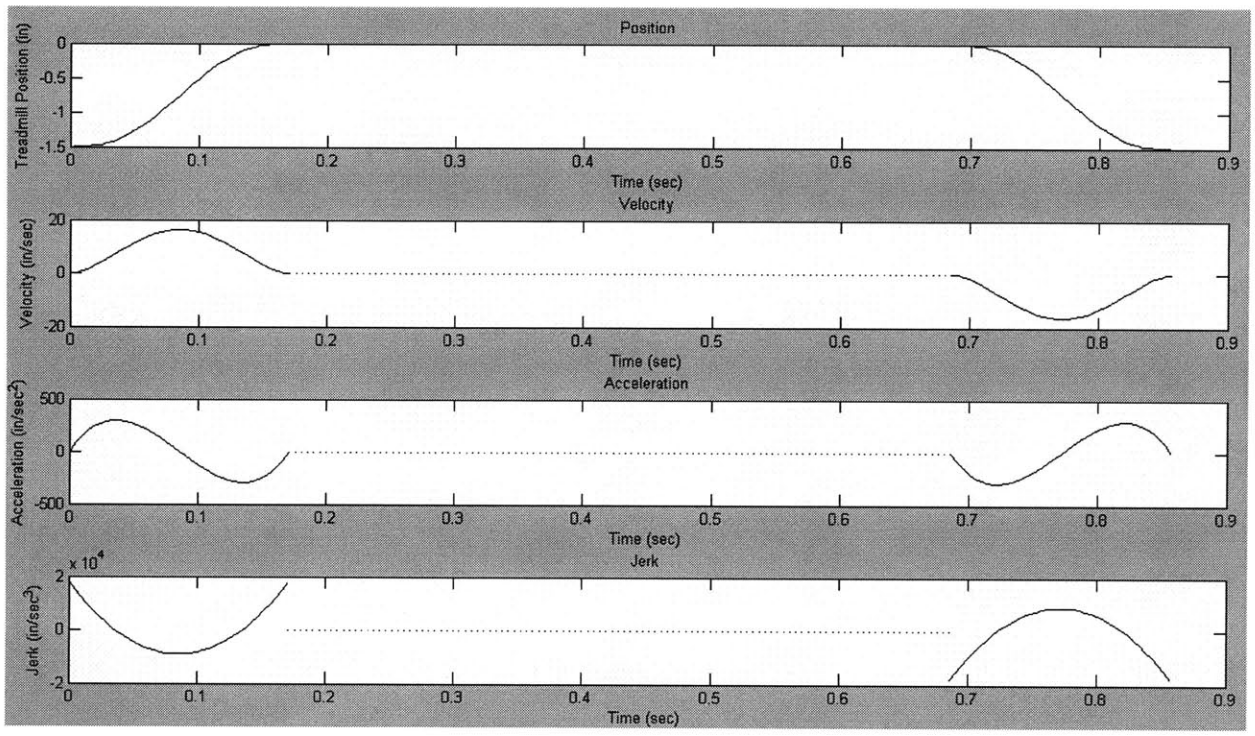

Figure 4-7. Single-Dwell polynomial SVAJ diagram.

The polynomial functions maintained continuity through acceleration and the jerk has a finite value throughout the cycle. With a maximum velocity of 16.41 in/sec, acceleration 294 in/sec^2, and jerk 1.79x10^4 in/sec^3, it is very comparable to the both the cycloidal and double harmonic results, and has the lowest maximum velocity and acceleration. A comparison of all three single-dwell position profiles is shown in Figure 4-8.

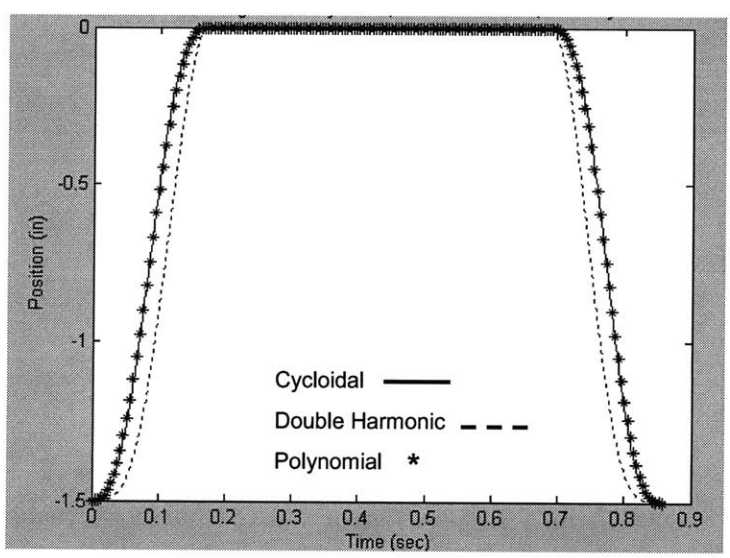

Figure 4-8. Cycloidal, double harmonic, and polynomial position functions.

Both the cycloidal and polynomial profiles are almost indistinguishable from each other, while the double harmonic has the steepest slope. Since the polynomial function has the lowest velocity and acceleration, and comparable jerk, it will be chosen to design the cam profile.

4.1.2 Pressure Angle

Once the SVAJ functions have been defined, the next step is to size the cam. This size is affected by the pressure angle and the radius of curvature of the cam [39]. These values are determined by the prime circle radius, R_p. As shown in Figure 4-9, the prime circle radius is the smallest circle that can be drawn tangent to the center of the roller follower. Conceptually, when creating a radial cam, one can visualize taking the S diagram and wrapping it around the prime circle to create the cam surface [39].

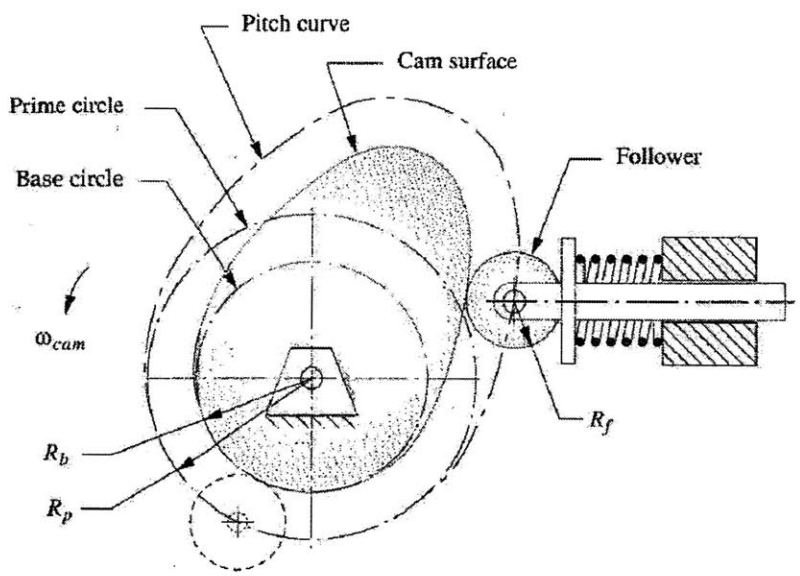

Figure 4-9. Prime radius for a cam roller follower [39].

The pressure angle, φ, is the angle between the velocity (direction of motion) of the follower and the normal force of the follower on the cam surface (see Figure 4-10). When φ = 0°, all of the force from the cam is transmitted to the follower, and none to slip velocity. In contrast, when φ = 90°, no motion will be transmitted to the follower and it will slip. The rule of thumb for oscillating roller followers is to keep the pressure angle between +/- 35° to avoid slippage [39].

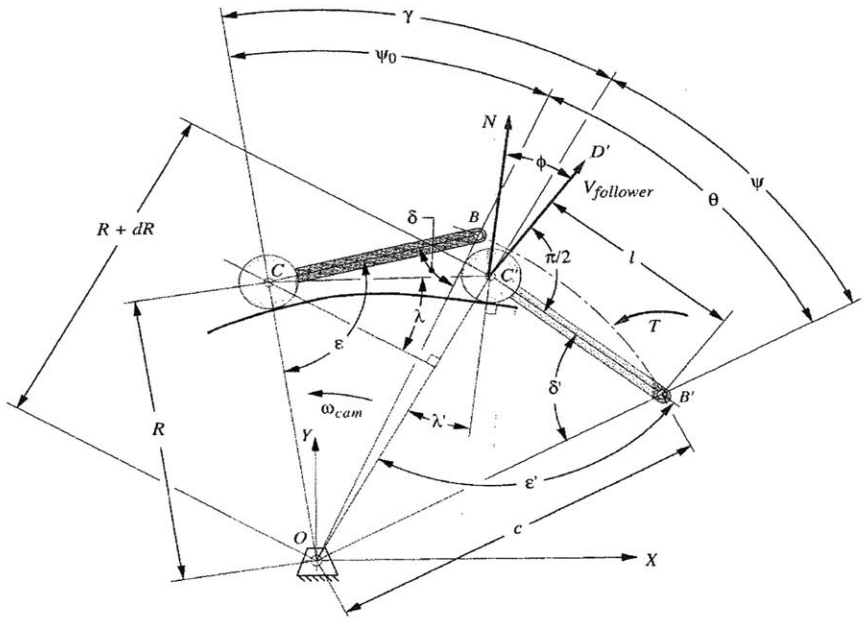

Figure 4-10. Pressure angle of an oscillating roller follower [39].

The equation for the pressure angle is derived from the geometry in Figure 4-10. The equations for rise, dwell, and fall are presented below in Equations 4.17 – 4.20 [39].

$$R_p = \sqrt{l^2 + c^2 - 2lc\cos\delta} \quad \text{(eq 4.17)}$$

$$\psi = \cos^{-1}\left(\frac{c^2 + R_p{}^2 - l^2}{2R_p c}\right) \quad \text{(eq 4.18)}$$

$$\varphi_{rise,fall} = -\frac{\pi}{2} + \sin^{-1}\left(\frac{c}{R}\sin\delta\right) + \tan^{-1}\left(\frac{1}{\dfrac{R_p{}^2}{lc\sin\delta\dfrac{d\delta}{d\theta}} + \dfrac{c^2 - R_p{}^2 - l^2}{2R_p c\sin\psi}}\right) \quad \text{(eq 4.19)}$$

$$\varphi_{dwell} = -\frac{\pi}{2} + \sin^{-1}\left(\frac{c}{R_p}\sin\delta\right) \quad \text{(eq 4.20)}$$

The minimum R_p that results in a pressure angle between +/- 35° is 5.75 inches, shown in Figure 4-11. The maximum rise pressure angle is -35° and the fall pressure angle is 24°. As can be seen from the equations, the larger the R_p, the smaller the pressure angle will be, but this will also

increase the size and the cost of the cam. The minimum R_p that produces an acceptable pressure angle is the optimal choice.

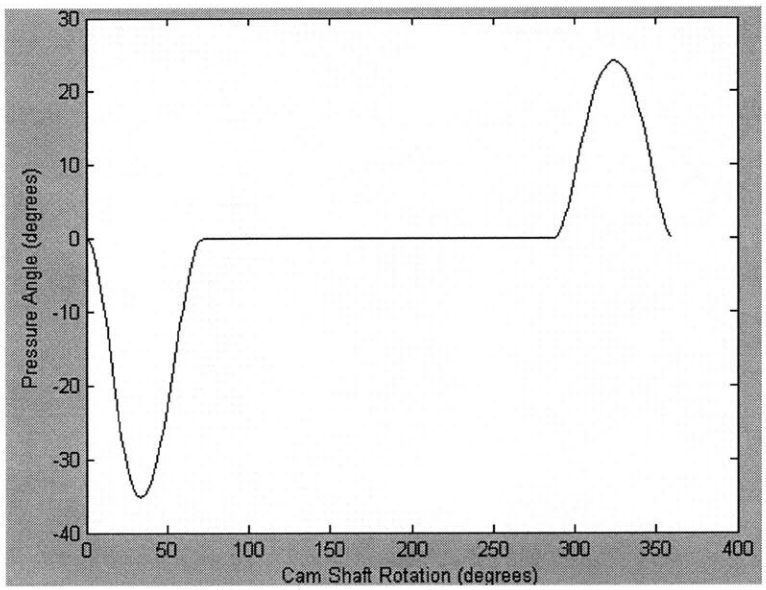

Figure 4-11. Pressure angle for a cam with R_p = 5.75 inches.

This R_p of 5.75 inches will now be used to calculate the cam surface profile coordinates.

4.1.3 Cam Surface Coordinates

Since the R_p passes through the center of the roller follower, the size of the follower will affect the size of the cam. A follower with a radius of 0.5 inches is a common available size and will be used to determine the surface profile of the cam.

Figure 4-12 shows the geometry of the oscillating roller follower system. The sign convention of the rotation of the arm and cam is negative for clockwise motion and positive for counterclockwise motion.

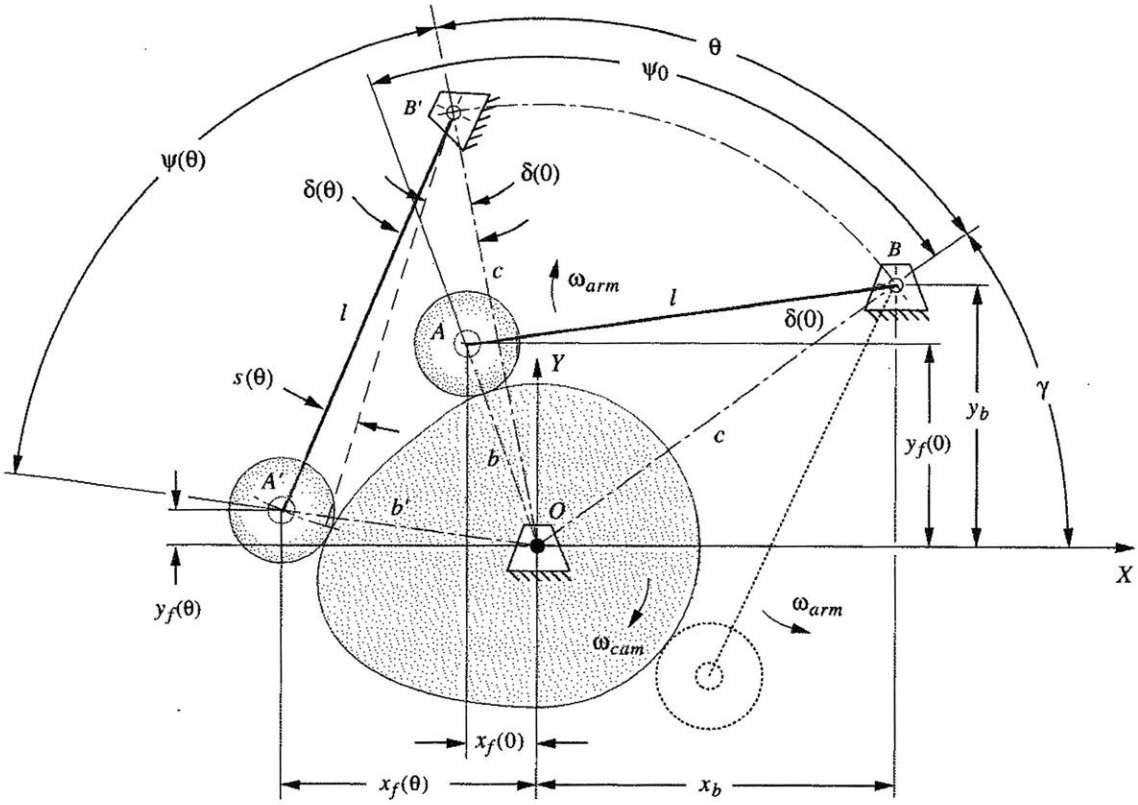

Figure 4-12. Cam profile of an oscillating roller follower [39].

Equations 4.21 – 4.30 were derived from this geometry and used to calculate coordinates of the path of the center of the follower, x_f and y_f, the surface coordinates x_s and y_s of the cam [39].

$$\gamma = \tan^{-1}\left(\frac{y_b}{x_b}\right) \quad \text{(eq. 4.21)}$$

$$b = \sqrt{c^2 + l^2 - 2cl\cos\delta(\theta)} \quad \text{(eq. 4.22)}$$

$$\delta(\theta) = \cos^{-1}\left(\frac{c^2 + l^2 - b^2}{2cl}\right) \quad \text{(eq. 4.23)}$$

$$\psi(\theta) = \cos^{-1}\left(\frac{c^2 + b^2 - l^2}{2cb}\right) \quad \text{(eq. 4.24)}$$

$$x_f(\theta) = b\cos\left[\gamma - \text{sgn}(\omega_{cam})\theta - \text{sgn}(\omega_{arm})\psi(\theta)\right] \quad \text{(eq. 4.25)}$$

$$y_f(\theta) = b\sin\left[\gamma - \text{sgn}(\omega_{cam})\theta - \text{sgn}(\omega_{arm})\psi(\theta)\right] \quad \text{(eq. 4.26)}$$

$$\lambda(\theta) = \theta + \gamma - \delta(\theta) \quad \text{(eq. 4.27)}$$

$$\sigma(\theta) = \lambda(\theta) + \frac{\pi}{2} + \varphi(\theta) \quad \text{(eq. 4.28)}$$

$$x_s(\theta) = x_f(\theta) \pm \text{sgn}(\omega_{arm}) R_f \cos\left[\sigma(\theta)\right] \quad \text{(eq. 4.29)}$$

$$y_s(\theta) = y_f(\theta) \pm \text{sgn}(\omega_{arm}) R_f \sin\left[\sigma(\theta)\right] \quad \text{(eq. 4.30)}$$

Figure 4-13 shows the resulting surface coordinates. The innermost curve is the cam surface, the middle curve is the path of the center of the follower, and the outermost curve is the path of the outer diameter of the follower. The point is the origin of the cam and where the camshaft would be centered.

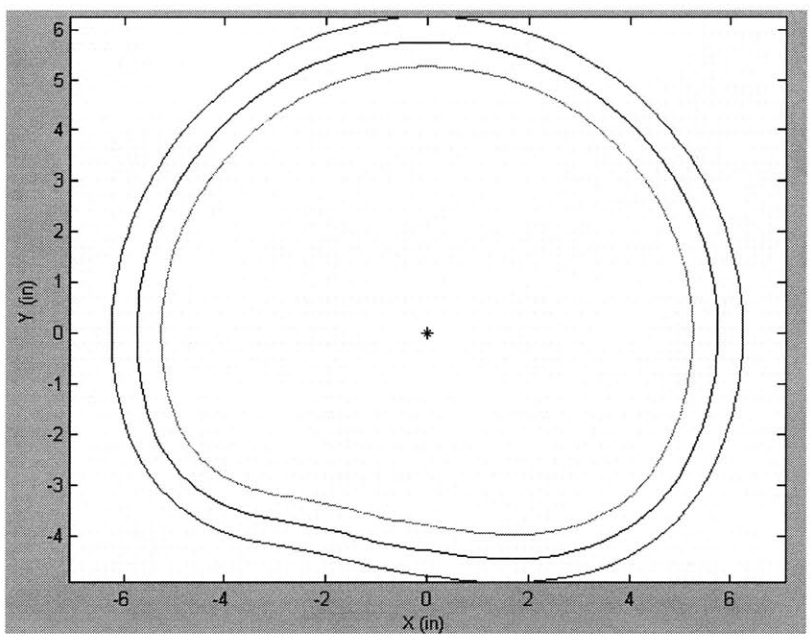

Figure 4-13. Cam surface coordinates.

The cam is 10.5 inches across at its largest diameter and 9 inches at the smallest diameter and will be able to be located under the treadmills by raising the walking surface 12 inches. This profile was first imported into Solidworks to create a three-dimensional model and then exported to MasterCam to write a program to mill the profile from 0.5 inch thick 6061 aluminum.

Increasing the swing clearance requirement greatly increases the size of the cam and the maximum velocity, acceleration, and jerk. A swing clearance of 4.5 inches would require a cam

that is at least 21 inches at its largest diameter. A cam of this size would not be able to be located under the treadmills and would be very expensive to manufacture. If the clearance specification has to be greatly increased, a cam design would not be the optimal solution.

4.2 Camshaft Material Selection

The camshaft must be able to withstand the weight of both the treadmill and subject without deformation that may alter the cam rotation or yielding which may cause the shaft to fail. This is very important since the camshaft transmits the torque from the motors to the cam to provide actuation. During swing phase, one treadmill will have no load, while the other will be supporting 100% of the subject's weight (assuming no body weight support). If the subject weighs 350 lbs (158.8 kg), and each treadmill weighs 18 lbs (8.2 kg), the load will total 368 lbs (166.9 kg).

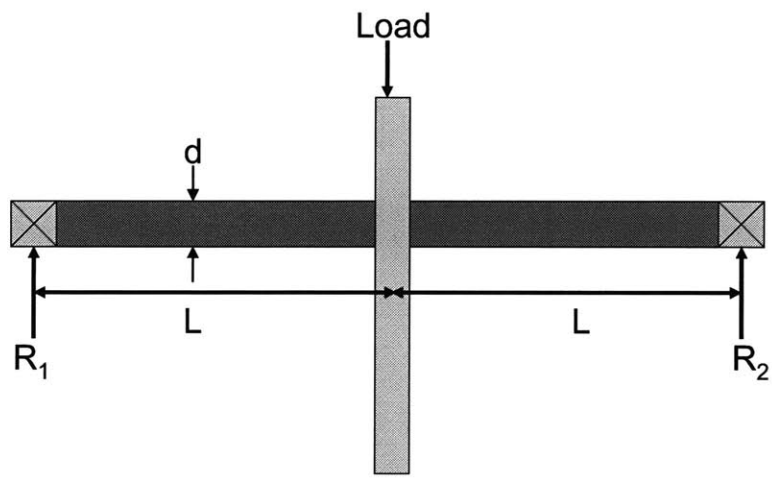

Figure 4-14. Loading of camshaft.

The total length of the camshaft between the bearings is 4 inches (10.2 cm) and the cam is located approximately in the middle (Figure 4-14). This creates a symmetric free body diagram where Load = $R_1 + R_2$ (where $R_1 = R_2$). To facilitate rotation and mating with bearings, a circular cross-section has been chosen with an area moment of inertia, I, and deflection under loading, v [44]:

$$I = \frac{\pi r^4}{4} \quad \text{(eq. 4.31)}$$

$$v = -\frac{Load * L^3}{48EI} \quad \text{(eq. 4.32)}$$

Where r is the radius, L is the length from the end of the shaft to the loading point, and E is the modulus of elasticity of the material. A factor of safety of 4 will be applied to the total weight to account for the shock loading caused by the collision between the heel and treadmill for each step.

A common material used for shafts, gears, and axels due to its good fatigue, abrasion, and impact resistance while remaining highly machinable are 41XX or "chrome-moly" steels. These steels get their name from the addition of chromium and molybdenum and have an improved strength to weight ratio compared to standard 1020 steel. 4140 contains between 0.8 – 1.1% chromium and 0.15 – 0.25% molybdenum and has a modulus of elasticity of 29,700 ksi (205 GPa) and a yield strength of 60,200 psi (415 MPa) [45]. For a 1 inch (2.5 cm) diameter shaft of 4140, the resulting deflection with 1472 lbs (887.7 kg) of load (4*368) is 1.68×10^{-5} inches (4.3×10^{-5} cm). This deflection will not be noticeable for this application.

The stress, σ, caused from this loading must also be examined to ensure it is not larger than the yield stress of the material [44].

$$\sigma = \frac{Load}{Area} \quad \text{(eq. 4.33)}$$

For a load of 1472 lbs (667.7 kg), and the cross-sectional area of a 1 inch diameter circle, the resulting stress is 1874.2 psi (12.9 MPa), which is over 32 times smaller than the yield strength of 60,200 psi. A 1 inch diameter shaft of 4140 steel is acceptable for this design.

4.3 Camshaft Bearing Selection

In order to minimize the rotary friction in the system and transmit the torque from the motors, the proper bearings must be chosen. The camshaft load is primarily radial, will be operating at constant and relatively low speeds, and the stepping of the subjects will create shock loading. Below is a brief description of common types of bearings that support radial loads, and the conditions for which they are best suited.

4.3.1 Ball Bearings

Radial ball bearings have two basic types, non-filling slot or Conrad type (filling slot) [46]. Bearings can have more than one row of balls in order to support larger loads. Conrad ball bearings have a deeper raceway in both the inner and outer rings (Figure 4-15). The deeper raceway allows the bearing to withstand heavy radial and moderate bi-directional thrust loads. The filling slot ball bearing contains more balls than an equivalent-sized Conrad type, giving it a higher radial load capacity, but due to the filling slots, these bearings can only withstand small thrust loads. If the maximum rated thrust load is exceeded, the balls will roll over the filling slots, causing severe damage and even failure to the ball bearing. Both of these bearings are not best suited to withstand shock loading.

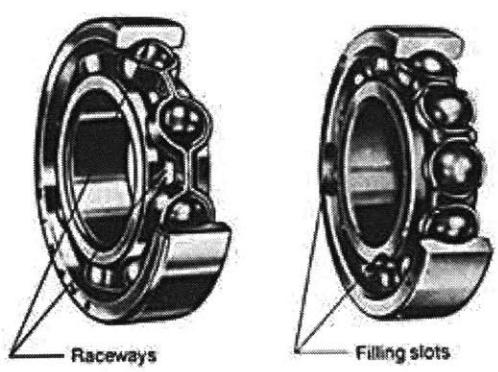

a) b)

Figure 4-15. a) Conrad ball bearing, b) filling slot ball bearing [46].

4.3.2 Angular Contact Bearings

Angular contact bearings use axially asymmetric races so that axial loads pass in a straight line through the bearing, while radial loads push against the races axially (Figure 4-16) [46]. This asymmetry makes the angle of contact on the inner and outer races equal. Angular contact bearings are able to support both radial and axial loads, and as the contact angle increases between 10° and 45°, the bearing's ability to axial loads increases, but its ability to withstand radial loads decreases.

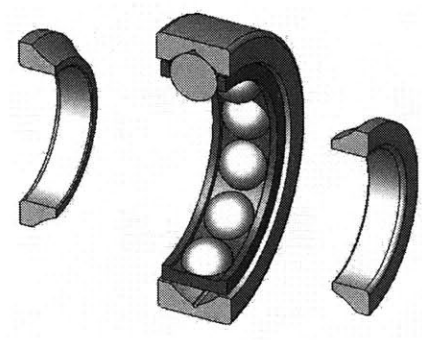

Figure 4-16. Angular contact bearing.

Since angular contact bearings can only support axial loads in one direction, they are often used in matched pairs. This allows for bi-axial loads to be supported and increases the stiffness of the system [46].

4.3.3 Cylindrical Roller Bearings

Cylindrical roller bearings (Figure 4-17) have both the highest radial and speed capacity for a given cross section of any type of roller bearing [46]. A non-locating cylindrical bearing allows axial shaft movement which may occur due to thermal expansion or assembly tolerance build-up. Cylindrical bearings are best at supporting radial loads, and if the outer rings have ridges, light axial loads as well. The maximum rated speed the bearing can tolerate is determined by the roller length–to–diameter ratio. For general use, a roller length equal to the roller diameter provides the optimal combination of load and speed limits.

While roller bearings can support greater loads than ball bearings, roller bearings are more sensitive to misalignment. Angular misalignment between the shaft and housing can cause non-uniform loading of the rollers, leading to reduced bearing life [46].

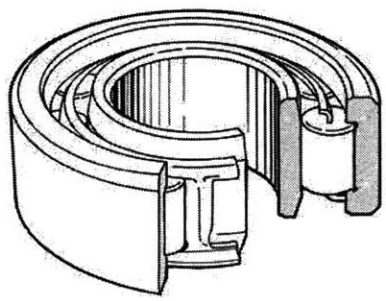

Figure 4-17. Cylindrical roller bearing [46].

4.3.4 Needle Roller Bearings

Needle roller bearings (Figure 4-18) are similar to cylindrical roller bearings, but have a smaller roller diameter-to-length ratio [46]. Needle roller bearings have a higher load capacity than a single row ball bearing with the same outer diameter.

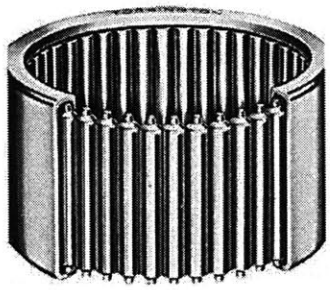

Figure 4-18. Needle roller bearing [46].

4.3.5 Tapered Roller Bearings

The geometry of a tapered roller bearing (Figure 4-19a) makes it capable of supporting heavy radial, axial, and any combination of the two loads [46]. Unlike the previous bearings, tapered roller bearings come in two pieces, the cone and the cup (Figure 4-19b and c). When a tapered

roller bearing is loaded, the load is broken down into three components: a radial component (perpendicular to the camshaft), an axial or thrust component (parallel to the camshaft), and a roller seating force which maintains contact between the rollers in the cup and the cone [46].

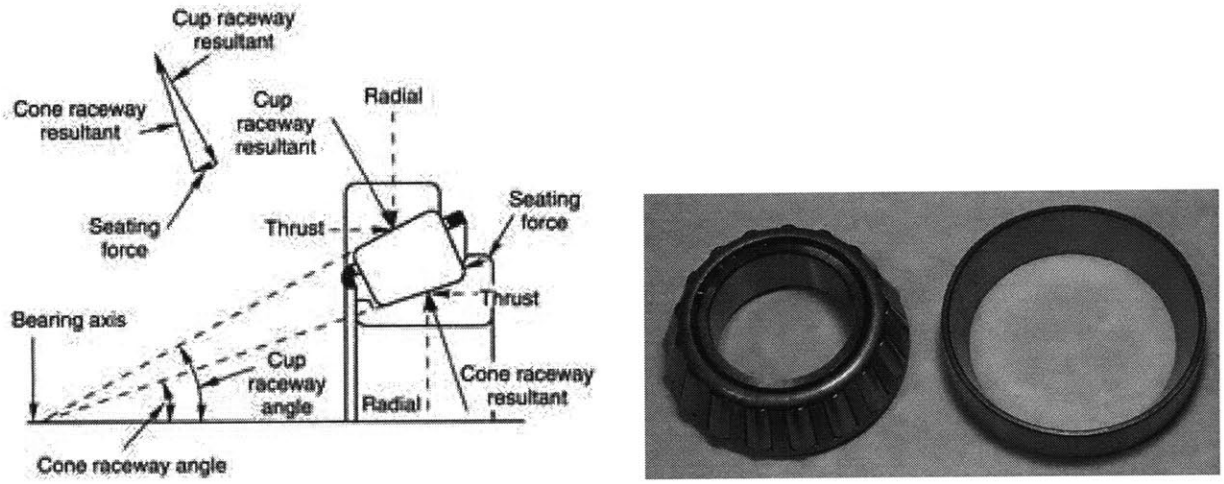

a) b) c)

Figure 4-19. a) cone geometry of tapered roller bearing, b) tapered roller bearing cone, c) cup.

Another benefit of the bearing geometry is that the rollers rotate with a true rolling motion without the rollers skidding over the raceway. This makes the rollers wear evenly and prolongs bearing life [46]. In addition, the race and roller angles can be matched to the application: shallow angles for predominantly radial loads and steeper angles for a greater thrust capacity. Tapered roller bearings tolerate misalignment well and because the separate pieces can be adjusted during assembly.

Because tapered roller bearings are separate pieces, they must be preloaded in assembly. Figure 4-20 shows a common preloading method [47].

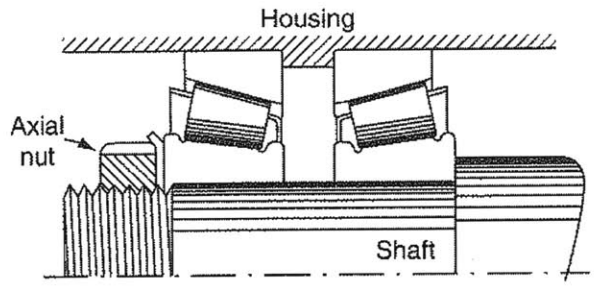

Figure 4-20. Method for preloading tapered roller bearings [47].

Since tapered roller bearings are able to support radial loads, shock loads, accommodate shaft misalignment, and have adjustable clearance, they will be chosen to support the camshaft. The bearings were sized to fit with the 1 inch diameter camshaft and the full specifications are listed in Appendix A.

4.4 Full Cam System

Figure 4-21 shows a Solidworks model of the treadmill cam system with the roller followers that are bolted to the treadmills. Both cam assemblies are identical with the exception of the orientation of the camshaft. Both non-threaded ends must be facing towards the outside of the treadmill in order to couple with the gear reducer and motors.

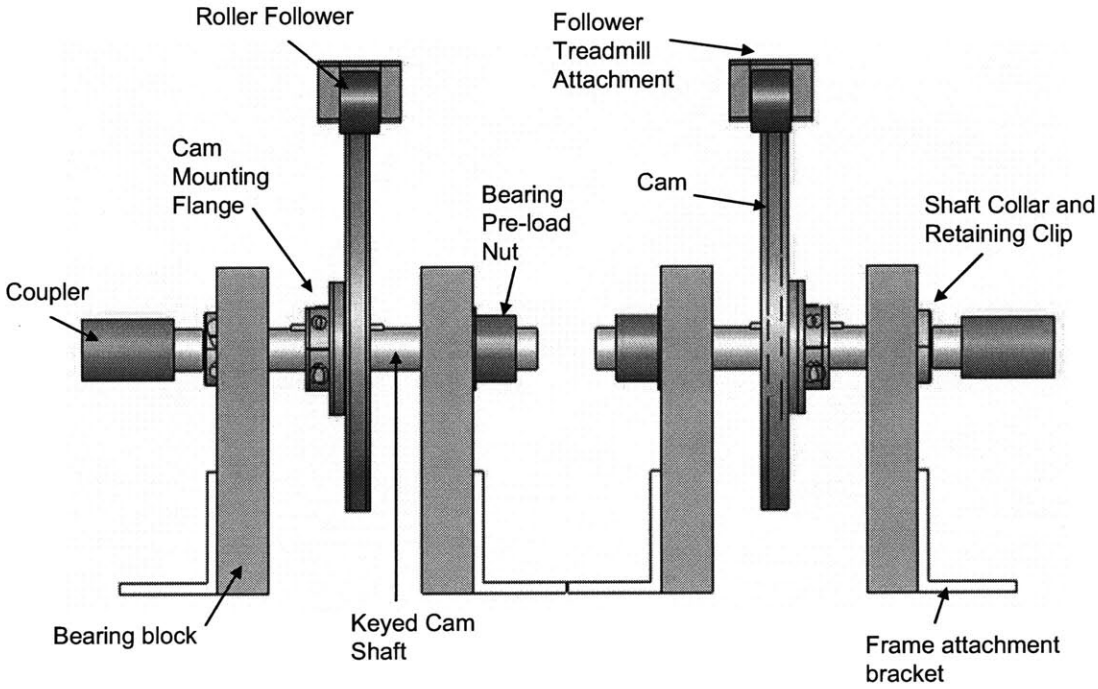

Figure 4-21. Cam system for treadmill actuation.

Figure 4-22 shows a cross-sectional view of a single cam subassembly highlighting the bearing pre-load design. The bearing blocks were machined with a press fit for the taper roller bearing cup and a shoulder to prevent axial motion of the cups. The pre-load on the pair of taper roller bearing cones is created by the clamp collar on the motor coupling side of the camshaft and the

nut on the opposite threaded end. The position of the nut on the shaft will determine the force on the bearings. The nut was positioned so that the cam was able to spin freely without any lateral motion. A lock nut (not shown in the figure) was added to prevent the pre-load nut from moving.

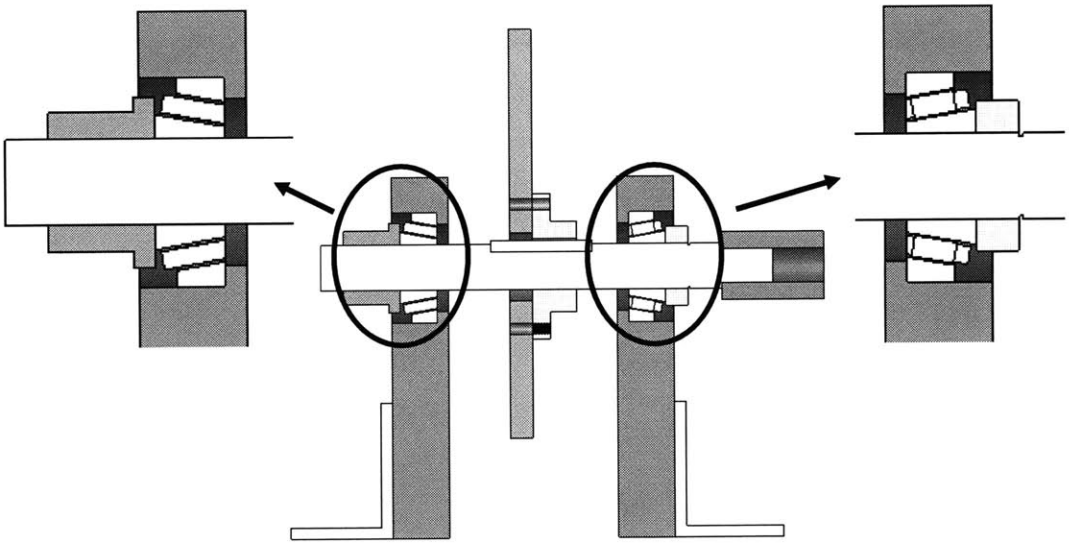

Figure 4-22. Detail of bearing pre-load design.

Finally, Figure 4-23 shows both machined cam assemblies clamped to a table before they were installed in the TreadClimber frame.

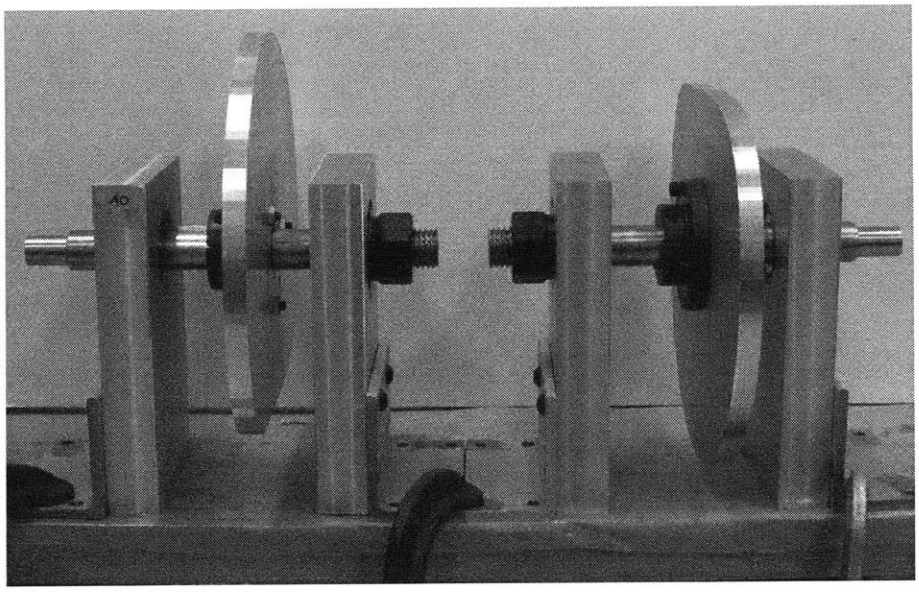

Figure 4-23. Assembled cam subsystem.

4.5 Treadmill Modifications

In order to accommodate the cam actuation system, the treadmills and the treadmill motor had to be raised 12 inches. Four lengths of 80/20 aluminum 3 inch square extrusion (details provided in section 4.6.1) were used to build the required distance (Figure 4-24). The TreadClimber treadmill assembly originally bolted to the frame with four bolts, so a length of extrusion was bolted to the frame to provide a foundation and the top layer was bolted to the treadmills. Each length was secured to the rest of the stack using plates specifically designed for use with 80/20.

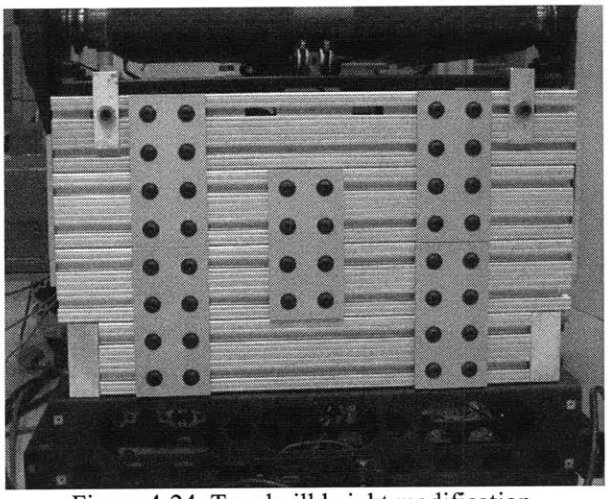

Figure 4-24. Treadmill height modification.

The motor that drives the treadmill was originally bolted to the base of the frame, and in order to use the original drive belt, the motor was also raised the same 12 inch distance with 80/20 extrusion (Figure 4-25).

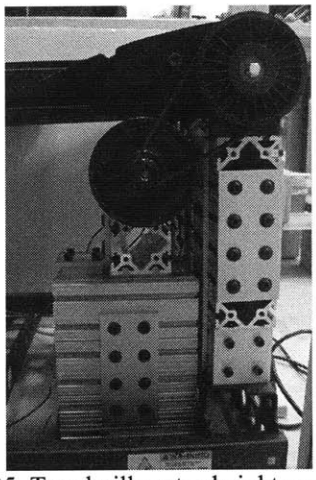

Figure 4-25. Treadmill motor height modification.

Further information about the selected motor gear reduction will be presented in Chapter 5 with the assembly troubleshooting information. The design and construction of the body weight support component of this device will now be presented.

4.6 Body Weight Support (BWS) Design

The body weight support system consists of two main parts: the supporting frame and the subject interface. The details of each subsystem are discussed below.

4.6.1 BWS Frame

The frame was constructed from 3 inch square 80/20 aluminum extrusion and connecting plates. Four swivel, lockable castors are mounted at the base so that the BWS is easy to maneuver when attaching to subject, but then can be locked to reduce relative motion between the treadmill and BWS. Figure 4-26 depicts the 80/20 extrusion and Figure 4-27 shows the BWS frame.

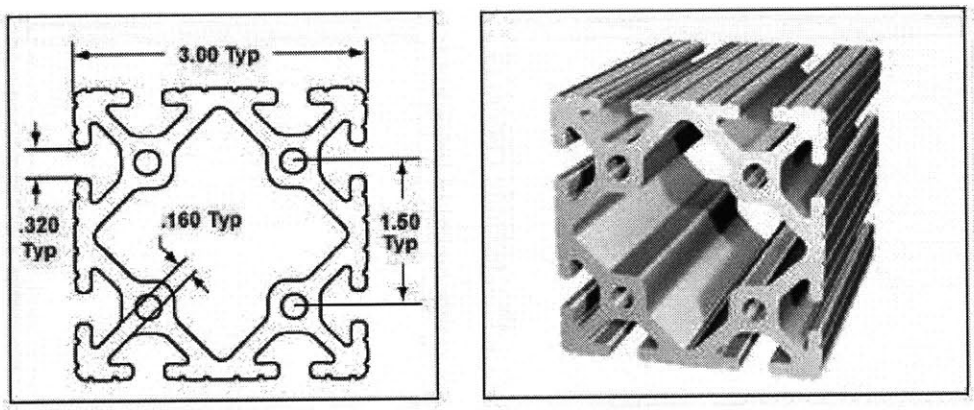

a) b)

Figure 4-26. 80/20, 3030 aluminum extrusion, a) front view and dimensions, b) isometric view [48].

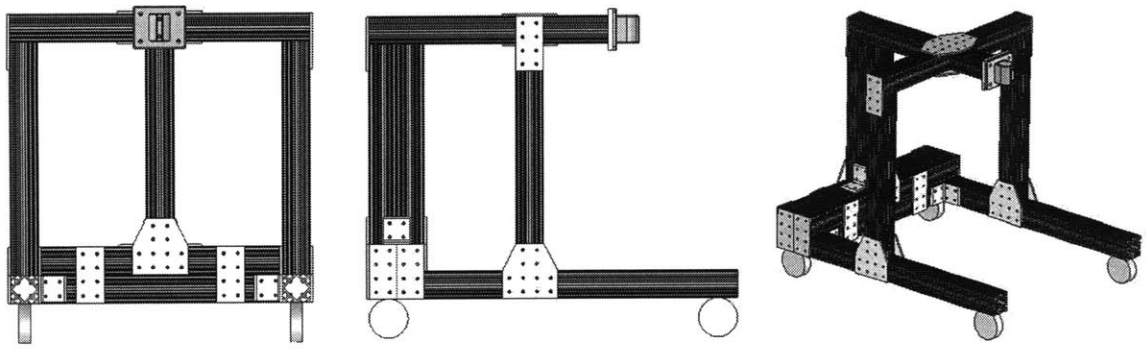

a) b) c)

Figure 4-27. BWS frame, a) front view, b) side view, c) isometric view.

80/20 extrusion is made of 6105-T5 aluminum and the profile chosen for the frame has the material and shape characteristics listed in Table 4-2. These values will be used to complete bending and column buckling calculations to validate the material selection. Calculations will be completed with a subject load, P, of 350 lbs (158.8 kg).

Second Moment of Inertia (in^4) [cm^4]	3.413 [142.1]
Cross-sectional Area (in^2) [cm^4]	3.448 [143.5]
Yield Strength (psi) [MPa]	35,000 [241.3]
Modulus of Elasticity (ksi) [GPa]	10,200 [70.3]

Table 4-2. 80/20 3030 extrusion material characteristics [48].

The three members that are under bending conditions are the 40 inch (101.6 cm) base members with the attached castors, the 26 inch (66 cm) member that is cantilevered and attaches to the BWS subject interface, and the 14.5 inch (36.8 cm) members that connect the vertical supports and the 26 inch member.

Figure 4-28 shows the location and the loading of the 40 inch member. This member is supported by casters on each end, and half of the subject load is transmitted through the vertical support 17 inches (43.2 cm) from the rear of the frame. The gear reducer sits at the front of the member and directly over one of the castors, so it does not cause bending. Since the loading is not in the center of the beam, the expression to calculate beam deflection is [44]:

$$v = \frac{-Pba}{6EIL}\left(L^2 - b^2 - a^2\right) \quad \text{(eq. 4-34)}$$

Where a is the distance from the origin to the load, b is the remaining distance to the end of the member, L is the total length of the member (a+b), E is the modulus of elasticity of the material, and I is the second moment of inertia. This member supports half of the subject's weight, so P = 175 lbs (79.4 kg). This results in a deflection of 0.006 inches (0.015 cm) which will not affect shaft alignment between the gear reducer and camshaft.

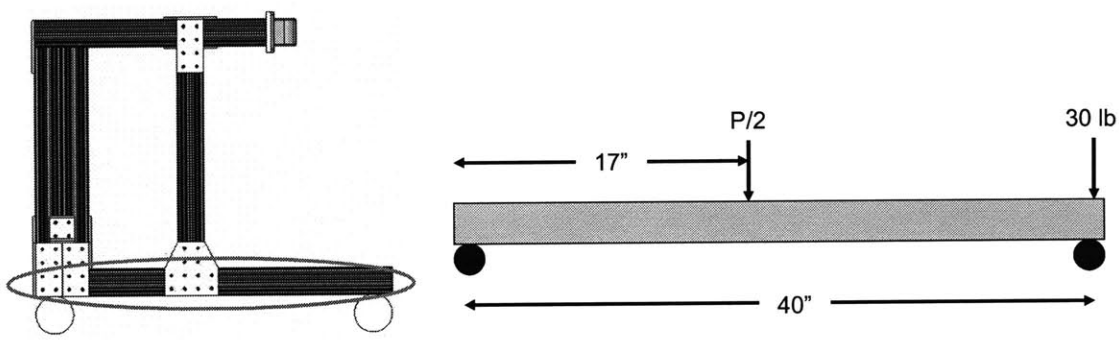

a) b)

Figure 4-28. BWS frame base member bending, a) location of beam in frame, b) force diagram.

The cantilevered member that supports the bicycle seat body weight support must not have a large deflection which will impede a normal gait (Figure 4-29). The deflection equation for this cantilever is [44]:

$$v = -\frac{PL^3}{3EI} \quad \text{(eq. 4-35)}$$

The resulting deflection if there were no side bracing and a 350 lb subject is 0.027 inches (0.069 cm). This small deflection is acceptable, but side bracing would also prevent side-to-side movements as well as add vertical support.

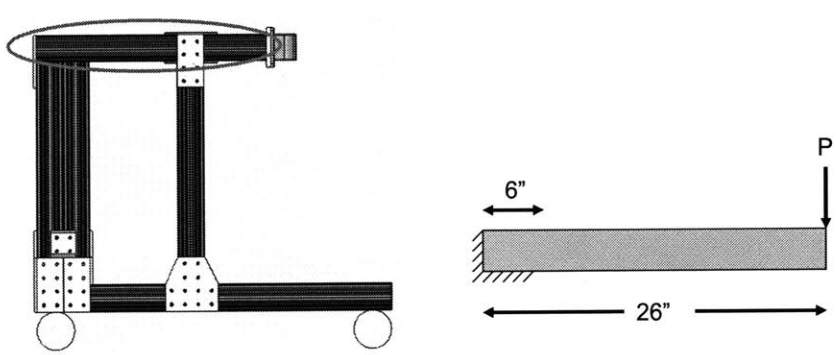

Figure 4-29. BWS subject interface attachment member bending, a) location of beam in frame, b) force diagram.

The 14.5 inch side braces (Figure 4-30), are also cantilevered, and with each carrying half of the load of a subject each, the resulting deflection is 0.0025 inches (0.006 cm), which is acceptable.

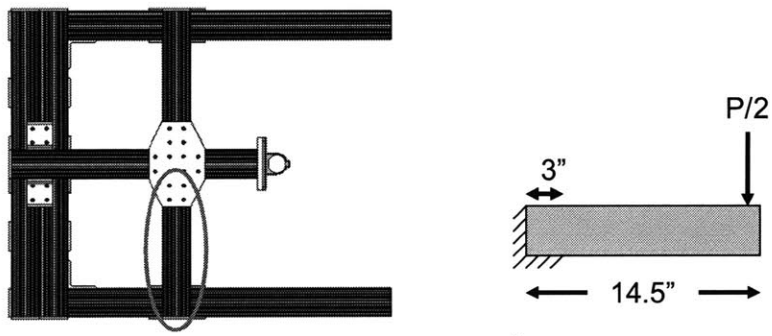

a) b)

Figure 4-30. BWS frame cross member bending, a) location of beam in frame, b) force diagram.

The frame also includes two 25 inch (63.5 cm) vertical side members that are under column loading and each member supports half of the subject (Figure 4-31). To calculate the critical load that would cause buckling [44]:

$$P_{cr} = \frac{\pi^2 EI}{L^2} \quad \text{(eq. 4-36)}$$

The critical load that would cause buckling is 549,787 lbs (249,379 kg), which is over 1500 times larger than the full weight of the subject, and is not a risk.

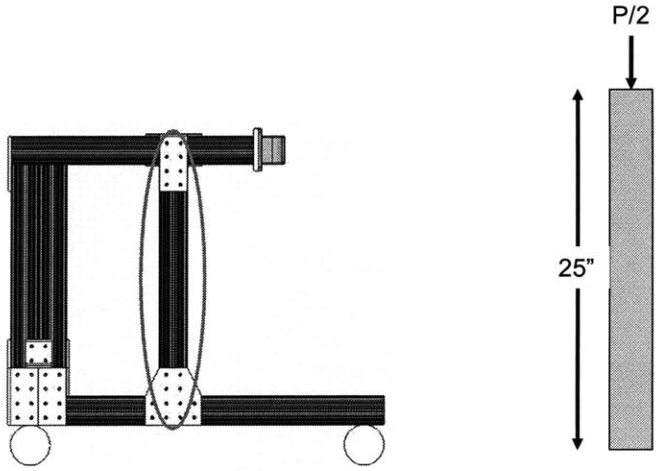

a) b)

Figure 4-31. BWS frame column buckling, a) location of beam in frame, b) force diagram.

The frame design is able to fully support the weight of a subject without unacceptable deflection. The BWS subject interface which is coupled to this frame will now be presented.

4.6.2 BWS Subject Interface

The BWS subject interface must allow degrees of freedom in order for the subject to be able to complete a natural gait. Vertical motion, pelvic rotation, and pelvic tilt will not be completely restricted for this prototype. In addition, both the height of the seat and upper body support must be adjustable to accommodate a range of patients. Each of these adjustment points has two 7/16 inch (1.11 cm) diameter 18-8 stainless steel quick release pins which have a maximum single shear load rating of 14,930 lbs (6772 kg). Each pin is in double shear, and even though one pin is more than strong enough for this application two were included as a safety measure. Figure 4-32 shows a model of the subject BWS interface and the harness that will be used to provide support to the upper body.

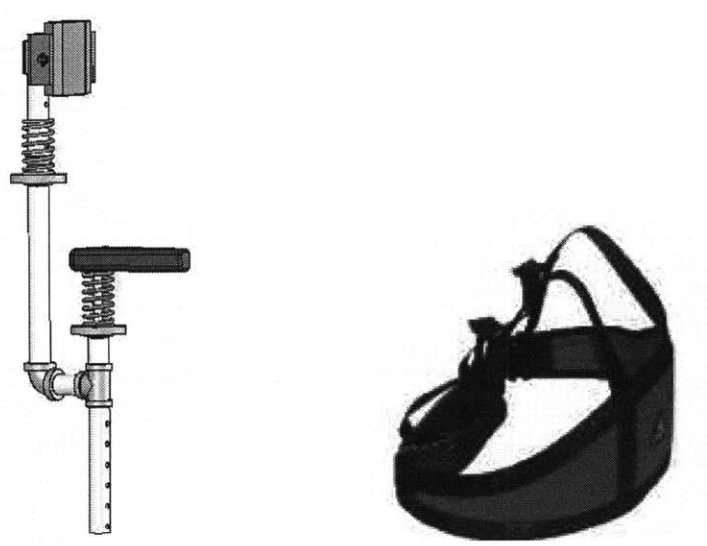

a) b)

Figure 4-32. a) body weight support subject interface, b) subject harness.

The BWS structure is made of Schedule 40, 1018 welded steel with a 1.90 inch (4.8 cm) outer diameter and 1.61 (4.1 cm) inch inner diameter. The link between the vertical back support and the bicycle seat support acts like a cantilever and the following bending and strength calculations

were completed in order to ensure the safety of the subject. Figure 4-33shows the loading condition.

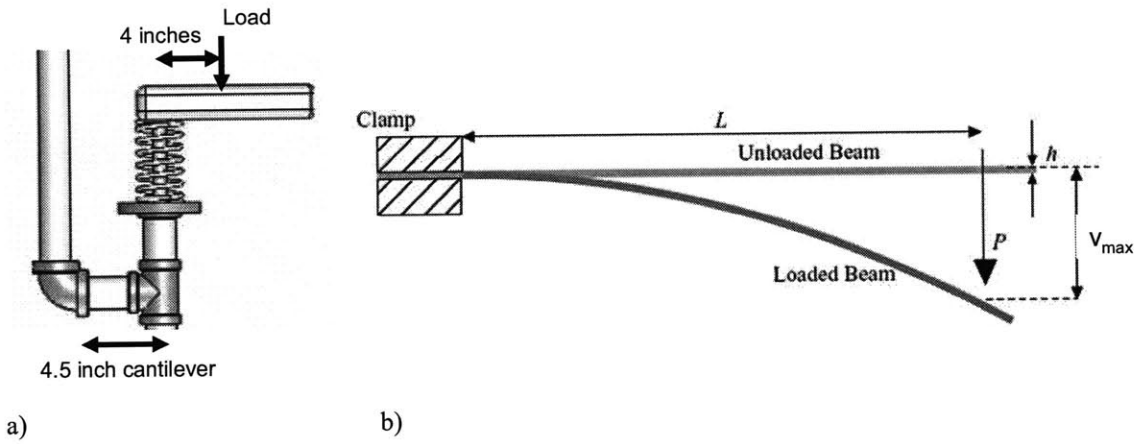

Figure 4-33. a) loading on bicycle seat, b) diagram of cantilever bending.

The following bending, second moment of inertia, I, and yield stress equations were used [44]:

$$v_{\max} = -\frac{PL^3}{3EI} \quad \text{(eq. 4-38)}$$

$$I = \frac{\pi\left(d_o^4 - d_i^4\right)}{64} \quad \text{(eq. 4-39)}$$

$$\sigma = \frac{P}{A} \quad \text{(eq. 4-40)}$$

Where v_{max} is the maximum deflection of the pipe, P is the load, L is the length of the pipe, E is the modulus of elasticity of 1018 steel (29,700 ksi or 205 GPa), d_o and d_i are the inner and outer diameters of the pipe respectively, and A is the pipe cross sectional area. For a 350 lb subject, and a factor of safety of 4 and a total cantilever length of 8.5 inches (21.6 cm), the maximum deflection is 0.031 inches (0.079 cm) and the stress is 1751.19 psi (12.1 MPa), over 30 times the 1018 yield stress of 53,700 psi (370.2 MPa). This design will not deflect significantly or yield. Steel was chosen because of cost, but aluminum could also be used which would make the design lighter and easier for therapists to adjust.

In order to allow for adjustability, the coupling between the frame and pipe of the body weight support could not be a press fit. This clearance allowed movement which could disrupt the balance of the subject and is unacceptable. To prevent this, and additional vertical member was

added to the BWS frame and a pipe collar was attached with a 3/8 inch (0.95 cm) threaded rod (Figure 4-34. This pipe collar can be loosened and retightened when the BWS is adjusted.

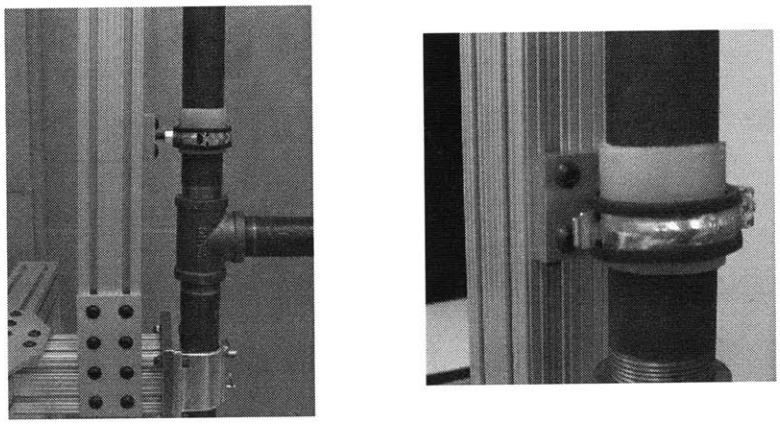

a) b)

Figure 4-34. Added BWS vertical stability, a) side view, b) detailed view.

Vertical Motion

Both the seat and the back support allow vertical movement of the subject's body and utilize springs and nested pipes with the ends lined with Teflon sleeves. This allows for a closer fit to reduce any wobbling between the parts, and reduces the sliding friction (Figures 4-35and 4-36.

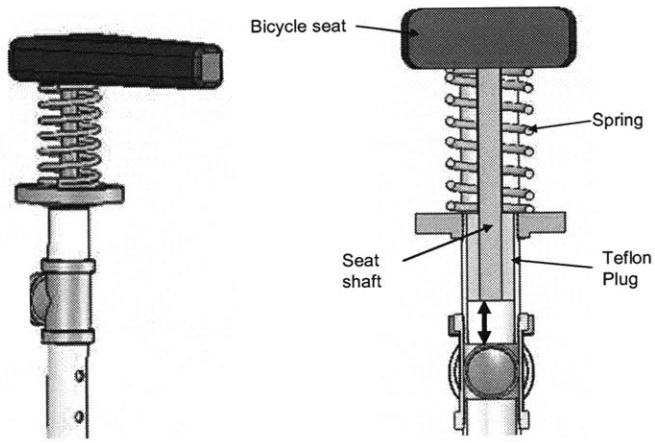

a) b)

Figure 4-35. Vertical DOF in bicycle seat, a) bicycle seat, b) cross-sectional view of nesting pipes.

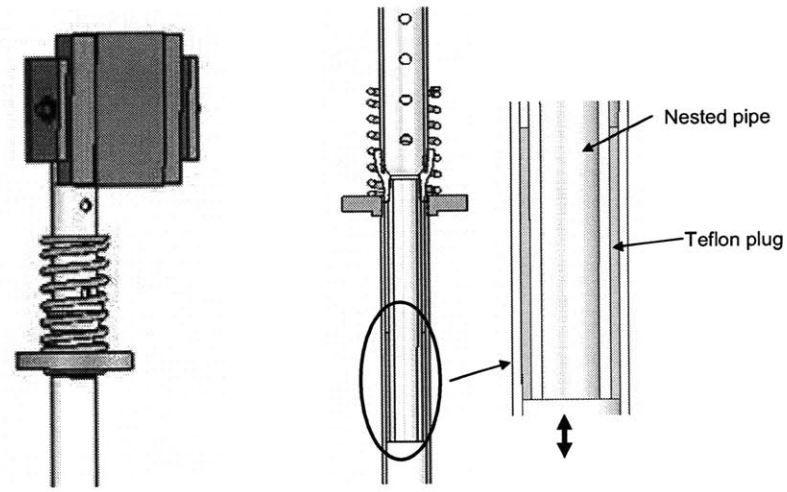

a) b)

Figure 4-36. Vertical DOF in upper body support, a) upper body support, b) cross-sectional view of nesting pipes.

The spring chosen for this prototype is a standard coil Hooke's Law spring. For the range of 99% male weighing 244 lbs (110.7 kg) to the 1% female weighing 93 lbs (42.2 kg), one spring may not be able to provide the nominal displacement. The average weight of 168.5 lbs (76.4 kg) was used with a displacement of 2 inches to calculate a spring constant of 84.25 lb/in (14.76 N/mm). Without having to special order a spring, the closest and easily available spring had a constant of 90 lb/in (15.7 N/mm). Under full body weight support, this would result in a 2.7 inch (6.9 cm) displacement for the 99% male and 1.03 inch (2.6 cm) displacement for the 1% female. This will be adequate for testing, but an adjustable spring would be required in order to provide adjustable body weight support for a range of subjects.

Pelvic Rotation

The nested design that allows the vertical motion of the pelvis and back also allows rotation (Figure 4-37) The current design does not have any stops to limit rotation, but these could easily be added and made adjustable depending on the subject's abilities. This degree of freedom is important to training a normal gait because along with pelvic tilt, it reduces the amount of energy needed by reducing the distance the center of mass must be lifted.

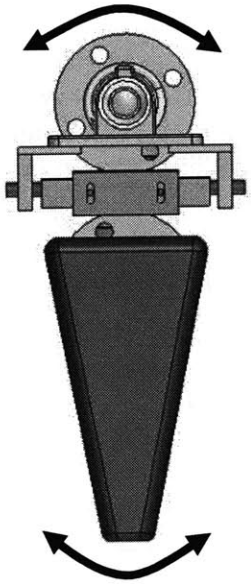

Figure 4-37. BWS pelvic rotation degree of freedom.

Pelvic Tilt

Preventing pelvic tilt will inhibit the subject from realistically practicing balance. While 5° is the average amount of required pelvic tilt, Figure 4-38 shows that the back support allows up to 20°. This will provide additional flexibility when securing the subject in the harness, and adjustable stops can be added to reduce this range of motion during therapy.

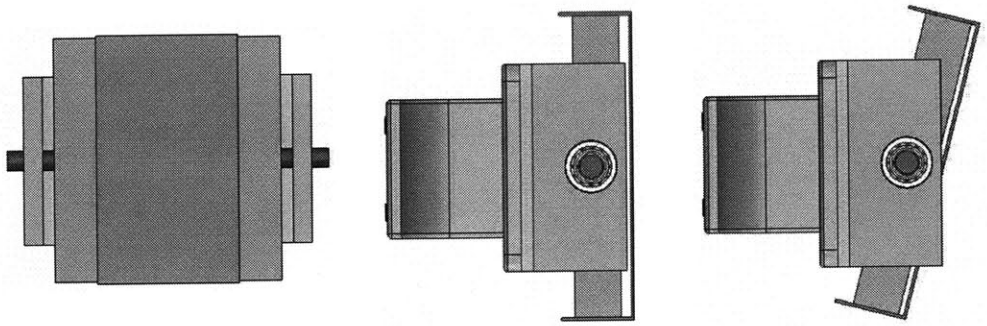

a) b) c)

Figure 4-38. Back support, a) front view, b) vertical back support, and c) back support at 20°.

The U-channel shaped sheet metal piece on the front of the back support is secured with four screws and can slide in and out in order to adjust the position of the upper body harness.

The detailed designs of both the treadmill and BWS systems have been presented separately. The next chapter will address troubleshooting the fully assembled system and healthy subject testing of the device.

Chapter 5: Device Troubleshooting and Healthy Subject Testing

This chapter presents the gear reduction implemented for the cam actuation, adjustments made to the device during final assembly, and the results from proof-of-concept testing with healthy subjects and a passive mannequin.

5.1 Motor Gear Reduction

To calculate the required gear reduction, the rated rpm of the motor is divided by the maximum desired camshaft speed. The brushless AC servomotors are rated at 3000 rpm, but the back electromotive force (back-emf) produced by the motor and controller amplifier must be considered to determine the maximum speed the system can produce. The back-emf is the voltage generated in an electric motor and is proportional to the angular velocity of the motor [49]:

$$V_b = K_e \omega \quad \text{(eq. 5.1)}$$

Where V_b is the back-emf, K_e is the constant of proportionality, and ω is the angular velocity of the motor shaft. For the Kollmorgen motors, the proportionality constant K_e = 111 volts/k_{rpm} and at the rated speed of 3000 rpm, the resulting back-emf is 333 volts. The controller amplifier has a limit of 50 volts, and therefore cannot produce a motor speed larger than 450 rpm. The maximum measured speed is approximately 350 rpm which produces a back-emf of 38.9 volts. This speed will be used to determine the appropriate gear reduction for the cam system.

The required cam speed range between 16 and 70 rpm was determined in Section 3.5.1. In order to choose a gear reduction that will operate in this range, the maximum motor speed is divided by the maximum cam speed. The quotient is 5, so a reduction of 5:1 should allow for the necessary range, but the torque of the motor is less than the rated 33.3 in-lb (3.76 Nm) at low speeds, and the motor does not turn until an angular velocity greater than 100 rpm (10.47 rad/sec) is commanded. In order to produce the torque required to lift the treadmill, it must be turning at its maximum speed of about 350 rpm with a gear reduction of 20:1. Figure 5-1 shows

an available 20:1 right angle, dual shaft reducer that will be used for this prototype. Full specifications are listed in Appendix A.

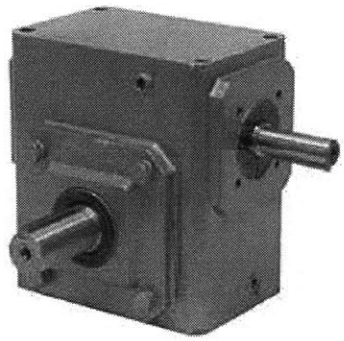

Figure 5-1. 20:1 ratio gear reducer.

This gear reduction produces a camshaft speed of 17.5 rpm. Based on the stride lengths of the 99% male and 1% female, at the slowest treadmill speed of 1.03 ft/sec (0.3 m/s), the required camshaft speed is approximately 16.2 and 21.9 rpm respectively. The resulting camshaft speed is only compatible with a small range of individuals in the tallest percentiles, and therefore the speed of the treadmill must be reduced. This will be discussed in the next section.

Figure 5-2 shows the gear reducer coupled to both the motor and the camshaft. The end of the camshaft was turned down to 0.875 inches (2.22 cm) and keyed to match the output shaft of the reducer. These shafts were coupled with a two-piece clamp collar with a keyway to prevent slipping. The motor shaft was unable to be modified, so a stepped clamp collar was used to couple the 0.75 inch (1.9 cm) diameter motor shaft to the 0.625 inch (1.6 cm) diameter input shaft of the gear reducer. The motor shaft could not be keyed, but since it is at the input which experiences less torque, slippage was not observed.

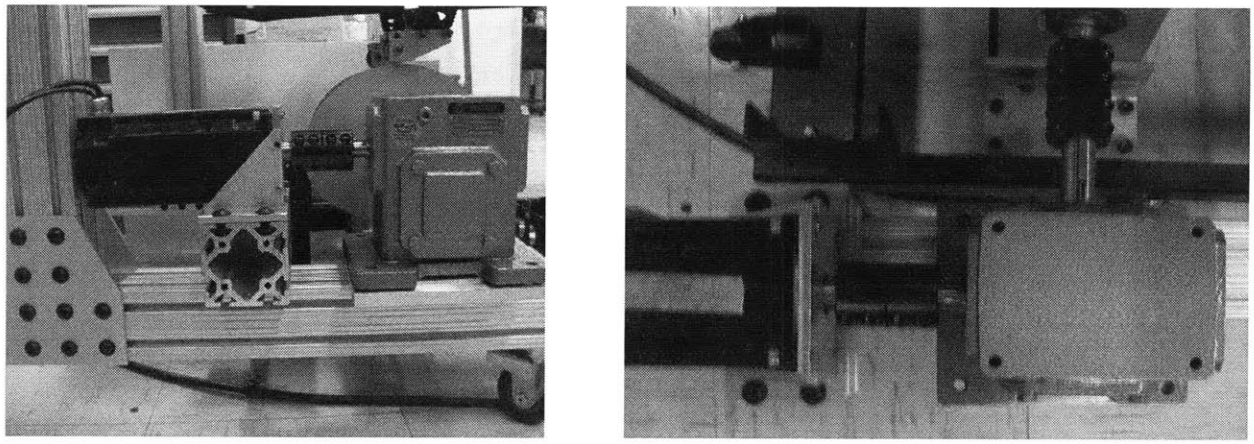

a) b)

Figure 5-2. Camshaft gear reduction, a) side view, b) top view.

5.2 Treadmill Speed Reduction

In order for the treadmill speed to be compatible with the available camshaft speed of 17.5 rpm, or 17.5 steps per minute, it must be reduced for the majority of the population. At this camshaft speed, a full stride must take about 3.4 seconds, which corresponds to a 2.04 second (60%) stance time. For the 1% female with a 20.24 inch stride length, the estimated required treadmill speed is 0.82 ft/sec (0.24 m/sec) and for the 99% male with a 27.44 inch stride length a 1.12 ft/sec (0.34 m/sec) speed which is approximately equal to the current slowest treadmill speed.

When the treadmill is commanded to 1.03 ft/sec, the 1.1 inch (2.8 cm) diameter treadmill motor output spins at 250 rpm and is coupled to a 4.7 inch (11.9 cm) diameter pulley for a speed reduction of about 4.3:1. In order to accommodate a treadmill speed of 0.82 ft/sec, a reduction of 1.03/0.82 or 1:1.26 is required. This results in about a 5 inch (12.7 cm) diameter pulley, but rounding up to a 6 inch (15.24 cm) diameter pulley will allow the treadmill to be run at slower speeds which may be utilized by patients.

In order to determine the belt length required to accommodate the new pulley, geometry was used based on the schematic in Figure 5-3. Setting the center of the motor output as the origin

and using Cartesian coordinates, the original treadmill pulley center is located at an x distance of 4.25 inches (10.8 cm) and a y distance of 5 inches (12.7 cm).

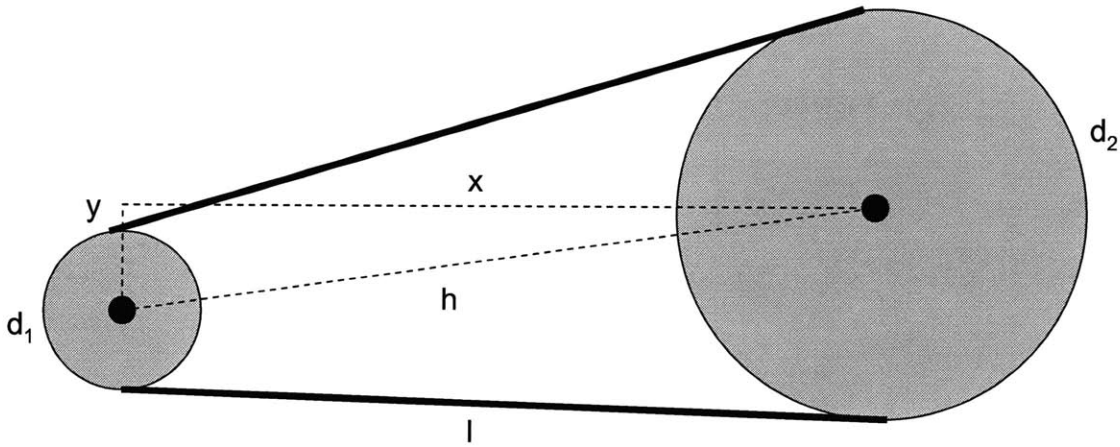

Figure 5-3. Schematic of pulley reduction and belt length.

The required belt length, assuming 180° of wrap on each pulley can be calculated using Equation 5.2. For the original pulley, the calculated L = 22.1 inches (56.1 cm) and the actual belt length was 22 inches, which checks.

$$L = \frac{1}{2}\left(2\pi\frac{d_1}{2}\right) + \frac{1}{2}\left(2\pi\frac{d_2}{2}\right) + 2l \quad \text{(eq. 5.2)}$$

Using the same equation to find the belt length for the new 6 inch diameter pulley and increasing the x distance account for the larger pulley results in a 25.49 inch (67.4 cm) or rounding up to the closest available standard size, 26 inches. The current configuration has about 4 inches of available adjustability in the negative x direction (away from the treadmill pulley), so this belt will be able to be accommodated.

Figure 5-4 shows the original and new pulley configurations. The 6 inch diameter pulley was able to reduce the treadmill speed from 1.12 ft/sec (0.34 m/s) to 0.92 ft/sec (0.28 m/s). The TreadClimber uses closed-loop control with a sensor that measures the time to complete one revolution by detecting a magnet that is located on the pulley. Attempts to move both the magnet

and sensor towards the center of the pulley so that the controller would slow the motor resulted in a system error. Also, two magnets were placed at 180° on the pulley in order to "trick" the system in to rotating at half the original speed, but this also resulted in a system error.

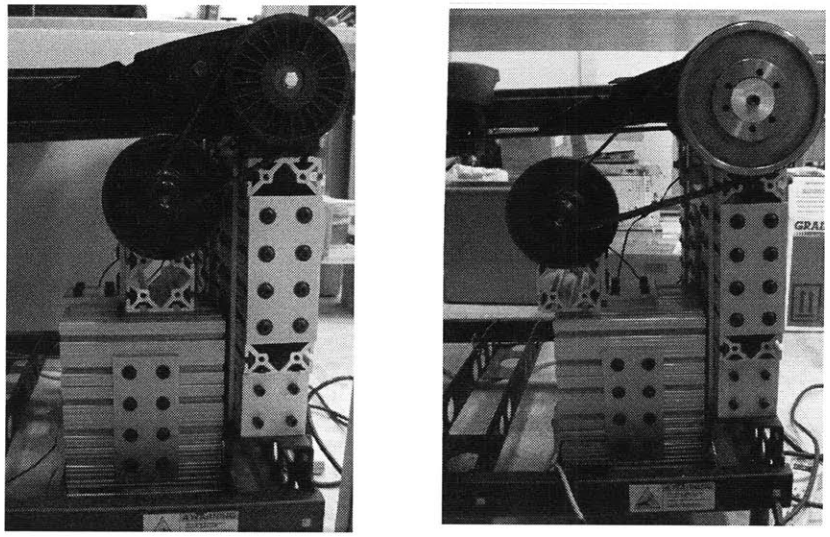

a) b)

Figure 5-4. Treadmill pulley, a) original 4.3:1 reduction, b) modified 6:1 reduction

This troubleshooting was able to reduce the treadmill speed, but an optimal solution would be to purchase motors to drive the cams that have a lower back-emf so that the cam speed can be adjusted to the required treadmill speed.

5.3 Fully Assembled System

Figures 5-5 and 5-6 show the full system as a Solidworks model and as built, respectively. This configuration was used in both the healthy human subject and passive mannequin testing which will be presented next.

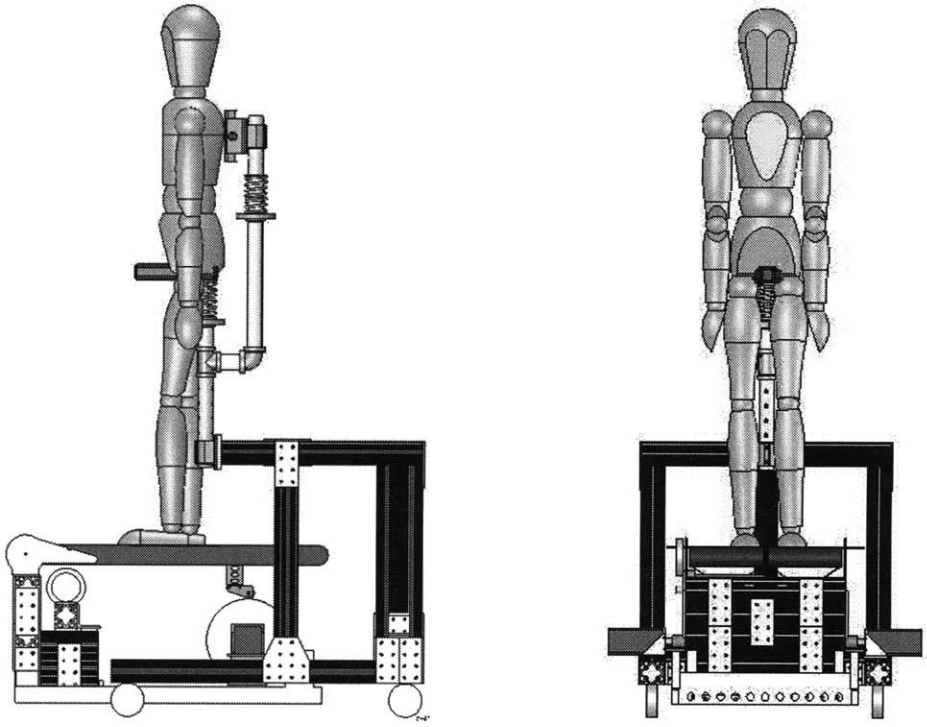

a) b)

Figure 5-5. Model of full system. a) side view, b) front view

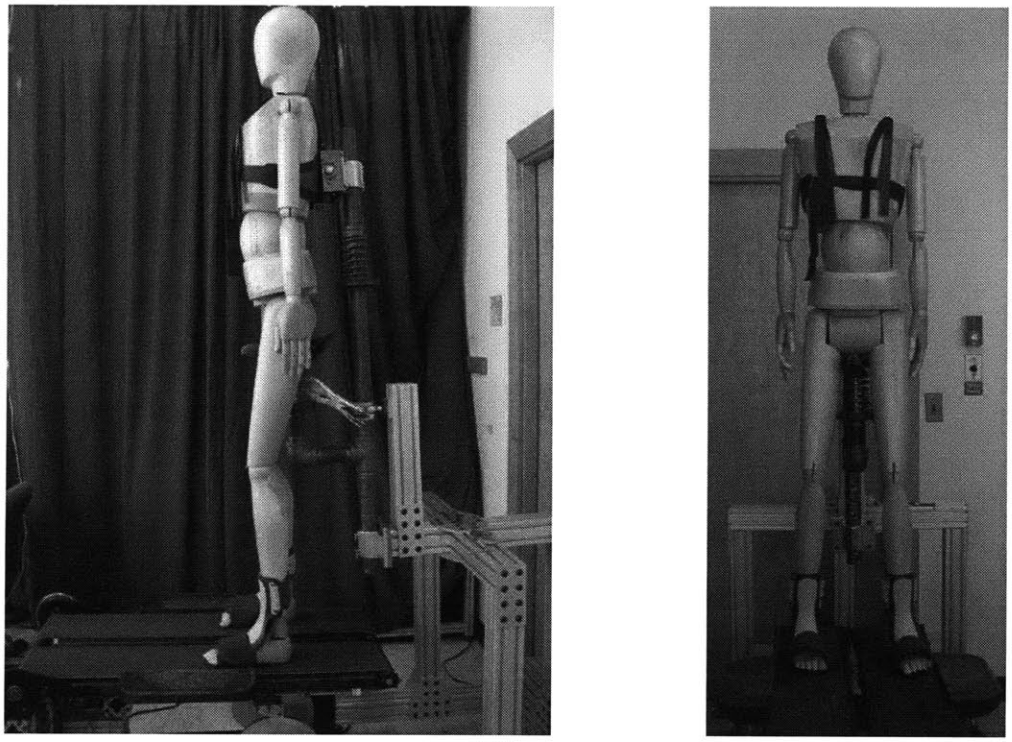

a) b)

Figure 5-6. Fully assembled system, a) front view, b) side view.

5.4 Healthy Subject Testing

In order to test if this prototype was able to provide adequate swing clearance, a small group of healthy subjects were tested walking on the device both as a regular treadmill (no actuation or BWS) and with BWS and the motors driving the cams. Electromyography from leg muscles was collected to measure the muscle activation. This testing was approved by the MIT Committee on the Use of Humans as Experimental Subjects (COUHES) and all subjects gave informed consent.

5.4.1 Electromyography

The study of the electrical signals measured when a muscle is contracted is called electromyography (EMG). Like axons in the nervous system, muscles also conduct electrical potentials and the signal resulting from the motor fibers that fire is called the motor unit action potential (m.u.a.p.) [50]. When electrodes are placed on the skin over a muscle (surface), or implanted inside the muscle (in-dwelling), they will record the sum of the m.u.a.p. along that muscle. Distance from the electrode is also a factor and as the m.u.a.p.'s distance from the electrode increases, the magnitude of its measured signal decreases [50]. For the healthy human subjects, surface EMG will be recorded during normal (non-actuated) treadmill walking and when the subject is relaxing their legs with an ankle brace and allowing the treadmill to provide the necessary swing clearance. The following muscles have been chosen to record EMG signals.

Tibialis Anterior

The tibialis anterior (TA) is located on the front of the lower part of the leg, anterior, or in front of the tibia (Figure 5-7). For healthy subjects, this muscle exhibits peak EMG activity at heel-strike when the foot is dorsiflexed, and no activity during midstance and toe-off [51]. There are two main theories for the function of this muscle. Some studies argue that the TA counteracts forces applied to the heel by the ground during heel-strike, and others suggest that it is responsible for decelerating the foot at heel-strike and lowers it to the ground by lengthening [51]. When this muscle is paralyzed, the subject can not hold their foot up and exhibits a clinical condition referred to as "drop foot".

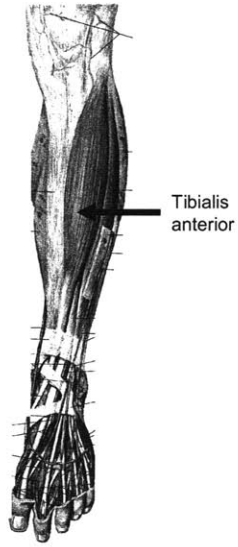

Figure 5-7. Tibialis anterior [52].

Soleus

The soleus is located on the lower leg and is activated during foot plantar flexion [51] (Figure 5-8). McGowan et al. found that while both the soleus and gastrocnemius contribute to body support, the soleus is the primary contributor to forward propulsion [53].

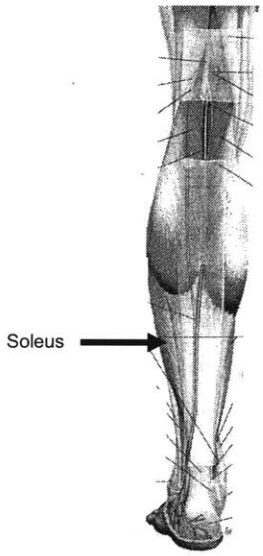

Figure 5-8. Soleus [52].

Rectus Femoris

The rectus femoris is one of four muscles that make up the quadriceps femoris (Latin meaning four muscles of the femur) which is also comprised of the vastus lateralis, vastus medialis, and vastus intermedius [52]. Figure 5-9 shows the front of the thigh and identifies the location of the rectus femoris. The rectus femoris is close to the surface and covers most of the other three quadriceps muscles which makes it the easiest to measure using surface EMG electrodes. Its highest activation occurs at heel strike and it exhibits a biphasic pattern, meaning it has activation peaks during one gait cycle [51].

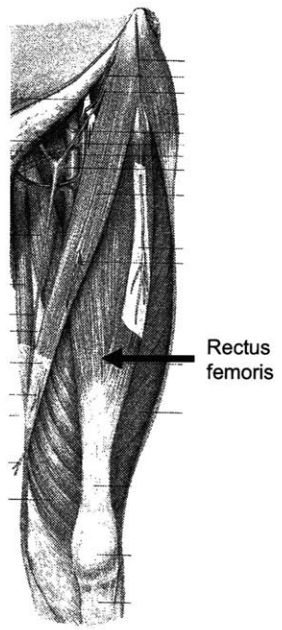

Figure 5-9. Rectus femoris [52].

Semitendinosus

The hamstrings are made up of three muscles, the semitendinosus, semimembranosus, and the biceps femoris [52]. Figure 5-10 shows the back of the thigh and identifies the location of the semitendinosus. This muscle is located on the back of the leg above the knee and is activated during stance phase and exhibits a triphasic pattern with three peaks. The first peak occurs at heel-strike, the second at 50% of the cycle, and the third at about 90% of the cycle [51].

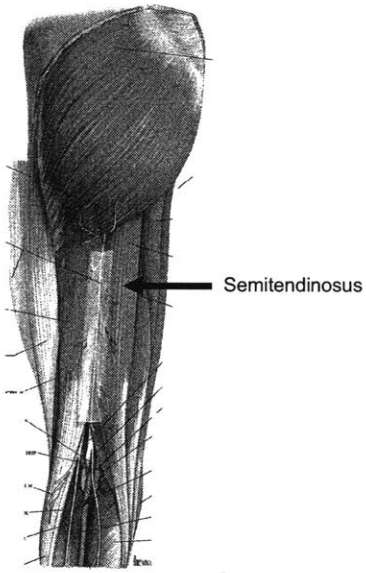

Figure 5-10. Semitendinosus [52].

5.4.2 Healthy Subject Test Results

The EMG signals were collected from the muscles listed above by a 16 channel Myomonitor IV wireless datalogger from Delsys (Boston, MA) (specifications listed in Appendix A). Figure 5-11 shows the EMG placement on a subject prior to testing. Where 1 indicates the TA, 2 the soleus, 3 the rectus femoris, and 4 the semitendinosus.

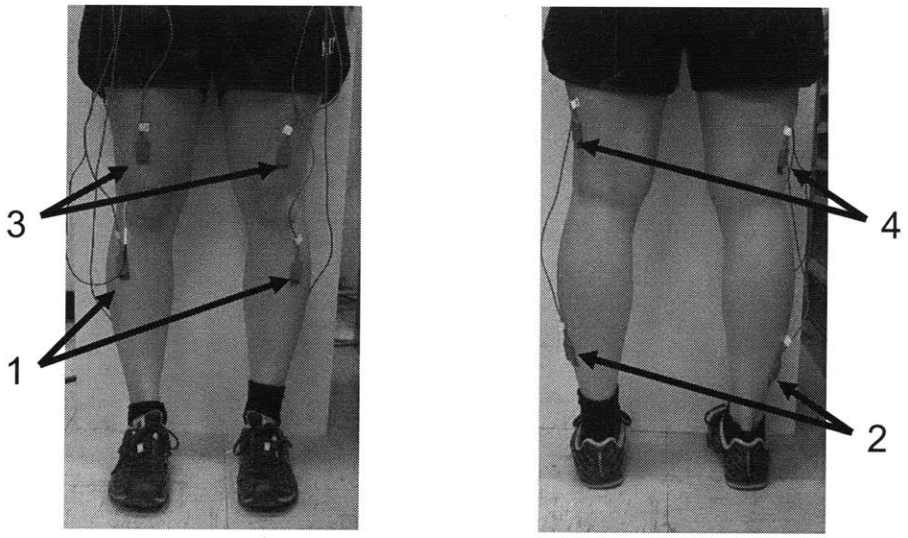

Figure 5-11. Subject EMG placement.

Figure 5-12 shows a summary of EMG activity in the leg during normal walking for a full gait cycle beginning with heel-strike and Figure 5-13 shows EMG data from the quadriceps, TA, gastrocnemius, and hamstrings of a healthy subject walking at about 3.3 ft/sec (1 m/s) [51]. Details of which quadriceps and hamstring muscles measured were not indicated.

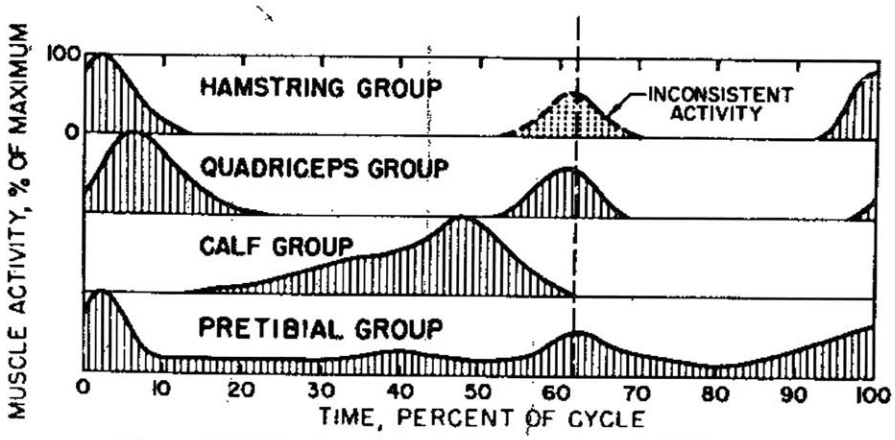

Figure 5-12. Muscle activity during one gait cycle [51].

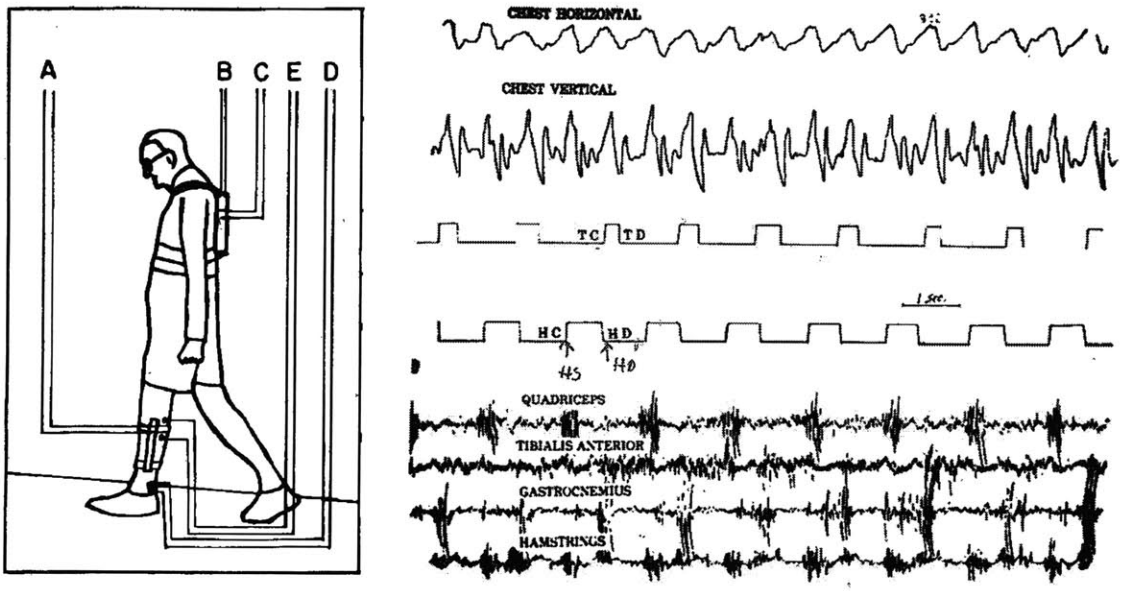

Figure 5-13. Average healthy subject walking EMG data [51].

Four healthy subjects were tested, but due to the set camshaft speed of 17.5 rpm and minimum treadmill speed of 0.92 ft/sec (0.28 m/s), only two subjects were able to consistently synchronize their stepping with the actuation of the treadmill. This issue can be corrected in future

configurations by implementing different camshaft motors that will not be limited by the amplifier.

The EMG data was processed with Matlab using a moving 250 ms integral window and used the trapezoidal rule to estimate the amplitude of the signal. The root mean square of the signal was calculated before the estimation. The original Matlab program was written by Patrick Ho.

Figure 5-14 shows the both the raw (thin trace) and estimated amplitude (positive thick trace) of the EMG signal from the TA during normal treadmill walking. As expected, the peak activation occurs at heel-strike and there is no activation during the swing phase.

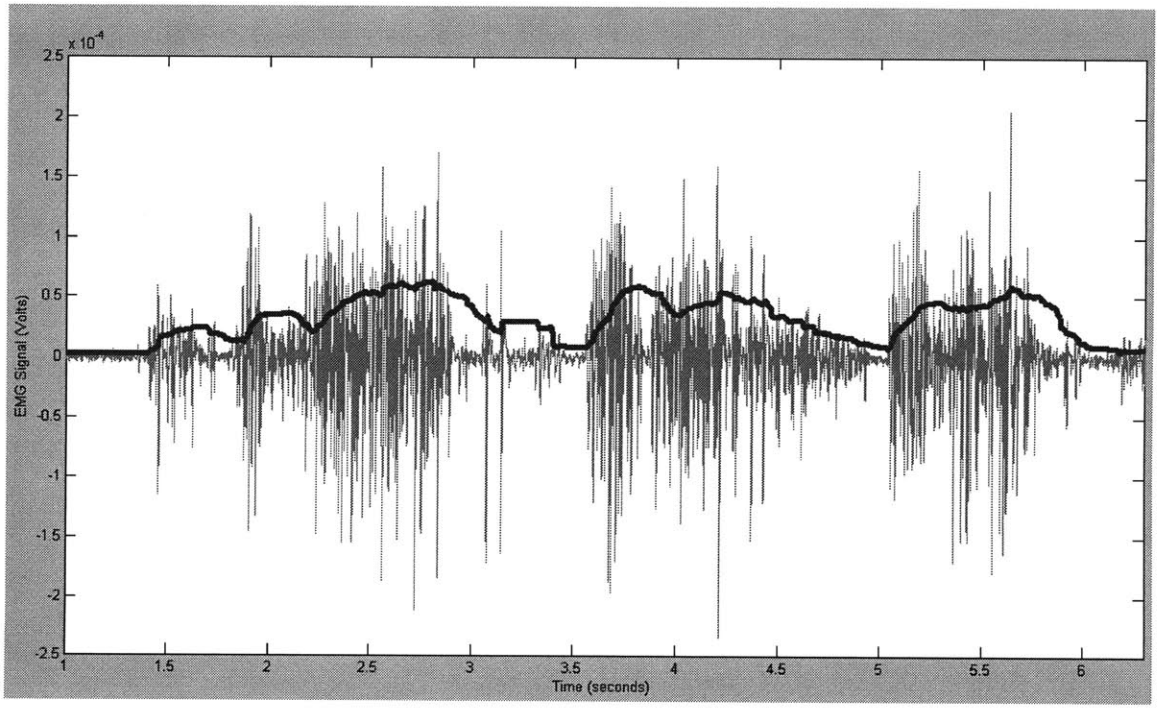

Figure 5-14. Healthy subject normal treadmill walking TA EMG.

Figures 5-15 – 5-17 show the remaining EMG signals of the soleus, rectus femoris, and semitendinosus, respectively.

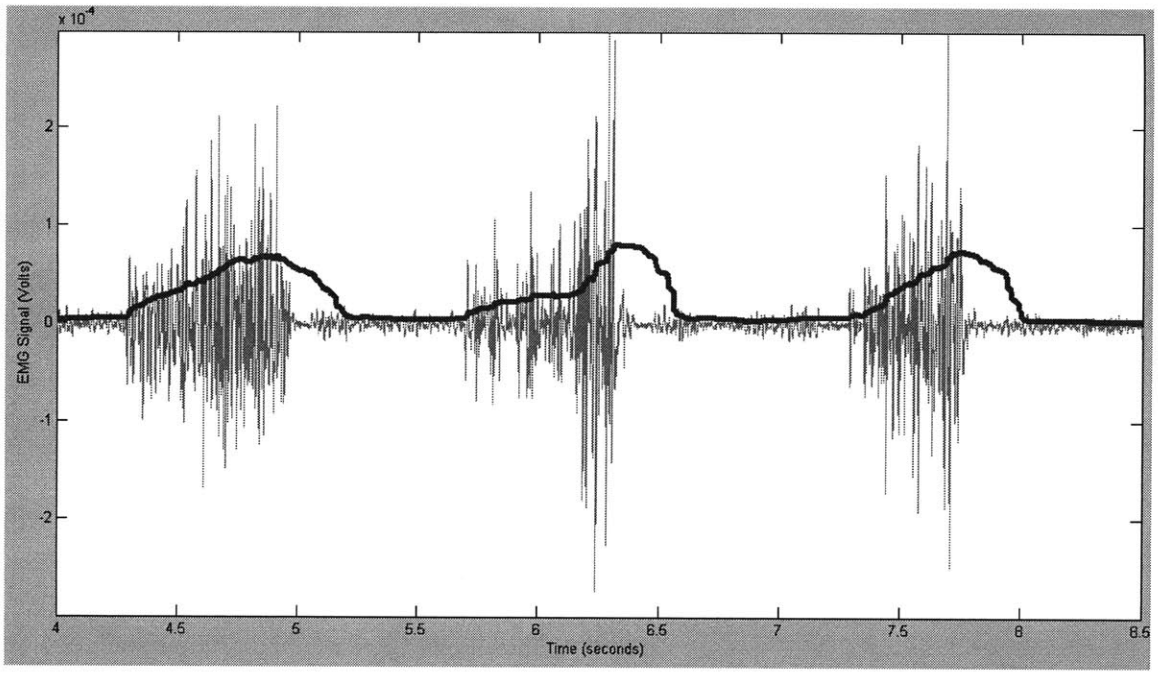

Figure 5-15. Healthy subject normal treadmill walking soleus EMG.

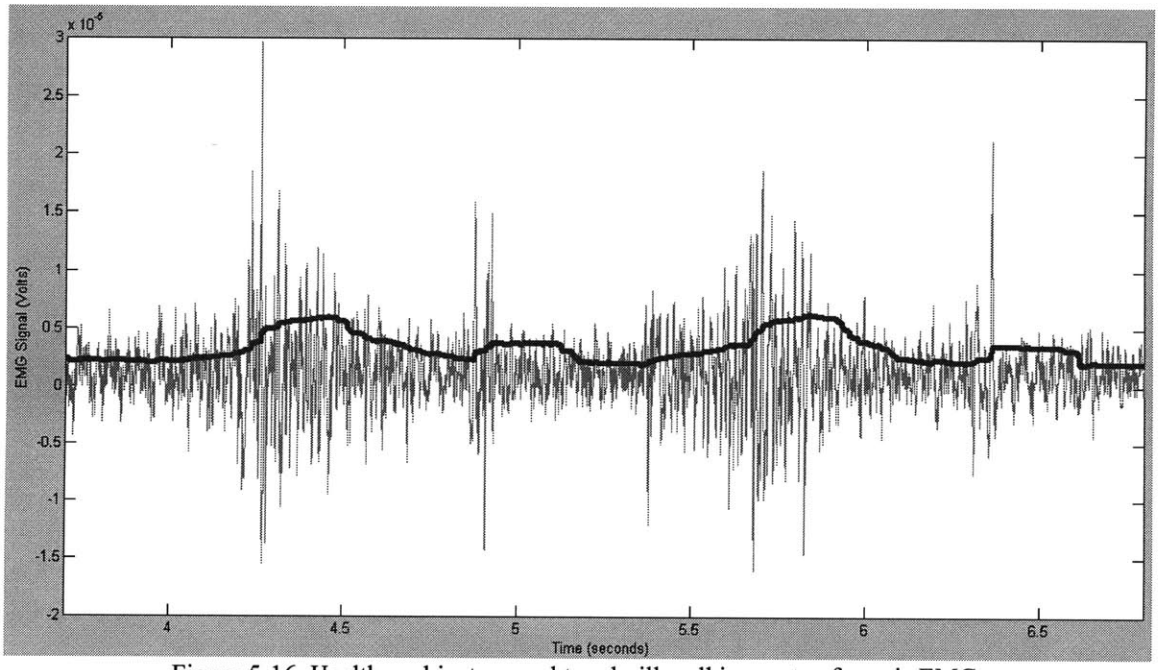

Figure 5-16. Healthy subject normal treadmill walking rectus femoris EMG.

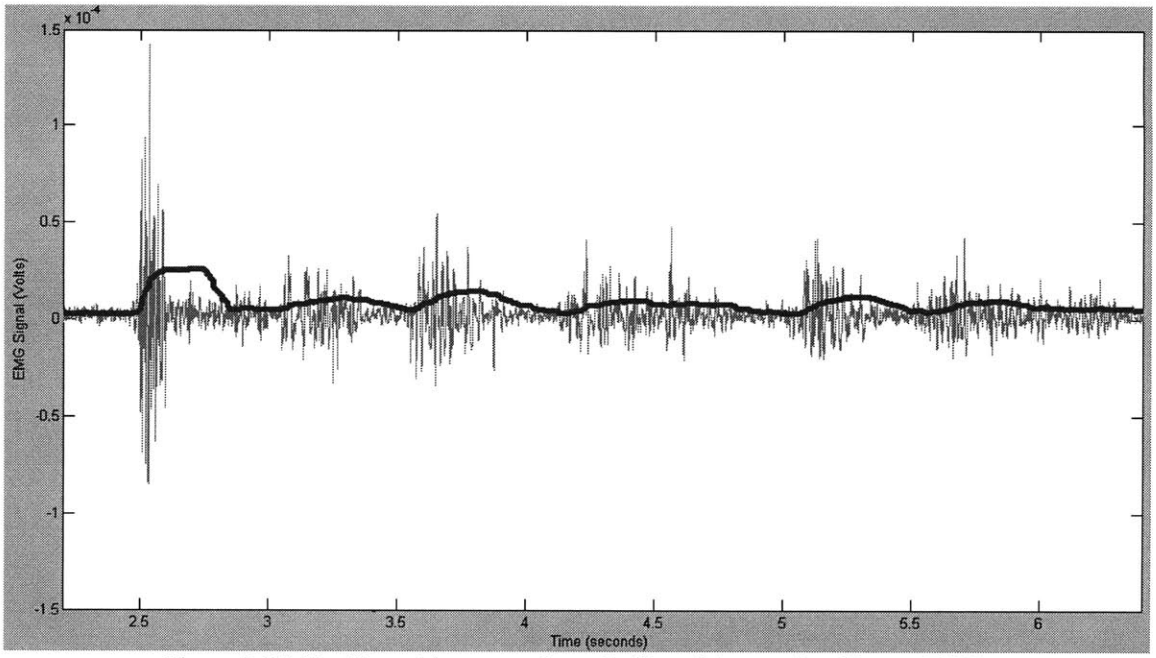

Figure 5-17. Healthy subject normal treadmill walking semitendinosus EMG.

As expected for normal healthy gait, the soleus was activated at toe-off to provide propulsion, the rectus femoris shows a biphasic pattern and the semitendinosus a triphasic pattern.

The above figures and their characteristics will serve as a baseline to compare the EMG activity during treadmill actuation with BWS. An ankle brace was secured to the subjects so that they could relax their leg without experiencing foot drop and allow their leg to swing freely.

Figure 5-18 shows the EMG signal from the TA which is very similar to normal treadmill walking. Peak activation was observed at heel-strike and activation was present throughout the stance phase.

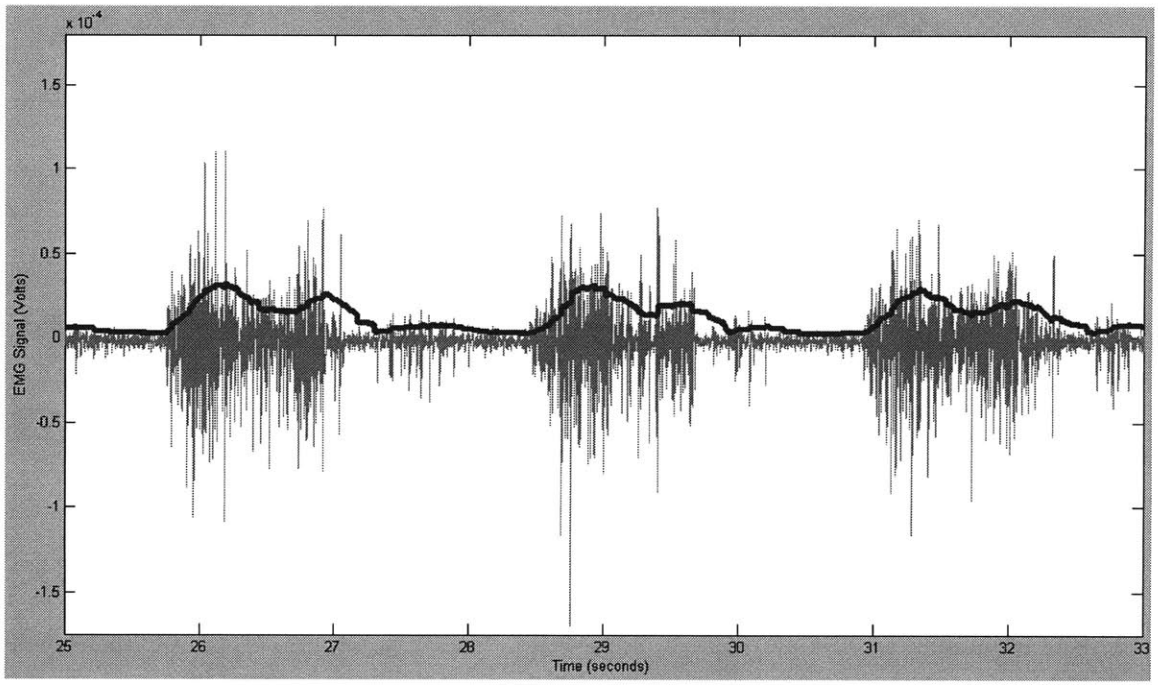

Figure 5-18. Healthy subject actuated treadmill walking TA EMG.

Figures 5-19 (soleus) and 5-20 (rectus femoris) show both free swing for three cycles when the subject was synchronized with the actuation followed by three cycles where the gait cycle and cam were not coordinated and the subject was actively stepping. The soleus and rectus femoris showed almost no activity during free swing, but when the subject and the actuation were not coordinated, the EMG signal resembled normal treadmill walking. Since the soleus is responsible for forward propulsion, it is logical that its activity is greatly decreased when gravity and the treadmill actuation are facilitating the swing phase.

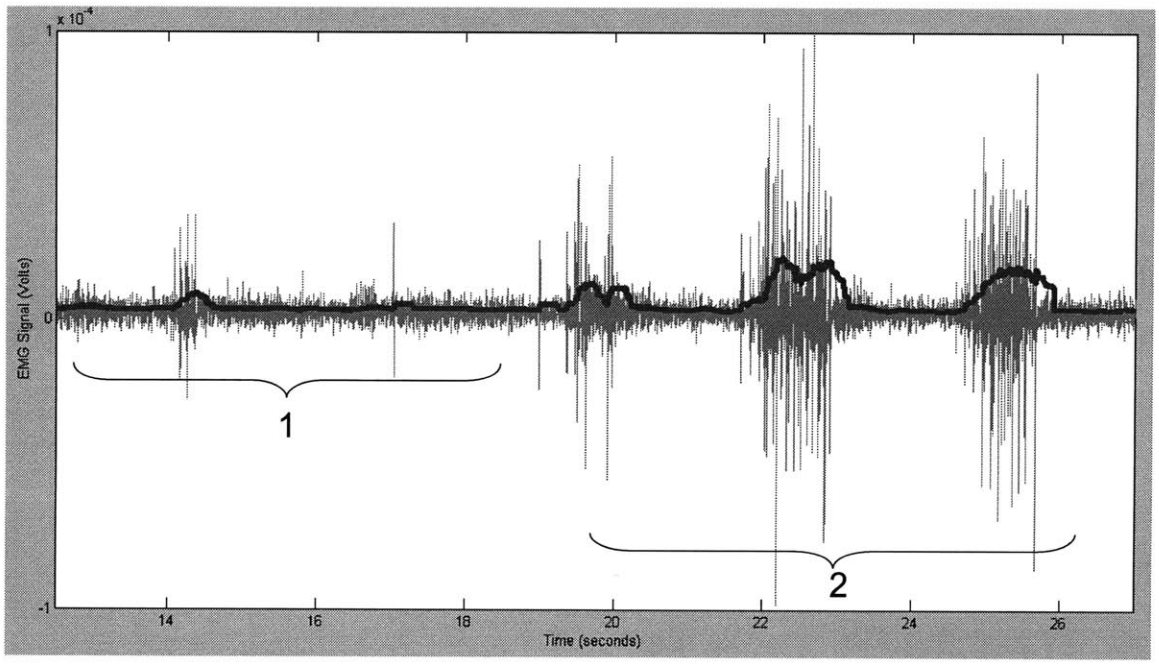

Figure 5-19. Healthy subject actuated treadmill soleus EMG.

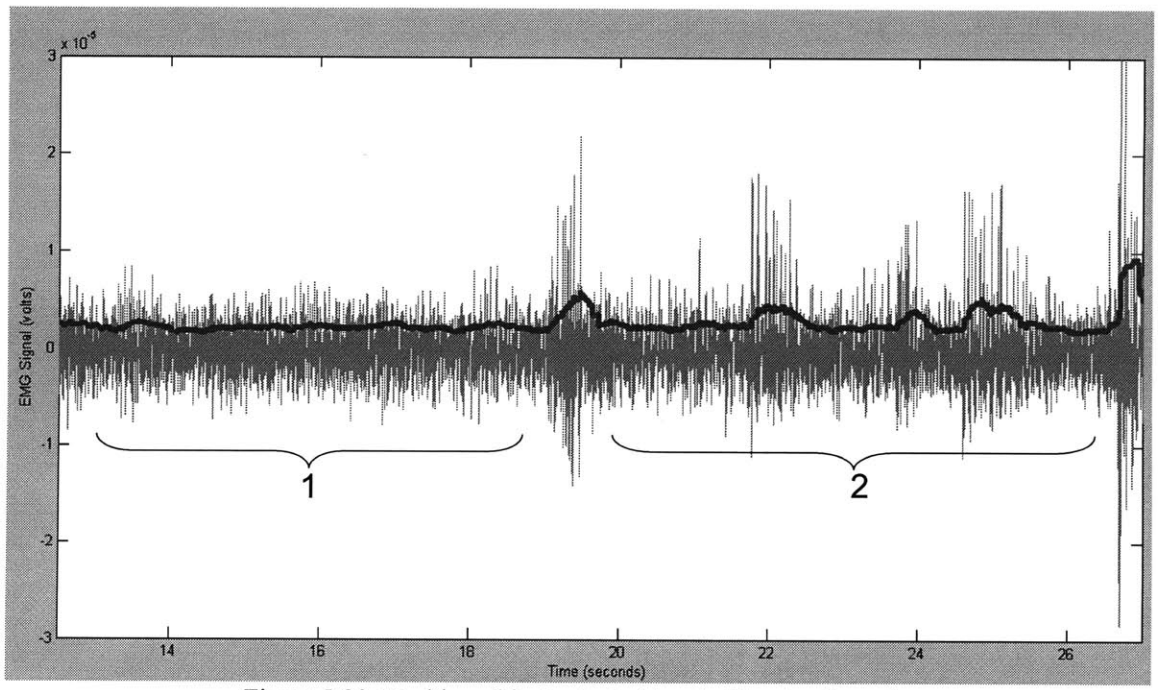

Figure 5-20. Healthy subject actuated treadmill rectus femoris.

Figure 5-21 shows the EMG signal measured from the semitendinosus, which like the TA, looks very similar to the normal treadmill walking with a triphasic pattern. Since the semitendinosus is

activated during weight bearing, even though BWS is provided, the leg will still experience loading and will generate an EMG signal.

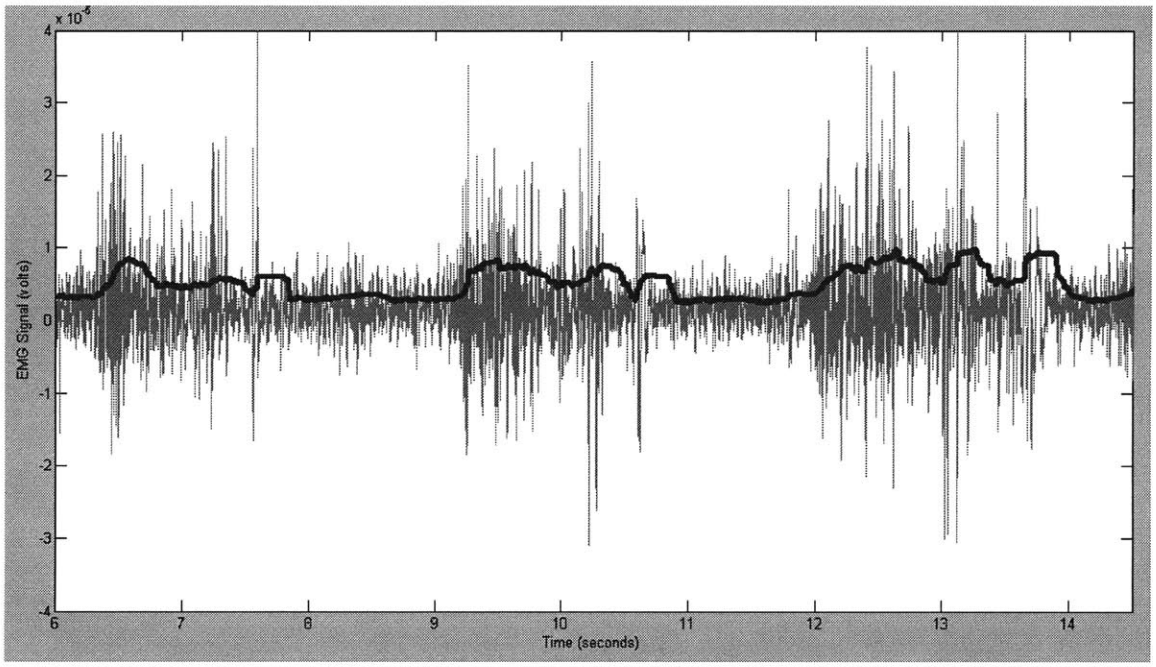

Figure 5-21. Healthy subject actuated treadmill walking semitendinosus EMG.

These preliminary EMG measurements show that even during free swing, the TA and the semitendinosus are activated, while the soleus and rectus femoris are not. If this therapy is used, it may be necessary to include additional exercises that will help strengthen the soleus and rectus femoris so that the patient will be able to reduce the amount of swing clearance needed to walk. Further testing will be required to determine if this therapy will be effective, but testing with healthy subjects has shown that this device is feasible.

5.4.3 Mannequin Testing

Another test to evaluate the feasibility of this device was to use a passive mannequin. Nicknamed Pinocchio, he is made of wood, 5'10" (177.8 cm) tall, weighs approximately 20 lbs (9.1 kg), and is shown with the device in Figure 5-6. Although the treadmill and cam speeds could not be optimally adjusted for his height, the treadmill actuation was able to provide adequate clearance for the swing phase (Figure 5-22).

a) b) c)

Figure 5-22. Mannequin test, a) at toe-off, b) swing phase, c) heel-strike.

By showing that this device can be used in a completely passive state indicates that the patient does not need to have full control of their legs before they can begin using this device for gait therapy.

Goniometers were used with the same data logging system (Figure 5-23). Measurements were recorded at the hip and knee during treadmill actuation (Figures 5-24 and 5-25).

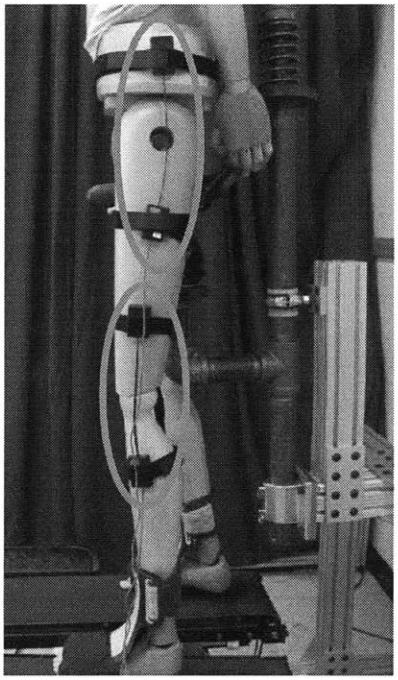

Figure 5-23. Mannequin goniometer placement.

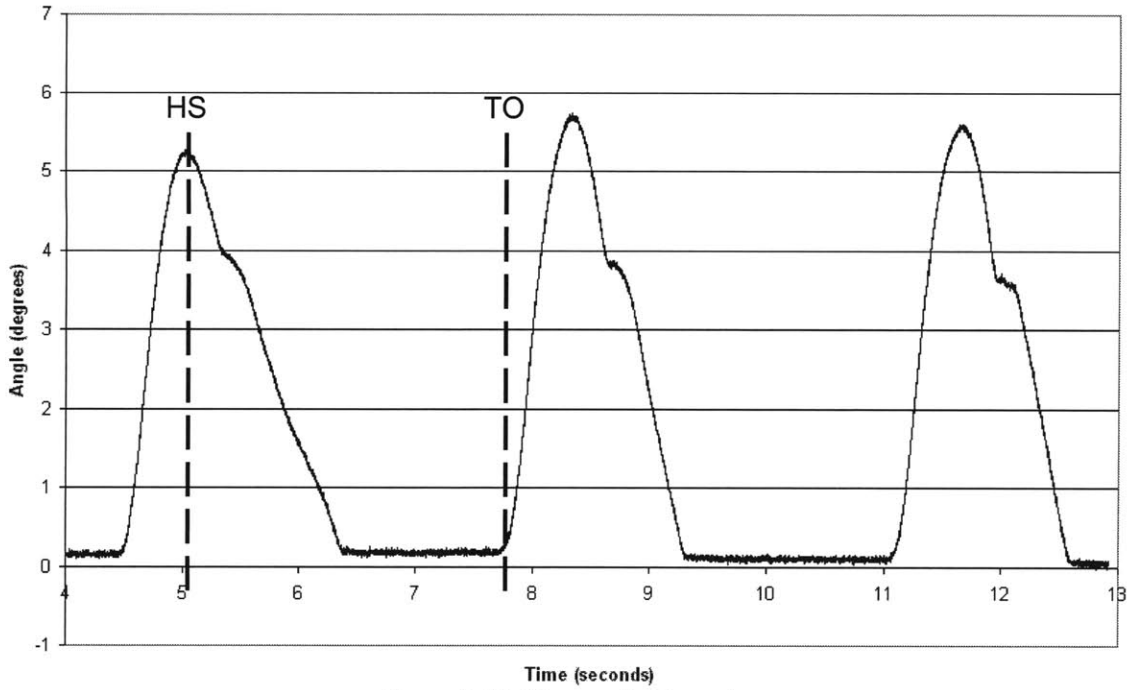

Figure 5-24. Mannequin hip angle.

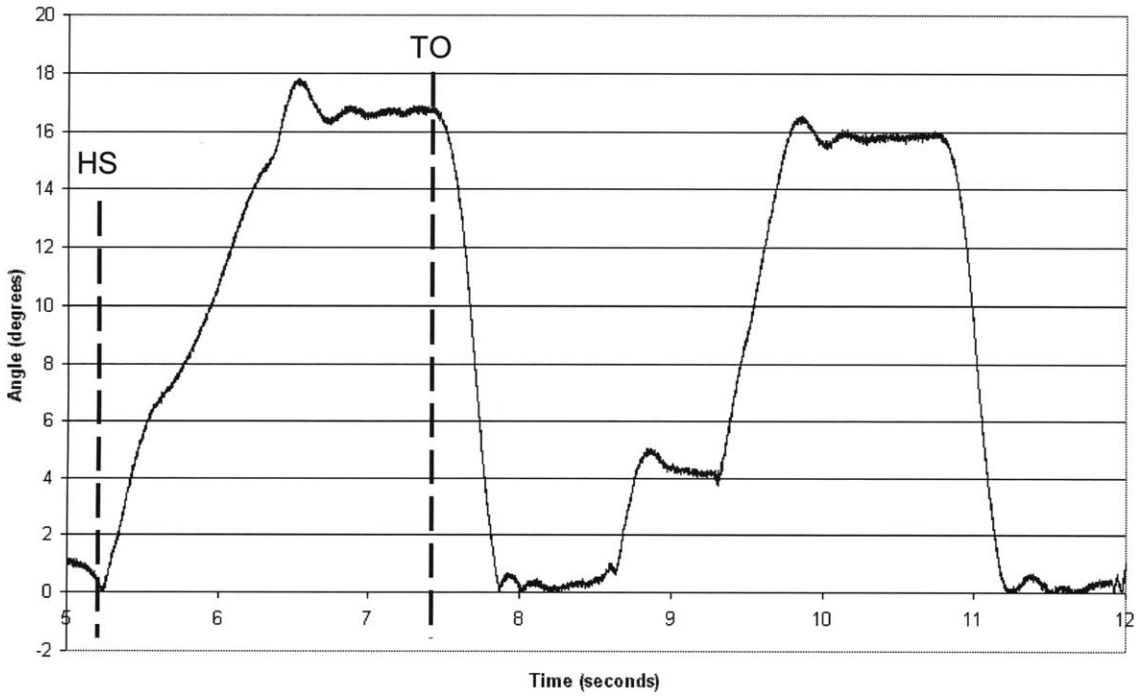

Figure 5-25. Mannequin knee angle.

During average healthy gait at about 3.28 ft/sec (1 m/s), hip angles are 30° and -10° at heel-strike and toe-off respectively (refer to Figure 3-5) [5]. For the mannequin, the observed angle at heel-

strike was 5° and at toe-off 0°. This range of movement is much smaller than healthy gait, but the hip and knee angles do depend on speed and the treadmill was only running at about 1 ft/sec (0.3 m/s) or about one third of the speed for average healthy gait. For the knee during average healthy gait the angle ranges from about 5° to almost 60° when the knee flexes to provide swing clearance. When the treadmill provides swing clearance, the knee does not have to flex and after toe-off the knee angle goes to zero before the next heel strike which was expected. While the angles are smaller than normal gait, the subject is still receiving neural input provided by stepping and as the therapy speed increases and the provided swing clearance decreases, the angles should increase.

The next and final chapter will discuss the project evaluation and recommend areas for future work so that this device can be used by patients in a clinical setting.

Chapter 6: Conclusions

This thesis presented the design, development, troubleshooting, and basic testing with healthy subjects of a device for gait rehabilitation. Through the introduction and background, the current problems clinicians and patients are facing were discussed and a need for this device was explained. By looking at the strengths and weaknesses of devices currently available, the novel idea of actuating the walking surface rather than the patient was developed. Several actuator designs were discussed and the final chosen cam design was described in detail. Finally, the components for both the cam actuation and BWS were machined in house by the author and the device was assembled and successfully tested with healthy subjects and a passive mannequin to show feasibility of this proof-of-concept prototype. This final chapter will discuss an overall evaluation of the project and suggest areas for future work.

6.1 Project Evaluation

The purpose of this project was to complete a proof-of-concept design for a novel device for gait therapy. The resulting prototype was able to provide swing clearance for healthy subjects and a completely passive mannequin. This device successfully showed that this concept is feasible, and the next section will address areas that will improve the design so that it can be further developed and tested in a clinic with patients.

6.2 Future Work

The following is a suggested list of future work to be completed for this device to be implemented in the clinic and additional features that would enhance this design:

- Patient Accessibility – The current treadmill surface is approximately 20 inches (50.8 cm) from the floor, and impaired patients will need a ramp with assistance to use this

device. If linear actuators were employed for actuation, the amount of clearance required under the treadmills could be greatly reduced and this problem could be eliminated.

- Treadmill/Cam Control – The current control for the treadmill and cam speed is limited by the TreadClimber default settings and the cam motor amplifier. For this proof-of-concept testing, it has been run with open-loop control. In order to be able to adjust to a large range of patients with varying abilities, these two speeds will have to be better controlled and coordinated and a closed-loop controller should be implemented.

- BWS Design – The current BWS design is heavy, and would be difficult for a single clinician to adjust. This section could be fabricated from aluminum tubing instead of the current steel. Bending the aluminum tubing would not only lighten the design and reduce the number of components, it would provide a sleeker, more streamlined design.

- Adjustable BWS – The current BWS does have the option of changing the spring rate to alter the amount of BWS the bicycle seat provides, but in order to provide for a large range of weights and supporting percentages of those weights, many springs would be needed. Although a passive BWS has the advantage of being simple, investigation into either an easily adjustable passive or an active BWS can be made.

- Adding DOFs to BWS – For design simplicity, the current BWS allows vertical motion, pelvic tilt, and rotation about the vertical axis. Investigation into allowing additional degrees of freedom, including lateral motion, and its effect on gait quality should be made. A balance between restricting and allowing motion, gait quality, and the safety of the impaired patient is important.

- Visual Display – A key to successful therapy is keeping the patient motivated and aware of their progress. One method currently employed by many robots, including the Manus and Wrist Robot, is incorporating a visual display. Whether the display has a game this patient plays, or provides scenery to "walk" by, visual input would enhance the therapy experience.

- Combining this device, Elvis-the-Pelvis, and Anklebot – Future development of these three devices could be used together to rehabilitate the entire lower body. Using the Pelvis robot to provide BWS and necessary degrees of freedom of the hips over the actuated treadmill and implementing the Anklebot to actuate ankle movements.

Additional work to further refine this design, specifically the control, will be needed before it can be implemented in a clinic, but this proof-of-concept work has shown the high level of feasibility of this novel design for gait rehabilitation.

References

[1] "Stroke Statistics" [Online] American Heart Association. Available: http://www.americanheart.org/presenter.jhtml?identifier=4725. Accessed December 2008.

[2] Peshkin M, Brown D, Santos-Munne J, et al. KineAssist: a robotic overground gait and balance training device. *Proceedings of the 2005 IEEE 9th International Conference on Rehabilitation Robotics*. 2005;241-246.

[3] "Spinal Cord Injury Facts and Statistics" [Online] SCI-Info Pages. Available: http://www.sci-info-pages.com/facts.html. Accessed December 2008.

[4] Inman V. Human Walking. Baltimore, MD: Williams & Wilkins; 1981.

[5] Trew M, Everett T. Human Movement: An Introductory Text. Edinburgh, NY:Elservier/Churchill Livingstone; 2005.

[6] Whittle M. Gait Analysis: An Introduction. Boston, MA: Butterworth-Heinemann; 1996.

[7] Hooper S. Central Pattern Generators. Encyclopedia of Life Sciences. Macmillan Reference, 2001.

[8] Dietz V, Muller R, Colombo G. Locomotor activity in spinal man: significance of afferent input from joint and load receptors. *Brain*. 2002;125:2626-2634.

[9] Dietz V, Colombo G, Jensen L, et al. Locomotor capacity of spinal cord in paraplegic patients. *Annals of Neurology*. 1995;37:574-582.

[10] Harkema S, Hurley S, Patel U, et al. Human lumbosacral spinal cord interprets loading during stepping. *Journal of Neurophysiology*. 1997;77:797-811.

[11] Kirker S, Simpson D, Jenner J, et al. Stepping before standing: hip muscle function in stepping and standing balance after stroke. *Journal of Neurology, Neurosurgery, and Psychiatry*. 2000;68:458-464.

[12] "Falls Among Older Adults: A Review" [Online] Centers for Disease Control and Prevention: Department of Health and Human Services. Available: http://www.cdc.gov/ncipc/factsheets/adultfalls.htm. Accessed December 2008.

[13] Sawner K, LaVigne J. Brunnstrom's Movement Therapy in Hemiplegia: A Neurophysiological Approach. Philadelphia, PA: J.B. Lippincott Company; 1992.

[14] Bobath B. Adult Hemiplegia: Evaluation and Treatment. Oxford, England: Heinemann Professional Publishing Ltd; 1990.

[15] Davies P. Steps to Follow: A Guide to the Treatment of Adult Hemiplegia. New York, NY: Springer-Verlag; 1985.

[16] Riley P, Paolini G, Croce U, et al. A kinematic and kinetic comparison of overground and treadmill walking in healthy subjects. *Gait and Posture*. 2007;26:17-24.

[17] Lee S, Hidler J. Biomechanics of overground vs. treadmill walking in healthy individuals. *Journal of Applied Physiology*. 2008;104;747-755.

[18] Stolze H, Kuhtz-Buschbeck J, Mondwurf C, et al. Gait analysis during treadmill and overground locomotion in children and adults. *Electroencephalography and clinical Neurophysiology*. 1009;105:490-497.

[19] Matsas A, Taylor N, McBurney H. Knee joint kinematics from familiarized treadmill walking can be generalized to overground walking in young unimpaired subjects. *Gait and Posture*. 2000;11:46-53.

[20] Nilsson L, Carlsson J, Danielsson A, et al. Walking training and patients with hemiparesis at an early state after stroke: a comparison of walking training on a treadmill with body weight support and walking training on the ground. *Clinical Rehabilitation*. 2001;15:515-527.

[21] Hesse S, Bertelt C, Jahnke M, et al. Treadmill training with partial body weight support compared with physiotherapy in nonambulatory hemiparetic patients. *Stroke*. 1995;26:976-981.

[22] Visintin M, Barbeu H, Korner-Bitensky N, et al. A new approach to retrain gait in stroke patients through body weight support and treadmill stimulation. *Stroke*. 1998;29:1122-1128.

[23] Pohl M, Mehrholz J, Ritschel C, et al. Speed-dependent treadmill training in ambulatory hemiparetic stroke patients: a randomized controlled trial. *Stroke*. 2002;33:553-558.

[24] Lamontagne A, Fung J. Faster is better: implications for speed-intensive gait training after stroke. *Stroke*. 2004;35:2543-2548.

[25] Pohl M, Werner C, Holzgraefe, et al. Repetitive locomotor training and physiotherapy improve walking and basic activities of daily living after stroke: a single-blind, randomized multicentre trial (Deutsche GAngtrainerStudie, DEGAS). *Clinical Rehabilitation*. 2007;21:17-27.

[26] Peurala S, Tarkka I, Pitkanen K, et al. The effectiveness of body weight-supported gait training and floor walking in patients with chronic stroke. *Archives of Physical Medicine and Rehabilitation*. 2005;86:1557-1564.

[27] "Rehabilitation Robotics" [Online] Available: http://www.ipk.fraunhofer.de/ rehabrobotics. Accessed December 2008.

[28] Hidler J, Wisman W, Neckel N. Kinematic trajectories while walking within the Lokomat robotic gait-orthosis. *Clinical Biomechanics*. 2008;23:1251-1259.

[29] Jezernik S, Colombo G, Keller T, et al. Robotic orthosis Lokomat: a rehabilitation and research tool. *Neuromodulation*. 2003;6:108-115.

[30] Mayr A, Kofler M, Quirbach E, et al. Prospective, blinded, randomized crossover study of gait rehabilitation in stroke patients using the Lokomat gait orthosis. *Neurorehabilitation and Neural Repair*. 2007;21:307-314.

[31] Hidler J, Wall A. Alteration in muscle activation patterns during robotic-assisted walking. *Clinical Biomechanics*. 2005;20:184-193.

[32] Hornby T, Campbell D, Kahn J, et al. Enhanced gait-related improvements after therapist-versus robotic-assisted locomotor training in subjects with chronic stroke: a randomized control study. *Stroke*. 2008;39:1786-1792.

[33] Hidler, J, Nichols, D, Pelliccio, M, et al. Multicenter Randomized Clinical Trial Evaluating the Effectiveness of the Lokomat in Subacute Stroke. *Neurorehabilitation and Neural Repair*. 2009;23:5-13.

[34] Collins S, Wisse M, Ruina A. A three-dimensional passive-dynamic walking robot with two legs and knees. *The International Journal of Robotics Research*. 2001;20:607-615.

[35] Altshuller G. And Suddenly the Inventor Appeared: TRIZ, the Theory of Inventive Problem Solving. Worcester, MA: Technical Innovation Center, 2006.

[36] Altshuller G. 40 Principles: TRIZ Keys to Technical Innovation. Worcester, MA: Technical Innovation Center, 2005.

[37] Tilley A. The Measure of Man and Woman: Human Factors in Design. New York, NY: Wiley; 1993.

[38] Wilson M, Qureshy H, Protas E, et al. Equipment specifications for supported treadmill ambulation training. *Journal of Rehabilitation Research and Development*. 2000;37:415-422.

[39] Norton R. Cam Design and Manufacturing Handbook. New York, NY: Industrial Press, Inc.; 2002.

[40] Norvelle F. Electrohydraulic Control Systems. Upper Saddle River, NJ: Prentice Hall; 2003.

[41] He J, Kram R, McMahon T. Mechanics of running under simulated low gravity. *Journal of Applied Physiology*. 1991;71:863-870.

[42] Roberts M. *A Robot for Gait Rehabilitation*. MSME Thesis, Massachusetts Institute of Technology, June 2004.

[43] Krebs H. Robot-mediated movement therapy: a tool for training and evaluation. Technical Aids for Rehabilitation (TAR) – 2007, Technical University of Berlin, July 25-26, 2007.

[44] Hibbeler R. Mechanics of Materials 5th Edition. Upper Saddle River, NJ: Pearson Education, Inc.; 2003.

[45] "Chrome-moly Steel" [Online] Available: http://www.matweb.com. Accessed December 2008.

[46] "Bearings Reference Center" [Online] Available http://www.bearings.machinedesign.com/BDEList.aspx. Accessed December 2008.

[47] Harris T. Rolling Bearing Analysis. New York, NY: Wiley; 2001.

[48] "80/20 Product Catalog" [Online] Available http://www.8020.net/. Accessed December 2008.

[49] Nise N. Control Systems Engineering, 4th Edition. Hoboken, NJ: John Wiley & Sons, Inc.; 2004.

[50] Winter D. Biomechanics and Motor Control of Human Movement. Hoboken: NJ: John Wiley & Sons, Inc.; 2005.

[51] Basmajian J. Muscles Alive : Their Functionality Revealed by Electromyography, 5th Edition. Baltimore, MD: Williams & Wilkins; 1985.

[52] Gasparo L. Atlas of Human Anatomy. Philadelphia, PA: W.B. Saunders Company; 1970.

[53] McGowan C, Neptune R, Kram R. Independent effects of weight and mass on plantar flexor activity during walking: implications for their contributions to body support and forward propulsion. *Journal of Applied Physiology*. 2008; 105:486-494.

Appendix A

TreadClimber® Specifications

Throughout this manual, all references to the left or right side, and to the front or back, are made as if you were on the TreadClimber® machine, ready to exercise. For example, the power cord is plugged into the incoming power plug at the back of the base.

The dimensions and general specifications for the Bowflex® TreadClimber® exercise machine are as follows:

Physical Dimensions	
Length	46 inches (117 cm)
Width	28.5 inches (72.5 cm)
Height	55.25 inches (140.5 cm)
Weight	185 pounds (84 kg)
Shipping Weight	220 pounds (100 kg)
System Capacities	
Maximum Weight Capacity	300 lbs (136 kgs)
Speed	
TC1000	0.5 to 3.8 MPH (0.8 to 6.1KPH)
TC3000 and TC5000	0.7 to 4.0 MPH (1.1 to 6.4 KPH)
Workout Resistance Levels	1 to 12
Warranty Length	See the Warranty section for full information per machine type
Component Specifications	
Belt	7.75 in x 38.5 in (19.5 cm x 98 cm)
Motor	0.5 hp continuous duty
Treadmill Incline	10% Grade
Frame	Powder-coated steel
Operational Voltage	95 to 130 VAC 50 - 60 Hz
Operational Current	10A Max
Breaker	12A
Always use a 15A circuit with no loads. A short 14 gauge, 3 wire extension cord is permissible.	
Regulatory Approvals	UL CSA
Patent Information	U.S. and International Patents Pending

Electrical Layout (TC 3000 and TC 5000)

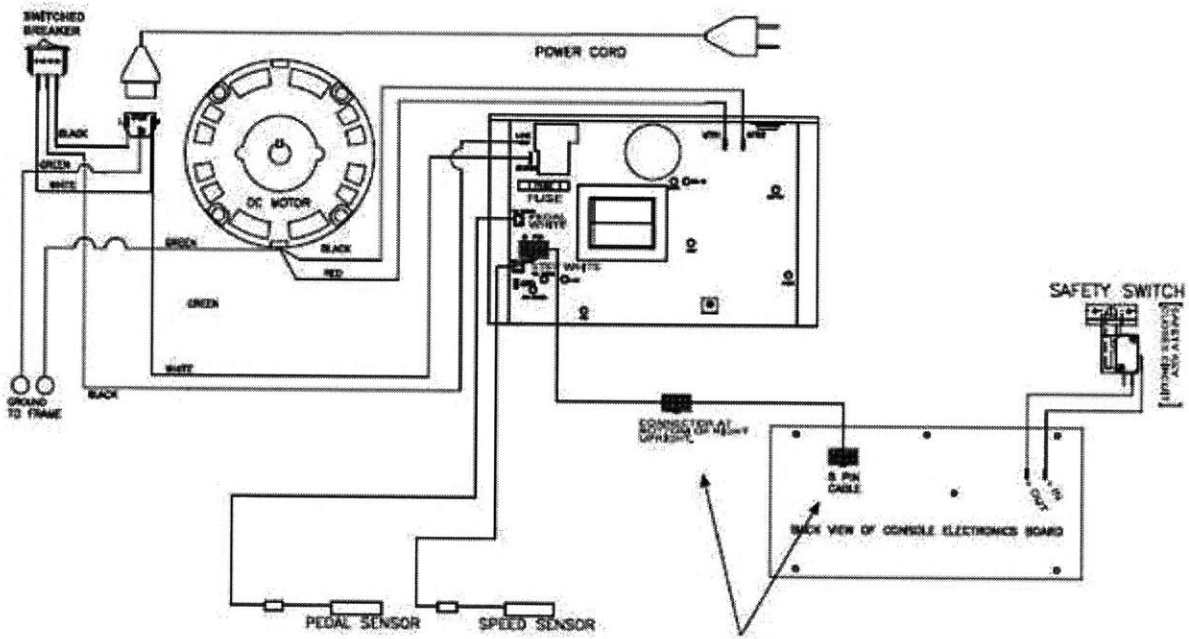

TC 110V SCHEMATIC

ITC 3000 /

Connector Pin Numbering

4	3	2	1
8	7	6	5

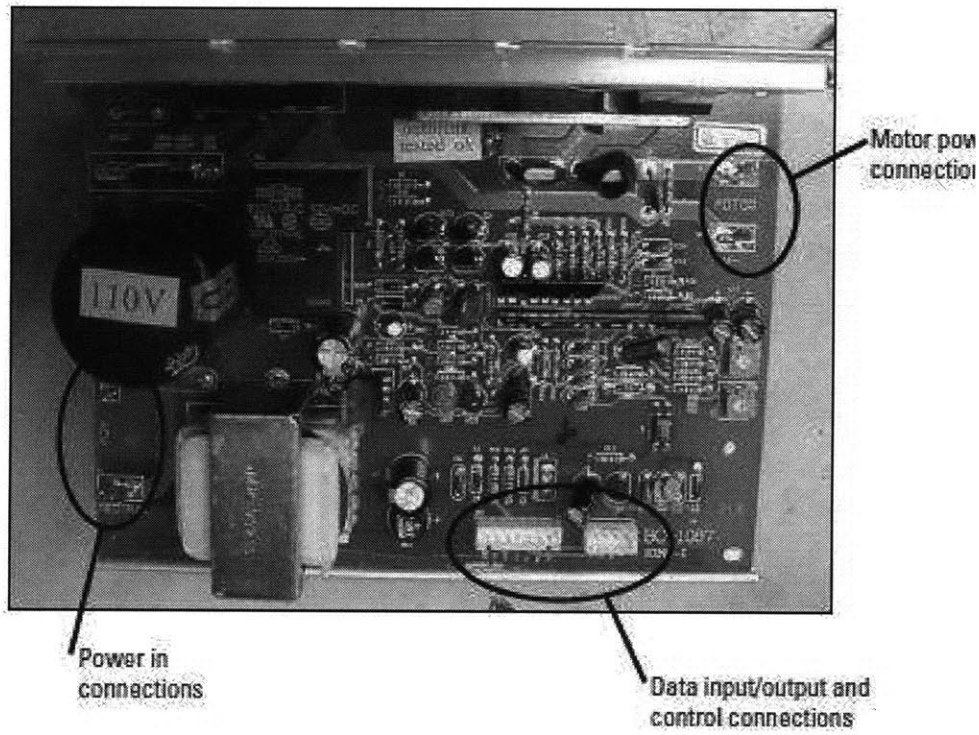

TC1000 MCB

8-Pin Connector Diagram (for experienced technicians, will require a multi-tester)

PIN NUMBER	CONNECTION	COLOR	VOLTS
Pin 8	Pedal RPM	Grey	5VDC
Pin 7	RPM In	Purple	5VDC
Pin 6	Vin	Blue	15VCD to 18VDC
Pin 5	Vin	Green	15VCD to 18VDC
Pin 4	GND	Yellow	0V
Pin 3	GND	Orange	0V
Pin 2	LCB Relay	Red	5VDC to 12VDC
Pin 1	PWM Out	Brown	5VDC

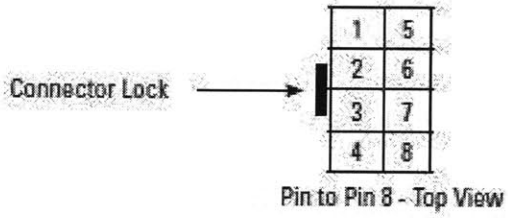

Pin to Pin 8 - Top View

Cam Motor Specifications:

AKM4x - Up to 640 VDC

See system data beginning on page 8 for typical torque/speed performance

	PARAMETER	Tol	SYMBOL	UNITS	AKM41 C	AKM41 E	AKM41 H	AKM42 C	AKM42 E	AKM42 G	AKM42 J	AKM43 E	AKM43 G	AKM43 K	AKM44 E	AKM44 G	AKM44 J
	Max Rated DC Bus Voltage	Max	V_{bus}	Vdc	640	640	320	640	640	640	320	640	640	320	640	640	640
	Continuous Torque (Stall) for ΔT winding = 100°C ①②③④	Nom	T_{cs}	N-m	1.95	2.82	2.06	3.35	3.42	3.53	3.56	4.70	4.80	4.90	5.76	5.88	6.00
				lb-in	17.3	17.9	18.2	29.6	30.3	31.2	31.5	41.6	42.5	43.4	51.0	52.0	53.1
	Continuous Current (Stall) for ΔT winding = 100°C ①②③④	Nom	I_{cs}	A_{rms}	1.46	2.85	5.68	1.40	2.74	4.80	8.40	2.76	4.87	9.60	2.9	5.0	8.8
	Continuous Torque (Stall) for ΔT winding = 60°C ②	Nom	T_{cs}	N-m	1.56	1.62	1.65	2.68	2.74	2.82	2.85	3.76	3.84	3.92	4.61	4.70	4.80
				lb-in	13.8	14.3	14.6	23.7	24.2	25.0	25.2	33.3	34.0	34.7	40.8	41.6	42.5
	Max Mechanical Speed ④	Nom	N_{max}	rpm	6000	6000	6000	6000	6000	6000	6000	6000	6000	6000	6000	6000	6000
	Peak Torque ①②	Nom	T_p	N-m	6.12	6.28	6.36	11.1	11.3	11.5	11.6	15.9	16.1	16.3	19.9	20.2	20.4
				lb-in	54.2	55.6	56.3	98.8	99.7	102	103	141	142	144	176	179	181
	Peak Current	Nom	I_p	A_{rms}	5.8	11.4	22.4	5.61	11.0	19.2	33.7	11.0	19.5	38.3	11.4	20.0	35.2
75VDC	Rated Torque (speed) ①②③④ *		T_{rtd}	N-m	-	-	1.99	-	-	-	-	-	-	-	-	-	-
				lb-in	-	-	17.6	-	-	-	-	-	-	-	-	-	-
	Rated Speed		N_{rtd}	rpm	-	-	1000	-	-	-	-	-	-	-	-	-	-
	Rated Power (speed) ①②③④		P_{rtd}	kW	-	-	0.21	-	-	-	-	-	-	-	-	-	-
				Hp	-	-	0.28	-	-	-	-	-	-	-	-	-	-
160VDC	Rated Torque (speed) ①②③④ *		T_{rtd}	N-m	-	1.94	1.86	-	-	-	3.03	-	-	4.08	-	-	-
				lb-in	-	17.2	16.5	-	-	-	26.8	-	-	36.1	-	-	-
	Rated Speed		N_{rtd}	rpm	-	1200	3000	-	-	-	3000	-	-	2500	-	-	-
	Rated Power (speed) ①②③④		P_{rtd}	kW	-	0.24	0.58	-	-	-	0.95	-	-	1.07	-	-	-
				Hp	-	0.33	0.78	-	-	-	1.28	-	-	1.43	-	-	-
320VDC	Rated Torque (speed) ①②③④ *		T_{rtd}	N-m	1.88	1.82	1.62	-	3.12	2.90	2.38	4.24	4.00	2.62	5.22	4.98	3.84
				lb-in	16.6	16.1	14.3	-	27.6	25.7	21.1	37.5	35.4	23.2	46.2	41.4	34.0
	Rated Speed		N_{rtd}	rpm	1200	3000	6000	-	1800	3500	6000	1500	2500	6000	1200	3000	4000
	Rated Power (speed) ①②③④		P_{rtd}	kW	0.24	0.57	1.02	-	0.59	1.06	1.50	0.67	1.05	1.65	0.65	1.03	1.01
				Hp	0.32	0.77	1.36	-	0.79	1.42	2.00	0.89	1.40	2.21	0.88	1.38	2.16
560VDC	Rated Torque (speed) ①②③④ *		T_{rtd}	N-m	1.77	1.58	-	3.10	2.81	2.35	-	3.92	3.01	-	4.80	3.76	2.75
				lb-in	15.7	14.0	-	27.4	24.9	20.8	-	34.7	26.6	-	42.5	33.3	24.3
	Rated Speed		N_{rtd}	rpm	3000	6000	-	1500	3500	6000	-	2500	5000	-	2000	4000	6000
	Rated Power (speed) ①②③④		P_{rtd}	kW	0.56	0.99	-	0.49	1.03	1.48	-	1.03	1.58	-	1.01	1.57	1.73
				Hp	0.75	1.33	-	0.65	1.38	1.98	-	1.38	2.11	-	1.35	2.11	2.32
640VDC	Rated Torque (speed) ①②③④ *		T_{rtd}	N-m	1.74	1.58	-	3.02	2.72	2.35	-	3.76	2.57	-	4.56	3.19	2.75
				lb-in	15.4	14.0	-	26.7	24.1	20.8	-	33.3	22.7	-	40.4	28.2	24.3
	Rated Speed		N_{rtd}	rpm	2500	6000	-	2000	4000	6000	-	3000	6000	-	2500	5000	6000
	Rated Power (speed) ①②③④		P_{rtd}	kW	0.64	0.99	-	0.63	1.14	1.48	-	1.18	1.61	-	1.19	1.67	1.73
				Hp	0.86	1.33	-	0.85	1.53	1.98	-	1.58	2.16	-	1.60	2.24	2.32
	Torque Constant ①	±10%	K_t	N-m/A_{rms}	1.34	0.71	0.37	2.48	1.26	0.74	0.42	1.72	0.99	0.52	2.04	1.19	0.69
				lb-in/A_{rms}	11.9	6.3	3.3	21.2	11.2	6.5	3.8	15.2	8.8	4.6	18.1	10.5	6.1
	Back EMF constant ④	±10%	K_e	V/k_{rpm}	86.3	45.6	23.7	154	80.9	47.5	27.5	111	63.9	33.2	132	76.6	44.2
	Resistance (line-line) ①	±10%	R_m		21.7	5.7	1.51	27.52	7.22	2.28	0.80	8.04	2.81	0.70	8.64	2.65	0.88
	Inductance (line-line)		L	mH	66.1	18.4	5.0	97.4	26.8	9.2	3.1	32.6	10.8	2.9	33.9	11.5	3.8
	Inertia		J_m	kg-cm²	0.81			1.5				2.1			2.7		
	(Includes Resolver feedback) ③			lb-in-s²	7.2E-04			1.3E-03				1.8E-03			2.4E-03		
	Optional Brake Inertia		J_m	kg-cm²	0.058			0.068				0.068			0.068		
	(Add to total)			lb-in-s²	6.0E-05			6.0E-05				6.0E-05			6.0E-05		
	Weight		W	kg	2.44			3.39				4.35			5.3		
				lb	5.4			7.5				9.6			11.7		
	Static Friction ③⑨		T_f	N-m	0.014			0.026				0.038			0.05		
				lb-in	0.12			0.23				0.34			0.44		
	Viscous Damping ①		K_dv	N-m/k_{rpm}	0.009			0.013				0.017			0.021		
				lb-in/k_{rpm}	0.08			0.12				0.15			0.19		
	Thermal Time Constant		TCT	minutes	13			17				20			24		
	Thermal Resistance		R_{thw-a}	°C/W	1.04			0.89				0.78			.71		
	Pole Pairs				5			5				5			5		
	Heatsink Size				10"X10"X¼" Aluminum Plate			10"X10"X¼" Aluminum Plate				10"X10"X¼" Aluminum Plate			10"X10"X¼" Aluminum Plate		

Notes:
1. Motor winding temperature rise, ΔT = 100°C, at 40°C ambient.
2. All data referenced to sinusoidal commutation.
3. Add parking brake if applicable for total inertia.
4. Motor with standard heatsink.
5. May be limited at some values of Vbus.
6. Measured at 25°C.
7. Brake motor option reduces continuous torque ratings by 0.12 N-m.
8. Commutating encoder/SFD options reduces continuous ratings by:
   AKM41 = 0.1 N-m AKM42 = 0.1 N-m
   AKM43 = 0.2 N-m AKM44 = 0.3 N-m
9. Brake plus commutating encoder/SFD motor option reduces continuous torque ratings by:
   AKM41 = 0.22 N-m AKM42 = 0.36 N-m
   AKM43 = 0.55 N-m AKM44 = 0.76 N-m
10. For motors with optional shaft seal, reduce torque shown by 0.071 N-m (0.63 lb-in), and increase T_f by the same amount.

DANAHER MOTION is a registered trademark of Danaher Corporation. Danaher Motion makes every attempt to ensure accuracy and reliability of the specifications in this publication. Specifications are subject to change without notice. Danaher Motion provides this information "AS IS" and disclaims all warranties, express or implied, including, but not limited to, implied warranties of merchantability and fitness for a particular purpose. It is the responsibility of the product user to determine the suitability of this product for a specific application. ©2004 Danaher Motion.

Recommended Motor/Drive Systems, 480 VAC, 640VDC ①

Servo Motor Model	Servo Drive Model	Peak Stall Torque T_{ps} ② N-m (lb-in)	Peak Torque at at Max. Speed T_{ms} N-m (lb-in)	Cont. Stall Torque T_{cs} N-m (lb-in)	Cont. Rated Torque T_{cr} N-m (lb-in)	Speed at Knee ω_k rpm	Rated Speed ω_r rpm	wmax. Speed ω_{max} rpm	Cont. Stall Current I_{cs} A_{rms}	Current@ Peak Torque I_{ps} A_{rms}	Inertia ③ J kg-cm² (lb-in-s² x 10^{-3})
AKM23D	S60300	2.87 (25.4)	2.87 (25.4)	1.16 (10.2)	0.92 (8.11)	8,000	8,000	8,000	2.19	6.0	0.216 (0.191)
AKM24D	S60300	3.52 (31.2)	3.52 (31.2)	1.41 (12.4)	1.11 (9.81)	8,000	8,000	8,000	2.21	6.0	0.27 (0.239)
AKM32D	S60300	5.14 (45.5)	0.0 (0.0)	2.04 (18.0)	1.58 (14)	5,500	6,000	7,510	2.23	6.0	0.59 (0.522)
AKM33E	S60300	6.35 (56.2)	0.0 (0.0)	2.79 (24.7)	2.27 (20.1)	5,050	5,000	6,280	2.58	6.0	0.85 (0.752)
AKM41E	S60300	3.87 (34.2)	3.87 (34.2)	2.02 (17.8)	1.58 (14.0)	6,000	6,000	6,000	2.85	6.0	0.81 (0.717)
AKM42E	S60300	6.97 (61.7)	0.0 (0.0)	3.42 (30.3)	2.72 (24.1)	3,850	4,000	5,480	2.74	6.0	1.45 (1.28)
AKM42G	S60600	7.99 (70.7)	7.99 (70.7)	3.53 (31.2)	2.35 (20.8)	6,000	6,000	6,000	4.8	12.0	1.45 (1.28)
AKM43E	S60300	9.67 (85.6)	0.0 (0.0)	4.7 (41.6)	3.76 (33.3)	2,910	3,000	4,000	2.76	6.0	2.09 (1.85)
AKM43G	S60600	10.9 (96.8)	6.7 (59.3)	4.8 (42.5)	2.57 (22.7)	4,950	6,000	6,000	4.87	12.0	2.09 (1.85)
AKM44E	S60300	11.6 (103)	0.0 (0.0)	5.76 (51)	4.56 (40.4)	2,570	2,500	3,370	2.85	6.0	2.73 (2.42)
AKM44G	S60600	13.3 (118)	0.0 (0.0)	5.88 (52.0)	3.19 (28.2)	4,350	5,000	5,790	5.0	12.0	2.73 (2.42)
AKM44J	S610-3000	18.1 (160)	18.1 (160)	6.0 (53.1)	2.75 (24.3)	6,000	6,000	6,000	8.8	30.0	2.73 (2.42)
AKM51E	S60300	9.14 (80.9)	0.0 (0.0)	4.7 (41.6)	3.8 (33.7)	2,770	3,000	4,010	2.75	6.0	3.42 (3.03)
AKM51G	S60600	10.2 (90.4)	5.9 (52.2)	4.75 (42.1)	1.94 (17.2)	4,680	6,000	6,000	4.84	12.0	3.42 (3.03)
AKM52E	S60300	15.4 (136)	0.0 (0.0)	8.34 (73.8)	7.28 (64.4)	1,890	2,000	2,470	3.0	6.0	6.22 (5.51)
AKM52G	S60600	18.9 (168)	0.0 (0.0)	8.43 (74.6)	6.66 (59)	2,750	3,000	3,840	4.72	12.0	6.22 (5.51)
AKM52K	S61000	16.9 (150)	15.8 (140)	8.6 (76.1)	3.25 (28.8)	5,890	6,000	6,000	9.3	20.0	6.22 (5.51)
AKM52K	S610-3000	21.9 (194)	15.7 (139)	8.6 (76.1)	3.25 (28.8)	4,990	6,000	6,000	9.3	27.8	6.22 (5.51)
AKM53G	S60600	25.8 (229)	0.0 (0.0)	11.4 (101)	9.5 (84)	2,160	2,400	2,880	4.77	12.0	9.12 (8.07)
AKM53K	S61000	22.9 (203)	0.0 (0.0)	11.6 (103)	6.85 (60.6)	4,650	4,500	5,550	9.4	20.0	9.12 (8.07)
AKM53K	S610-3000	30.2 (267)	0.0 (0.0)	11.6 (103)	6.85 (60.6)	4,014	4,500	5,550	9.4	28.1	9.12 (8.07)
AKM54G	S60600	31.7 (280)	0.0 (0.0)	14.3 (126)	12.3 (109)	1,860	2,000	2,390	5.0	12.0	11.9(10.6)
AKM54K	S61000	28.1 (249)	0.0 (0.0)	14.4 (127)	9.25 (81.9)	3,960	4,000	4,590	9.7	20.0	11.9(10.6)
AKM54K	S610-3000	38.4 (340)	0.0 (0.0)	14.4 (127)	9.25 (81.9)	3,410	4,000	4,590	9.7	29.2	11.9(10.6)
AKM62G	S60600	25.6 (227)	0.0 (0.0)	11.9 (106)	10.2 (90.1)	1,780	2,000	2,790	4.85	12.0	16.9 (15)
AKM62K	S61000	22.7 (201)	0.0 (0.0)	12.2 (108)	8.02 (71)	3,900	4,500	5,400	9.6	20.0	16.9 (15)
AKM62K	S610-3000	30.1 (267)	0.0 (0.0)	12.2 (108)	8.02 (71)	3,130	4,500	5,400	9.6	28.7	16.9 (15)
AKM62M	S61400	22.8 (201)	18.8 (166)	12.2 (108)	5.74 (50.8)	5,480	6,000	6,000	13.4	28.0	16.9 (15)
AKM63G	S60600	38.4 (340)	0.0 (0.0)	16.5 (146)	14.6 (128)	1,200	1,500	1,860	4.48	12.0	24.2 (21.4)
AKM63K	S61000	31 (274)	0.0 (0.0)	16.8 (149)	12 (106)	3,170	3,500	4,030	9.9	20.0	24.2 (21.4)
AKM63K	S610-3000	42.6 (377)	0.0 (0.0)	16.8 (149)	12 (106)	2,580	3,500	4,030	9.9	29.7	24.2 (21.4)
AKM63M	S61400	31.4 (278)	0.0 (0.0)	17 (150)	10.5 (92.9)	4,400	4,500	5,550	13.8	28.0	24.2 (21.4)
AKM63N	S62000	34.8 (308)	24.6 (218)	17 (150)	7.0 (62)	5,260	6,000	6,000	17.4	40.0	24.2 (21.4)
AKM64K	S61000	41.2 (365)	0.0 (0.0)	20.8 (184)	16.3 (145)	2,400	2,500	3,030	9.2	20.0	31.6 (28)
AKM64K	S610-3000	53.5 (474)	0.0 (0.0)	20.8 (184)	16.3 (145)	2,050	2,500	3,030	9.2	27.5	31.6 (28)
AKM64L	S61400	41.9 (371)	0.0 (0.0)	21 (186)	14.4 (127)	3,340	3,500	4,160	12.8	28.0	31.6 (28)
AKM64P	S62000	40.2 (355)	15.6 (138)	20.4 (180)	9.02 (79.8)	5,130	5,500	6,000	18.6	40.0	31.6 (28)
AKM65K	S61000	46.8 (414)	0.0 (0.0)	24.8 (219)	19.7 (175)	2,260	2,200	2,710	9.8	20.0	40.0 (35.4)
AKM65K	S610-3000	64.5 (571)	0.0 (0.0)	24.8 (219)	19.7 (175)	1,900	2,200	2,710	9.8	29.4	40.0 (35.4)
AKM65M	S61400	47.6 (421)	0.0 (0.0)	25 (221)	18.1 (160)	3,120	3,000	3,720	13.6	28.0	40.0 (35.4)
AKM65N	S62000	50.2 (444)	0.0 (0.0)	24.3 (215)	14.7 (131)	4,120	4,000	5,000	17.8	40.0	40.0 (35.4)
AKM72K	S61000	59.4 (526)	0.0 (0.0)	29.7 (263)	24 (213)	1,560	1,800	2,130	9.3	20.0	64.5 (57.1)
AKM72K	S610-3000	79.2 (701)	0.0 (0.0)	29.7 (263)	24 (213)	1,280	1,800	2,130	9.3	27.8	64.5 (57.1)
AKM72M	S61400	59.8 (529)	0.0 (0.0)	30 (266)	22.1 (196)	2,180	2,500	2,960	13	28.0	64.5 (57.1)
AKM72P	S62000	58.4 (516)	0.0 (0.0)	29.4 (260)	18.2 (161)	3,280	3,500	4,350	18.7	40.0	64.5 (57.1)
AKM73M	S61400	80.7 (714)	0.0 (0.0)	42 (372)	32.1 (284)	1,740	1,800	2,220	13.6	28.0	94.1 (81.5)
AKM73P	S62000	79.4 (702)	0.0 (0.0)	41.6 (368)	26.3 (233)	2,570	2,800	3,230	19.5	40.0	94.1 (81.5)
AKM74L	S61400	108 (952)	0.0 (0.0)	53 (469)	41.5 (367)	1,300	1,400	1,660	12.9	28.0	120.0 (105)
AKM74P	S62000	106 (938)	0.0 (0.0)	52.5 (464)	35.9 (318)	1,930	2,000	2,420	18.5	40.0	120.0 (105)

① See definitions of ratings beginning on page 8.
② Peak torque ratings are for 5 seconds.
③ Includes resolver feedback inertia.

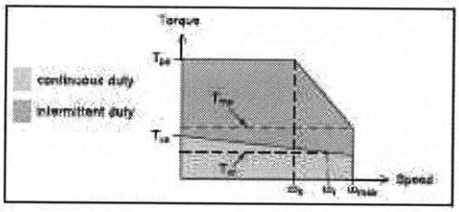

DANAHER MOTION is a registered trademark of Danaher Corporation. Danaher Motion makes every attempt to ensure accuracy and reliability of the specifications in this publication. Specifications are subject to change without notice. Danaher Motion provides this information "AS IS" and disclaims all warranties, express or implied, including, but not limited to, implied warranties of merchantability and fitness for a particular purpose. It is the responsibility of the product user to determine the suitability of this product for a specific application. ©2004 Danaher Motion.

AKM Series Brushless Servomotors

PN: AKM43E - ANMNEH00

AKM 4 2 E - EK C N R - 00

AKM Series

Motor Frame Size
1, 2, 3, 4, 5, 6, 7

Rotor Stack Length
1, 2, 3, 4, 5

Winding Type
A, B, C, D, etc.
S = Special

Mount
A = International standard mount
B = NEMA mount
C = Alternative standard mount
D = Alternative standard mount
E = NEMA mount
S = Special

Shaft
C = Closed keyway
K = Open keyway
N = Smooth shaft
S = Special

See pages 16-29 for details on mount / shaft option codes and availability.

Connectors
C = 0.5 meter shielded cables w/ IP65 connectors (AKM1, 2)
= Motor-mounted rotatable IP65 connectors (AKM3, 4, 5, 6, 7)
D = Single motor-mounted rotatable IP65 connector (AKM3, 4 models with SFD and no brake)
M = 0.5 meter shielded cables w/ IP20 plugs (AKM1, 2, 3, 4 models less than 6 amps)
P = 0.5 meter shielded cables w/ single IP20 plug (AKM1, 2, 3, 4 models with SFD and no brake, less than 6 amps)
S = Special

Brake
2 = 24 VDC brake (AKM2, 3, 4, 5, 6, 7 models)
N = No brake
S = Special

Feedback Device
1 - = 1024 PPR digital encoder w/ commutation
2 - = 2048 PPR digital encoder w/ commutation
C - = Smart feedback device (SFD) (AKM1, 2, 3, 4 models only)
R - = Resolver
DA = Single-turn Absolute Sine Encoder
DB = Multi-turn Absolute Sine Encoder
ED = 500 PPR digital encoder w/ commutation
EE = 1000 PPR digital encoder w/ commutation
EF = 2000 PPR digital encoder w/ commutation
EG = 2500 PPR digital encoder w/ commutation
EM = 4096 PPR digital encoder w/ commutation
EH = 5000 PPR digital encoder w/ commutation
EN = 8192 PPR digital encoder w/ commutation (AKM5, 6, 7 models only)
EJ = 10,000 PPR digital encoder w/ commutation (AKM5, 6, 7 models only)

Customization / Seal
00 = Standard motor w/o shaft seal
01 = Standard motor w/ shaft seal
Other #'s will be assigned for special motors.

Gear reducer specifications

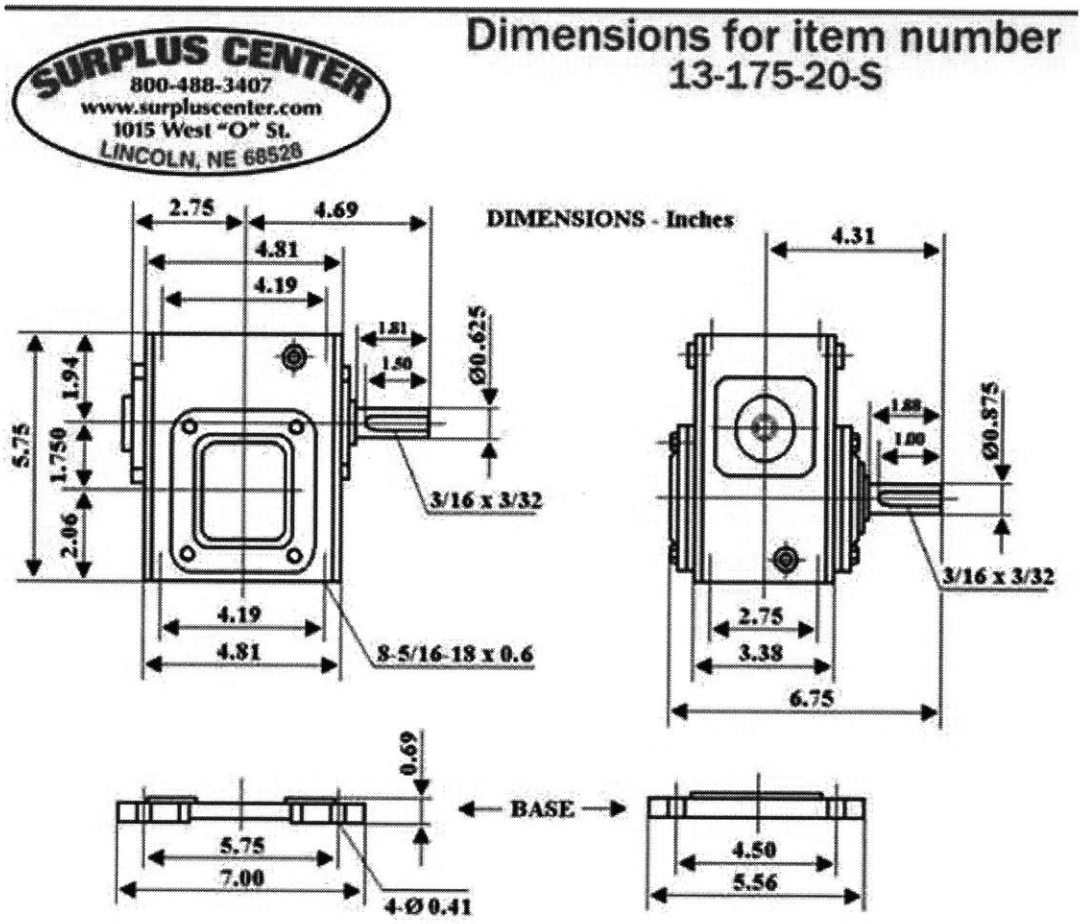

20:1 GEAR REDUCER

New, WORLDWIDE ELECTRIC cast iron right-angle worm gear-reducer. Left hand output shaft when viewed from input shaft. Can be easily swapped to give right hand output. Tapped mounting holes on top and bottom of case. Mounting base supplied. Input can be direct coupled, belt or chain driven.

SPECIFICATIONS

- 20:1 gear ratio
- .89 HP input
- 1750 RPM input
- 88 RPM output
- 337 in-lbs output torque
- 2.06" Output centerline height
- 5/8" x 1-3/4"dia. keyed input shaft
- 7/8" diam. x 1-7/8"keyed output shaft
- 2.75"x 4.19" mgt bolt pattern
- Overall size 7-1/8" x 6-1/2" x 7-1/8"
- Shpg 30 lbs

Bearing Specifications:

Timkin Taper Roller Bearing – Cup PN: 15100, Cone PN: 15245

Dimensions, mm (inches)			Load Ratings, N (lbf.)						
			Dynamic (1)	Factors (5)		Dynamic (2)	Factors (5)		Static
d	B	T	C_a	e	Y	C_{ea}	C_{ea0}	K	C_0
25.400	62.000	19.050	46800	0.35	1.71	12100	7280	1.67	53900
1.0000	2.4409	0.7500	10500			2730	1640		12100

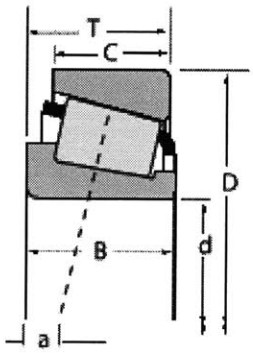

Dimensions, mm (inches)										
Bearing			Shaft			Housing			Cage	
			max shaft fillet radius	backing shoulder dia.	backing shoulder dia.		backing shoulder dia.			
B	C	a (3)	r_{as} (4)	d_a	d_b	r_{as} (4)	D_a	D_b	A_a	A_b
20.638	14.288	-5.8	3.5	31.5	38.0	1.3	58.0	55.0	1.20	1.00
0.8125	0.5625	-0.23	0.14	1.24	1.50	0.05	2.28	2.17	0.05	0.04

Factors			Weight kg (lbs.)
G_1	G_2	G_3	
14.6	7.58	0.0606	0.29
			0.65

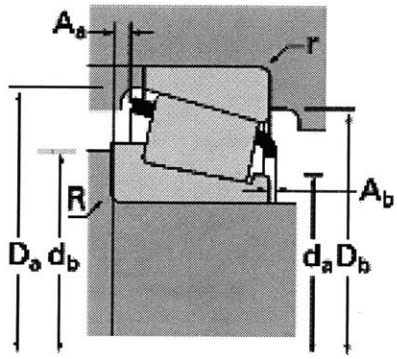

Specifications

System	DE-2.1 Bagnoli™ Single Differential	DE-3.1 Bagnoli™ Double Differential	DE-2.3 Myomonitor® Single Differential
Mechanical			
Number of Contacts	2	3	2
Contact Dimension	10.0 x 1.0 mm	10.0 x 1.0 mm	10.0 x 1.0 mm
Contact Spacing	10.0 mm	10.0 mm	10.0 mm
Contact Material	99.9% Ag	99.9% Ag	99.9% Ag
Detection Area	100 mm²	200 mm²	100 mm²
Case Dimensions	41 x 20 x 5 mm	41 x 20 x 5 mm	41 x 20 x 5 mm
Case Material	Polycarbonate	Polycarbonate	Polycarbonate
Cable Length	1.67 m	1.67 m	1.67 m
Connector	Hypertronics D04	Hypertronics D04	Hypertronics D04
Temperature Range	0-40 °C	0-40 °C	0-40 °C
Electrical			
Preamplifier Gain	10 V/V ±1%	10 V/V ±1% (per diff. pair)	1000 V/V ±1%
Bandwidth	open	open	20-450 Hz ±10%
Noise	1.2 µV (RMS, R.T.I.)	1.2 µV (RMS, R.T.I.)	1.5 µV (RMS, R.T.I.)
CMRR (0-500 Hz)	-92 dB (typical)	-92 dB (typical)	-92 dB (typical)
Power Consumption	20 mW (typical)	46 mW (typical)	40 mW (typical)
Input Impedance	>10^{15}Ω // 0.2pF	>10^{15}Ω // 0.2pF	>10^{15}Ω // 0.2pF

Comfort

Convenience

Full Range

DELSYS Sensors are unsurpassed in signal quality, resolution, and range of detection. All electrode models share unique input characteristics that guarantee low-noise signals and hassle-free recordings.

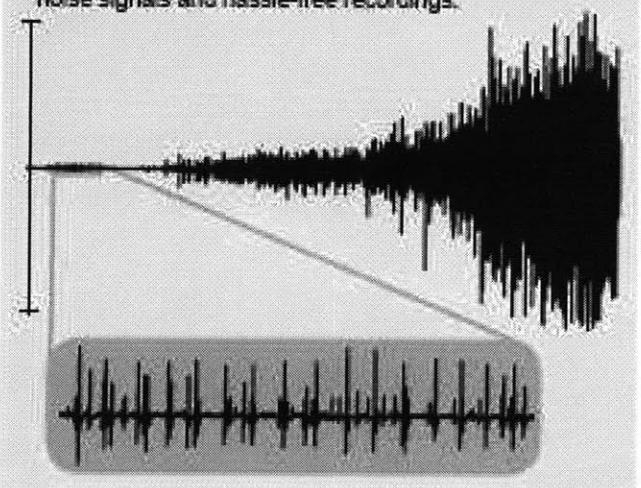

High Definition

Comprehensive

DE-2.1 Sensors are designed for a broad range of applications, ideally-suited to capture all EMG activity with precision and expediency.

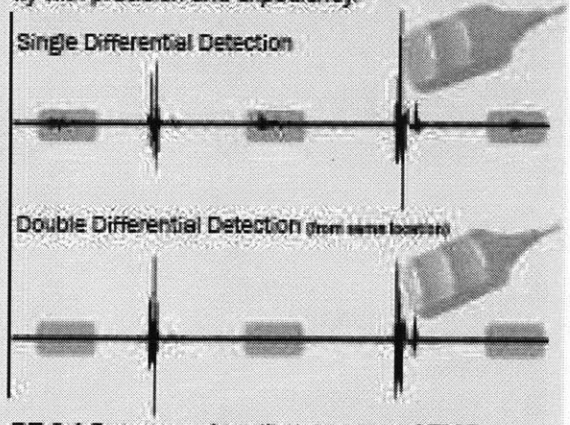

DE-3.1 Sensors reduce the presence of EMG crosstalk. Our Double-Differential approach offers unique research strategies for the discerning electromyographer.

Selective

www.delsys.com PO Box 15734, Boston, MA 02215 617 236 0599 (Tel) 617 236 0549 (Fax)

Appendix B: Kinematic Robot-Based Evaluation Scales and Clinical Counterparts to Measure Upper Limb Motor Performance in Patients with Chronic Stroke

This appendix includes work completed to investigate if the Manus robot metrics could be used to calculate four common clinical scores of upper extremity function, Fugl-Meyer Assessment, Motor Status Score, Motor Power Score, and Modified Ashworth Scale. First, a paper prepared outlining the development of linear regression models with Manus metrics to predict the clinical scores of 111 chronic stroke patients is presented. Next, further analysis of the Fugl-Meyer score is shown, followed by a brief description of the method for implementing a principle component analysis.

B1 Introduction

Stroke is the leading cause of permanent disability in the U.S.A.[1] While occupational and physical therapy are widely-accepted treatments for upper extremity dysfunction in stroke patients, they are labor-intensive and therefore expensive. Changes in the health care system and budgetary constraints have provided pressure to reduce the cost of therapy. Until recently, that has been done by shortening inpatient rehabilitation hospitalizations, but once the practical limit of abbreviated inpatient stays is reached, further efficiencies will be attainable chiefly by addressing clinical practices themselves.

Our research has demonstrated that the efficiency of care among stroke patients could be increased by the application of robotics and information technology, and these results have been confirmed by others[2-4]. Labor-intensive procedures have traditionally been a primary field for the application of robotics. Over the past decade, we have shown that labor-intensive physical therapies for stroke patients can be delivered safely and effectively by robotic aids. Such an approach has several major advantages over traditional motor therapies. Robots can be used to generate objective measures of patients' impairment and therapy outcome, assist in diagnosis, customize therapies based on patients' motor abilities, and assure compliance with treatment regimens and maintain patients' records. For the upper extremity, the most employed and deployed therapeutic robot is the MIT-Manus[5]. Developed by our group, this robot controls

patients' arm movement in the horizontal plane. A number of studies have shown that therapy with the MIT-Manus, and its commercial version InMotion2, are safe, tolerated, and clinically effective as measured by traditional clinical scales such as the Fugl-Meyer Assessment (FMA) and the Motor Status Score (MSS)[6-15]. Metrics extracted from movement data recorded from patients undergoing MIT-Manus therapy have been used for quantifying patients' motor abilities and their changes during motor recovery and have offered unprecedented insights into the process of motor recovery from stroke[16-18]. It remains unclear how these robot-based kinematic and kinetic metrics relate to traditional human-administered clinical scales for measuring outcome.

The goal of this study was to test the feasibility of deriving models to estimate clinical scores for the upper extremity from robot-based metrics. Such models would facilitate objective outcome measurement, freeing the therapist to render additional therapy, and ultimately, contribute to improving patients' care.

B2 Methods

Persons with Chronic Impairment due to Stroke

One-hundred and eleven (111) community dwelling volunteers who had suffered a stroke trained for 18 hours with the InMotion2 robot (Interactive Motion Technologies, Cambridge, MA). Subjects were trained in point-to-point movements which evoked significant improvement (as measured by clinical scales) by the end of the therapy[11]. The protocol included 5 evaluation sessions, three before treatment and two more at mid-point, and discharge. Pre-treatment evaluation sessions took place prior to admission with their average serving as the admission score and ensuring the patient's condition was stable.

Inclusion criteria were: 1) diagnosis of a single, unilateral stroke at least 6 months prior to enrollment verified by brain imaging; 2) sufficient cognitive and language abilities to understand and follow instructions (Mini-Mental Status Score of 22 and higher or interview for aphasic subjects); and 3) stroke-related impairments in muscle strength of the affected shoulder and

elbow between grades ≥1/5 and ≤3/5 on the Motor Power scale (MP)[19-20]. Subjects were excluded from the study if they had a fixed contraction deformity in the affected limb, and also if they demonstrated improvement over three measurements made during the four week observation period prior to treatment. None of the subjects were engaged in conventional occupational or physical therapy programs or received pharmacological management of spasticity and tone (i.e., Botox) during the experimental trial. All subjects volunteered for the study and gave their informed consent.

Clinical measures for the Upper Extremity

The FMA, MSS, the MP, and the Modified Ashworth Scale (MAS) were used to assess patients' abilities during the evaluation sessions. These scales have established reliability and validity as well as significant limitations, as described below.

The FMA has 5 evaluation domains (including sensory function, balance, and joint range of motion)[21-23]. In this study we only used the upper limb section of the FMA. Based on Twitchell[24] and Brunnstrom's[25] levels of motor recovery after stroke, such section can be used to assess synergistic and voluntary motor abilities in about 30 minutes. A three-point scale is used to measure performance (0 = unable, 1 = partial, 2 = performs fully) on 33 test items (total possible score = 66 points). The FMA is able to detect changes in persons with severe to moderate motor impairments after stroke, in part because of its inclusion of isolated joint movement rather than a sole emphasis on task-related actions. Reported disadvantages of the FMA include a potential ceiling effect for higher-functioning patients and its limited number of test items to evaluate distal, fine motor function[23]. Our protocol included patients in the moderate to severe range, so that the ceiling effect would not affect our results.

The MSS was developed at Burke Rehabilitation Hospital due the perceived pitfalls of relying on the upper limb section of the FMA for sub-acute stroke patients[26]. The upper limb section of the FMA suffers from a decreased sensitivity since return of reflex and synergistic movements (a substantial component of the total score) often occur before admission and evaluation at the rehabilitation hospital. Instead, the MSS uses an end-of-scale value of 82, with a potential range

of 40 points for isolated shoulder and elbow movements. Thus the MSS aims at augmenting the FMA by further specifying the quality of voluntary movement in the hemiparetic upper limb. The MSS elbow and shoulder section consists of a sum of scores (0 to 2) given to 10 isolated shoulder movements and 4 elbow/forearm movements. The MSS wrist and fingers section consists of a sum of grades for 3 isolated wrist movements and 12 hand movements[26]. To be an effective augmentation of the FMA, the MSS must preserve a linear relationship with the FMA. Results of a study with 56 sub-acute patients evaluated by the same "blinded" therapist showed that indeed the relationship between FMA and MSS was linear and that the MSS had good inter-rater as well as intra-rater reliability[26].

The Medical Research Council test of MP was used to assess strength. The MP measures strength in isolated muscle groups of the involved shoulder and elbow on an ordinal scale (scale range: 0, no muscle contraction; 5, normal strength)[19-20].

The MAS was used to measure hypertonia and it rates the resistance to passive stretch in 14 different muscle groups of the upper limb[27]. It is an ordinal scale ([0, 1, 1+, 2, 3, 4] or [0, 1, 2, 3, 4, 5]). Evaluations are conducted by moving a limb about a joint at different speeds, and by noting the muscular response throughout that limb range of motion (i.e., both speed and position dependent).

Kinematic Measures for the Upper Extremity

In this paper we will report on metrics obtained from three distinct sets of measurements: unconstrained reaching movement, unconstrained circle drawing, and shoulder strength.
The unconstrained reaching movement required the patient to perform unconstrained movement towards targets presented in 8 positions equally spaced around a 14cm radius circle and back to the center. Targets were presented in clockwise order similar to a robot-assisted therapy session. If the patient was unable to hit a target, the therapist cued the robot to stop recording and the patient's hand was moved to the target where recording of patient's movement proceeded. A total of 80 movements were performed for each evaluation session. The following macro-metrics were extracted from the data: the deviation from the straight line connecting the targets, aiming,

movement mean and peak speed, movement smoothness (ratio of mean to peak speed), and movement duration. Movement speed profiles were decomposed into support-bounded lognormal submovements as described in[17]. The following micro-metrics were derived from submovement decompositions: number of submovements, submovement duration, overlap, peak, inter-peak interval, and shape metrics mu (skewness or asymmetry) and sigma (kurtosis or "fatness"). The rationale for these micro-metrics was based on a century-old conjecture that human arm movement is controlled discretely, by combining elementary units of movements or submovements[16].

During the unconstrained circle drawing, the patient's hand was initially positioned at 3 o'clock and at 9 o'clock (right or left to the workspace center). Patients were asked to draw clockwise and counterclockwise circles starting and ending at the same point. This task, which was not trained during therapy, required the coordination of shoulder and elbow joint movements. A total of 20 movements were performed for each evaluation session. The following macro-metrics were extracted from the data as described in[18]: the axes ratio (ratio of the minor to major axes of the best-fitting ellipse) and the joint angle correlation (degree of independence of the shoulder and elbow movements).

Kinetic Measures for the Upper Extremity

Shoulder extension/flexion and abduction/adduction measurements take advantage of the fact that the MIT-Manus is a SCARA type device (Selective Compliance Assembly Robot Arm) which is highly compliant in the horizontal plane and has very low compliance on the vertical plane (almost infinite impedance). This affords the unique potential of easily testing the shoulder during flexion/extension and abduction/adduction. The patient's arm was pre-positioned at 90° of shoulder flexion/extension in the sagittal plane with elbow fully extended. The hand was supported in a plastic trough at the robot's tip with no support provided at the elbow. Once the patient was secured in the trough, the therapist manually stabilized the robot's arm in the required testing position. The patient was then instructed to attempt to lift and push-down his/her arm five consecutive times. During abduction/adduction testing, the patient was rotated in the chair 90° to left or right depending on the side of impairment and his/her arm was pre-positioned in 90°

abduction (Figure B1). The elbow position and support procedure was the same as during flexion/extension. Once the arm was secured, the patient was instructed to lift and push-down the arm five times. A total of 20 attempts to lift or push-down the arm were completed for each evaluation session. Mean shoulder strength (Z-Force) for flexion, extension, abduction, and adduction were calculated from the data[28].

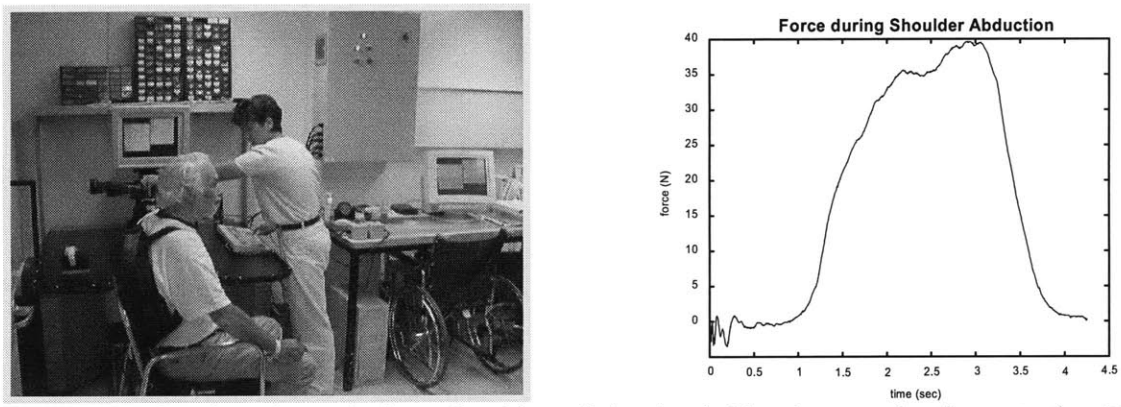

Figure B1. Stroke inpatient during shoulder abduction/adduction evaluation at the Burke Rehabilitation Hospital. The patient was asked to lift the hemiparetic arm to the best of his abilities.

Statistical Analysis

Least squares error multiple regression linear models were constructed in an attempt to estimate the FMA, the MSS, the MAS, and the MP from robot kinematic and kinetic metrics. Model performance was measured by the correlation between the therapist assigned and model calculated scores. Five types of models were investigated.

The first model calculated the FMA, MSS, MAS, and MP from all the kinematic and kinetic metrics. For the second model, prior to performing multiple regressions, a principal component analysis (PCA) was conducted on all kinematic and kinetic metrics in an attempt to reduce the total number of metrics. Fewer metrics would reduce the model complexity and perhaps the number of tasks performed by the patient, thereby reducing the overall time required for patient evaluation. Since the metrics had different units, the PCA was applied to normalized kinematic and kinetic metrics. Normalization scaled the data, so that each metric had zero mean and standard deviation of 1.

Three additional models containing different combinations of the robot metrics were constructed: kinematic macro-metrics and kinematic macro- and micro-metrics (submovements) for the FMA, MSS, and MAS, and force metrics for the MP.

All models were developed by randomly separating 75% of the data to train the model with the remaining 25% set aside for model validation. A Kruskal-Wallis test on the clinical scores confirmed that the training and validation data sets were not significantly different.

Correlations among the clinical scales were also investigated in order to identify dependent scales. A strong correlation between two or more clinical scales would indicate measurement redundancy, meaning it may be possible to eliminate one, thus reducing the amount of time required for patient evaluation.

B3 Results

Correlation Among Clinical Scales

Table B1 shows the correlation among clinical scales.

	FMA	MSS	MP	MAS
FMA	1	0.948	0.785	-0.23
MSS	0.948	1	0.774	-0.213
MP	0.785	0.774	1	-0.013
MAS	-0.23	-0.213	-0.013	1

Table B1. Correlation of clinical scores for chronic stroke patients (R-values)

Correlation among FMA and MSS was strong, suggesting redundancy for this population of chronic stroke patients. This was not entirely surprising since the MSS was designed to be a finer grading scale of the upper extremity impairment than the FMA for sub-acute patients. This result is consistent with and extends the results of previous studies for sub-acute stroke (Ferraro[26], 12 patients, $R = 0.981$, $p < 0.0001$ and Krebs[28], 56 patients, $R = 0.981$, $p < 0.0001$).

The correlation among the ability to move isolated joint movement (FMA and MSS) and strength (MP) was moderate suggesting a common trait. As patients improve the scales demonstrate such an improvement. In contrast, the correlation between MAS and the other scales was very low. If we assume that recovery can be characterized by improvement in the ability to move isolated joints and increased joint strength, then the observed low correlation suggests that tone might not be an important marker of recovery for this population.

Estimating FMA, MSS, MP, and MAS from Kinematic and Kinetic Metrics

Training and validation results of the kinematic and kinetic model to estimate the FMA, MSS, MP, and MAS are shown in Table B2. We employed all the kinematic and kinetic metrics to build such models. The residual plots did not have any significant correlations or patterns, indicating no underlying trends missed in the data and the appropriateness of our linear model.

	Training	Validation
FMA	0.802	0.427
MSS	0.788	0.696
MP	0.797	0.449
MAS	0.428	0.171

Table B2. R values for linear fit between measured and scores calculated with all (kinematic and kinetic) metrics

If there was a strong alignment of the robot-based metrics, the PCA would significantly reduce the number of metrics required to the estimation. The PCA did not reveal any significant redundancy on these kinematic and kinetic metrics and only reduced the original 20 metrics marginally to 17 variables for the FMA and 16 variables for the MSS, MP, and MAS. The residual plots did not have any significant correlations or patterns.

Calculating FMA, MSS, and MAS from Kinematic Metrics

The FMA and MSS evaluate motor impairment including isolated and synergistic movements. Therefore, the kinematic macro-metrics extracted from the unconstrained reaching movements

(point-to-point) and the circle drawing task (independent joint movement) were selected to develop a model. In addition, the benefits from including micro-metrics based on submovements in the model were explored.

Table B3 shows the training and validation results for the model. As with the previous models, no significant correlations or patterns were found in the residual plots. For the breakdown of the eight kinematic macro-metrics and seven kinematic micro-metrics (submovements) the training data performed better, namely the macro- and micro-metrics model yielded to the highest R values. But for the validation data, the opposite was true – the model based on the kinematic macro-metrics alone had larger R, indicating that this model generalized better to the data. In fact, it outperformed the model that included all the 20 robot-based metrics for the validation data (both kinematic and kinetic, see Table B2). The FMA showed the highest R values for the training data, but only moderate R values for the validation data. The MSS performance remained remarkably consistent between training and validation data (small difference among the correlation values). Neither the macro- nor the micro-metric model was able to produce more than a weak correlation for the MAS score.

For all three scales, including the micro-metrics based on submovements into the model (see validation data) produced no additional benefit.

	Training		Validation	
	Macro-metrics	Macro- and micro-metrics	Macro-metrics	Macro- and micro-metrics
FMA	0.740	0.779	0.425	0.410
MSS	0.711	0.772	0.721	0.688
MAS	0.357	0.399	0.158	0.137

Table B3. R values for linear fit between measured scores and scores calculated with kinematic metrics.

Since this model was the most concise and outperformed the others, the macro-metric model is reported for the FMA and MSS:

$$FMA = -4.58 - 11.63*[Aim] + 37.04*[Deviation] - 29.30*[MeanSpeed] + 62.55*[PeakSpeed] + 83.96*[Smoothness] + 1.72*[Duration] + 2.98*[EllipseRatio] - 17.28*[Joint\ Ind.]$$

$$MSS = -29.64 - 2.96*[Aim] - 16.12*[Deviation] - 230.22*[MeanSpeed] + 161.99*[PeakSpeed] + 184.74*[Smoothness] + 3.36*[Duration] - 16.55*[EllipseRatio] - 35.85*[Joint\ Ind.]$$

The average values and standard deviations of each metric for the 111 person with chronic stroke and the product of the average value with the model coefficients are shown in Table B4. This product indicates which metrics have the largest weights.

	Aim (rad)	Deviation (m)	Mean Speed (m/s)	Peak Speed (m/s)	Smoothness	Duration (s)	Ellipse	Joint Independence
Average	1.02	0.05	0.05	0.15	0.36	4.18	0.58	0.58
StDev	0.23	0.01	0.02	0.05	0.08	2.43	0.18	0.19
FMA model coefficient* Average (unitless)	11.85	1.75	1.55	9.32	30.22	7.20	1.72	9.99
MSS model coefficient* Average (unitless)	3.02	0.76	12.14	24.15	66.49	14.05	9.54	20.72

Table B4. Average, standard deviation, and model coefficient products (unitless) for the macro-metrics.

Calculating MP from Kinetic Metrics

Since the MP evaluates strength at each joint, the Z-force metrics were selected to develop a model. In contrast to the models for FMA, MSS, and MAS described above, this model was applied to logarithmic data. The logarithmic scale was introduced to account for Weber's law, which explains how actual forces (the Z-force measured by the robot force transducer) are perceived by humans (the MP score recorded by the therapist). According to Weber's Law the smallest perceivable difference in weight, p (the least difference that the test person can still perceive as a difference), is proportional to the starting value of the weight:

$$p = k \ln \frac{S}{S_o}$$

Where S is the stimulus weight, S_o is the stimulus threshold, and k is a proportionality constant. This model was similar to the model proposed by Krebs et al.[28] for calculating MP from shoulder

strength in sub-acute stroke patients. Our model yielded R equal to 0.580 for training and 0.520 for validation. The residual plots did not have any significant correlations or patterns.

The MP-force metrics model is reported below.

$$MP = 3.92 - 2.87 * \ln(\text{ZFlexion}) - 0.60 * \ln(\text{ZExtension}) - 1.09 * \ln(\text{ZAbduction}) - 1.84 * \ln(\text{ZAdduction}) + 12.52 * \ln(\text{Z})$$

Or in $\log_{10}$ basis:

$$MP = 3.92 - 6.60 * \log(\text{ZFlexion}) - 1.38 * \log(\text{ZExtension}) - 2.51 * \log(\text{ZAbduction}) - 4.23 * \log(\text{ZAdduction}) + 28.84 * \log(\text{Z})$$

B4 Discussion

First proposed over a decade ago, devices for robot-aided neuro-rehabilitation are increasingly being incorporated into stroke patients' care programs. In addition to delivering high intensity, reproducible sensorimotor therapy, these devices are precise and reliable "measuring" tools that can be expanded with multiple sensors to record simultaneously kinematic and force data. These measurements are objective and repeatable and can be used to provide patients and therapists with immediate measures of motor performance. Reducing the time to evaluate improvement or deterioration may offer new opportunities for designing therapeutic programs and ultimately for increasing the efficiency of patients' care.

Across multiple regression models, we demonstrate that the FMA always performed the best in training, but the validation performance decreased. Correlations were higher than those reported by the study of Colombo et al.[29], which used simple regression models to calculate the FMA (R=0.53-0.55). The MSS performed the most consistently between training and validation, with training correlations similar to the FMA. The strong correlation between the MSS and the FMA suggests that estimation of the MSS would allow for estimation of the FMA as well. In contrast to the positive results for the FMA and MSS, the MAS produced only weak non-significant correlations between the actual and calculated MAS scores and with the other scales. Tone and the variability of tone suggest that different clinical metrics should be developed to calculate this scale, a result supported by other clinical work[30-31].

The extent to which micro-metrics based on submovements improved models' performance was also investigated. Submovement extraction can be a tedious, slow, computer intensive task. In the past we employed two different strategies to extract submovements from patients' movement data: a global[32] or a local minimization scheme[2]. The efficiency of a global algorithm such as branch-and-bound is $O(N^M)$, where M is the number of submovements. A greedy algorithm such as ISRBF (Irregular Sampling Radial Basis Function) [2], is far more efficient under this definition O(MN), but contrary to the branch-and-bound algorithm, ending close to a global minimum is not guaranteed. In this study we found that the models that included submovement metrics performed only slightly better than those that did not (for example compare performance of the macro-metric models with those of the macro- and micro-metric models). Since the impact of submovements was found to be low, the greedy-type algorithm may be employed for extracting submovements. Although limited by local minima, it would reduce the computation from hours to seconds and allow online computation. The low impact may also allow for the submovement metrics to be eliminated entirely from the model.

The MP-force metrics model yielded relatively low correlation values, with R=0.580 and R=0.520 for training and validation respectively. Using a similar model, Krebs et al.[28] found a correlation of 0.853 between the MP score and the $\log_{10}$ of the Z-Force metric. In contrast to our study that investigated chronic stroke subjects evaluated by 3 different evaluators, the study by Krebs et al. investigated subjects in the sub-acute phase of recovery evaluated by the same therapist, which may account for the differences in results. While our model achieved only a moderate correlation, it should be pointed out that the slope of the curves obtained in both models Krebs and our model are quite similar giving additional credence to the proposed model to estimate the MP.

Of all the models investigated in this study, the kinematic macro-metric model for MSS appeared to offer the best trade-off between performance and complexity and strong, similar correlation values for training (R=0.711) and validation (R=0.721). Table 4 shows that the smoothness, peak speed, and joint independence metrics weighted the most in this model. These metrics may represent a significant first step towards the development of unified, real-time, automated measures of therapy outcome.

Robot measurements can potentially outperform human-administered clinical scales and are only limited by the performance of the robot sensors. For example, MIT-Manus can measure positions with a resolution of 0.1 mm. The reliability of human-administered clinical scales has often been questioned; for example, Sanford et al.[33] reported an inter-rater variability of +/- 18 points on a 95% confidence interval for the total FMA scale, pointing out that small patient improvements will not be able to be identified by the score. Krebs et al.[28] found up to a 15% discrepancy between therapists when evaluating the same patient for the upper extremity FMA scale. Gregson et al.[19] estimated an inter-rater agreement of 59% for the MAS. The MAS is considered a reliable clinical scale by some[19], but totally unreliable by others[34]. Besides having questionable reliability, human-administered clinical scales are also time-consuming. In contrast, robot measurements can potentially provide therapists and patients with immediate feedback. Real-time scoring can not only greatly reduce the amount of time required for evaluations of patients' motor improvements, but it is also becoming a key need for the new robot-aided neuro-rehabilitation scenarios. These include systems that continuously adapt the amount and type of delivered therapy based on patient's motor abilities[35-36].

Despite their potential advantages, robot measurements are not so well established as human-administered clinical scales, which are still the "gold standard" for measuring outcomes. This study proposes a tentative beginning for a unified set of metrics for outcome measurement. We demonstrate the feasibility of developing models to calculate the well-established clinical scales FMA, MSS, and MP from the robot-derived metrics. The ideal model would have as few, easy-to-calculate metrics as possible (to reduce the evaluation time) while maintaining good training and validation model performance.

B5 Investigating Shoulder/Elbow Score of the Fugl-Meyer Assessment

Because the Manus only provides therapy for the shoulder and elbow, the breakdown of the Fugl-Meyer upper extremity (max score = 66) was separated into a shoulder/elbow score (max score = 42) and a wrist/hand score (max score = 24). Currently, only the 48 Spaulding Rehabilitation Center patients FMA upper extremity scores were separated in this manner. The hypothesis is that the Manus metrics may provide a better estimate of the shoulder/elbow score

because those parts of the upper limb are receiving the therapy. A linear regression was completed for both the shoulder/elbow and wrist/hand data. The data was separated into training and test sets based on the previous analysis for comparison. Three sets of metrics were analyzed and their metrics are listed in Table B5:

AD = Admission and Discharge

AID = Admission, Interim, and Discharge

AIDF = Admission, Interim, Discharge, and Follow-Up

AD Metrics		AID Metrics	AIDF Metrics
Aim	Ellipse	Aim	Aim
Mean Speed	Joint Independence	Deviation	Deviation
Peak Speed	No. of Submovements	Mean Speed	Mean Speed
Mean Peak	Submovement Duration	Peak Speed	Peak Speed
Duration	Submovement Overlap	Mean Peak	Mean Peak
Z Flexion	Submovement Amplitude	Duration	Z Flexion
Z Extension	Sigma	Z Flexion	Z Extension
Z Abduction		Z Extension	Z Abduction
Z Adduction		Z Abduction	Z Adduction
Z		Z Adduction	Z
		Z	

Table B5. Manus metrics available for each patient evaluation time.

The AD metrics were chosen based on the previous principle component analysis. The AID and AIDF metrics were the only metrics available for all measurement times. Tables B6 and B7 show the results from the linear regression for all three sites and for only Spaulding, respectively.

	AD	AID
Training	0.783	0.734
Test	0.503	0.377

Table B6. Linear regression results for the total FMA score for all three centers.

	AD	AID
Training	0.734	0.857
Test	0.709	0.614

Table B7. Linear regression results for the total FMA score for Spaulding patients only.

Table B8 lists the results for the FMA score breakdown. For the training and test sets, the Shoulder/Elbow score was predicted with the largest linear correlation R for the AD and AID data sets. For the AD, AID, and AIDF data sets, the Shoulder/Elbow score was predicted with larger R compared to the prediction of the Wrist/Hand score. Compared to the full data set, the Spaulding group had lower R values for the AD and AID FMA prediction for training, but higher for test. It would be useful to obtain the FMA score breakdown data for the Baltimore and Burke patients and complete a full analysis.

	AD Shoulder/Elbow	AD Wrist/Hand	AID Shoulder/Elbow	AID Wrist/Hand	AIDF Shoulder/Elbow	AIDF Wrist/Hand
Training	0.829	0.774	0.743	0.612	0.672	0.538
Test	0.481	0.489	0.410	0.412	0.512	0.246

Table B8. Linear regression results for the shoulder/elbow and wrist/hand FMA score breakdown for Spaulding patients.

B6 Principle Component Analysis

Principle component analysis (PCA) is a multivariate choice method used when it is desired to reduce the number of variables [37]. The independent variables with the most variability are assumed to explain more of the variability in the dependent variable.

Often, the variables chosen for an analysis are measured in different units and therefore are not additive, as is with the different robot metrics. Therefore, it is necessary to convert them to standard comparable units.

Original observation

Mean of series

$$x_{ij} = \frac{(X_{ij} - X_m)}{\sigma}$$

Scale-free observation

Standard deviation of series

The transformed series is now scale free with a mean of zero and a standard deviation of one. Once the data is standardized, in order to conduct a PCA, the weights given to the variables must maximize the sum of squares of the correlation matrix.

Calculating the Variable Weights (when data has been standardized) [37]:

Step 1 – Find simple correlation coefficients of all variable combinations.

Correlation Table of the set of K Variables					
	X_1	X_2	X_3	X_k	$\Sigma^k_i r_{xi\,xj}$
X_1	$r_{x1\,x1}$	$r_{x1\,x2}$	..	$r_{x1\,xk}$	$\Sigma^k_i r_{x1\,xi}$
X_2	$r_{x2\,x1}$	$r_{x2\,x2}$	..	$r_{x2\,xk}$	
"	..	..	..	..	
"	..	..	..	..	
X_k	..	..	..	..	
"	$r_{xk\,x1}$	..	..	$r_{xk\,xk}$	
$\Sigma^k_i r_{x1\,xj}$	$\Sigma^k_i r_{xi\,x1}$	$\Sigma^k_i r_{xi\,x2}$	$\Sigma^k_i r_{xi\,x3}$	$\Sigma^k_i r_{xi\,xk}$	$\Sigma^k_i \Sigma^k_i r_{xi\,xj}$

The correlation matrix is symmetrical with 1's on the main diagonal (self correlation of unity).

Step 2 – Sum each column (or row) of the correlation table. For k independent variables, you will calculate k sums.

Step 3 – Compute the sum total of the column (or row) sums and take its square root (composite index).

Step 4 – Factor loading is obtained by:

$$a_{ij} = \frac{\sum_{i}^{k} r_{x_i x_j}}{\sqrt{\sum_{i}^{k}\sum_{j}^{k} r_{x_i x_j}}}$$

Step 5 – $P_1 = a_{11}x_1 + a_{12}x_2 + \ldots + a_{1k}x_k$

P_1 is the first principle component. The independent variables with the largest (in magnitude) loading factors have the largest variability. These variables should be retained during the reduction.

$$l_z = \sum_j^k a_{zj}^2$$

$$\frac{l_z}{k} = \text{ percent variation explained by } P_z$$

$$(\text{note: } \sum_i^k l_i = k)$$

Step 6 – The sum of squares of the loading of the principle component is called the latent root (or eigenvalue).

The common rule of thumb is to include principle components with a total sum of between 80-90% of the variance explained.

Note: the Matlab command to complete these steps is: [coefs]= princomp(zscore(dataset));

Where, "zscore" standardizes the variable data and "princomp" will calculate the factor loadings (coefs) for the variables based on correlations. Without the "zscore" command, "princomp" automatically centers each column of variables, but does NOT rescale them.

Appendix B References

1. American Stroke Association. [Online] http://www.strokeassociation.org. Accessed September 2008.

2. Prange, GB, Jannink, MJA, Groothuis-Oudshoorn, CGM, Hermens, HJ, IJzerman, MJ. Systematic review of the effect of robot-aided therapy on recovery of the hemiparetic arm after stroke. *Journal of Rehabilitation Research & Development*. 2006;43:171–184.

3. Kwakkel, G, Kollen, BJ, Krebs, HI. Effects of robot-assisted therapy on upper limb recovery after stroke: a systematic review," *Neurorehabilitation and Neural Repair* (In press).

4. Mehrholz J, Werner C, Kugler J, Pohl M. Electromechanical-assisted training for walking after stroke. *Cochrane Database Syst Rev 2007*.

5. Krebs HI, Hogan N, Aisen ML, Volpe BT. Robot-aided neuro-rehabilitation. *IEEE Trans Rehab Eng*. 1998;6:75-87.

6. Aisen, ML, Krebs, HI, McDowell, F, Hogan, N, Volpe, BT. The effect of robot assisted therapy and rehabilitative training on motor recovery following a stroke. *Arch of Neurol*. 1997;54:443-446.

7. Krebs, HI, Volpe, BT, Aisen, ML, Hogan, N. Increasing productivity and quality of care: robot-aided neurorehabilitation. *VA Journal of Rehabil Res and Dev*. 2000;37:639-652.

8. Volpe, BT, Krebs, HI, Hogan, N, Edelstein, L, Diels, CM, Aisen, ML. Robot training enhanced motor outcome in patients with stroke maintained over 3 years. *Neurology*. 1999;53:1874-1876.

9. Volpe, BT, Krebs, HI, Hogan, N, Edelstein, L, Diels, CM, Aisen, M. A novel approach to stroke rehabilitation: robot aided sensorymotor stimulation", *Neurology*. 2000;54:1938-1944.

10. Volpe, BT, Krebs, HI, Hogan, N. Is robot-aided sensorimotor training in stroke rehabilitation a realistic option? *Current Opinion in Neurology, Lippincott Williams & Wilkins*. 2001;14:745-52.

11. Ferraro, M, Palazzolo, JJ, Krol, J, Krebs, HI, Hogan, N, Volpe, BT. Robot aided sensorimotor arm training improves outcome in patients with chronic stroke. *Neurology*. 2003;61:1604-1607.

12. Fasoli SE, Krebs HI, Stein J, Frontera WR, Hogan N. Effects of robotic therapy on motor impairment and recovery in chronic stroke. *Arch Phys Med Rehabil*. 2003;84:477-482.

13. Fasoli SE, Krebs HI, Stein J, Frontera WR, Hughes R, Hogan N. Robotic therapy for chronic motor impairments after stroke: follow-up results. *Arch Phys Med* Rehabil. 2004;85:1106-11.

14. Stein J, Krebs HI, Frontera WR, Fasoli SE, Hughes R, Hogan N. Comparison of two techniques of robot-aided upper limb exercise training after stroke. *Am J Phys Med Rehabil.* 2004;83:720-728.

15. Daly JJ, Hogan N, Perepezko EM, Krebs HI, Rogers JM, Goyal KS, Dohring ME, Fredrickson E, Nethery J, Ruff RL. Response to upper-limb robotics and functional neuromuscular stimulation following stroke. *J Rehabil Res Dev.* 2005;42:723-736.

16. Krebs HI, Aisen ML, Volpe BT, Hogan N. Quantization of continuous arm movements in humans with brain injury. *Proc Natl Acad Sci U S A.* 1999;96:4645-4649.

17. Rohrer B, Fasoli S, Krebs HI, Hughes R, Volpe B, Frontera WR, Stein J, Hogan N. Movement smoothness changes during stroke recovery. *J Neurosci.* 2002;22:8297-8304.

18. Dipietro L, Krebs HI, Fasoli SE, Volpe BT, Stein J, Bever C, Hogan N. Changing motor synergies in chronic stroke. *J Neurophysiol.* 2007;98:757-768.

19. Gregson JM, Leathley MJ, Moore AP, Smith TL, Sharma AK, and Watkins CL. Reliability of measurements of muscle tone and muscle power in stroke patients. *Age Ageing.* 2000;29:223-228.

20. Medical Research Council/Guarantors of Brain. Aids to the examination of the peripheral nervous system. London: Bailliere Tindall, 1986.

21. Fugl-Meyer AR, Jaasko L, Leyman I, Olsson S, and Steglind S. The post stroke hemiplegic patient. A method for evaluation of physical performance. *Scandinavian Journal of Rehabilitation Medicine.* 1975;7:13-31.

22. Duncan, PW, Propst M, and Nelson SG. Reliability of the Fugl-Meyer assessment of sensorimotor recovery following cerebrovascular accident. *Physical Therapy.* 1983;63:1606-1610.

23. Gladstone DJ, Danells CJ, Black SE. The Fugl-Meyer assessment of motor recovery and stroke: a critical review of its measurement properties. *Neurorehabilitation & Neural Repair.* 2002;16:232-240.

24. Twitchell, TE. The restoration of motor function following hemiplegia in man. *Brain.* 1951;74:443-480.

25. Brunnstrom, S. *Movement therapy in hemiplegia.* New York: Harper & Row. 1970.

26. Ferraro M, Demaio JH, Krol J, Trudell C, Rannekleiv K, Edelstein L, Christos P, Aisen M, England J, Fasoli S, Krebs HI, Hogan N, Volpe BT. Assessing the motor status score: a scale for the evaluation of upper limb motor outcomes in patients after stroke. *Neurorehabil Neural Repair.* 2002;16:283-289.

27. Bohannon, RW, Smith, MD. Interrater reliability of a modified Ashworth scale of muscle spasticity. *Phys Ther.* 1987;67:206-207.

28. Krebs, HI, Volpe, BT, Ferraro, M, Fasoli, S, Palazzolo, JJ, Rohrer, B, Edelstein, Hogan, N. Robot-aided neurorehabilitation: from evidence-based to science-based rehabilitation. *Top Stroke Rehabil.* 2002;8:54-70.

29. Colombo, R, Pisano, F, Micera, S, Mazzone, A, Delconte, C, Carrozza, MC, Dario, P, Minuco, G. Robotic techniques for upper limb evaluation and rehabilitation of stroke patients. *IEEE Trans Neural Syst Rehabil Eng* .2005;13:311-324.

30. Sommerfeld DK, Eek EU, Svensson AK, Holmqvist LW, von Arbin MH. Spasticity after stroke: its occurrence and association with motor impairments and activity limitations. *Stroke.* 2004;35:134-139.

31. Landau WM. Spasticity after stroke: why bother? *Stroke.* 2004;35:1787-1788.

32. Rohrer B, Hogan N. Avoiding spurious submovement decompositions: a globally optimal algorithm. *Biol Cybern.* 2003;89:190-199.

33. Sanford, J, Moreland, J, Swanson, L, Stratford, P, Gowland, C. Reliability of the Fugl-Meyer assessment for testing motor performance in patients following stroke. Physical Therapy. 1993;73:447-454.

34. Pomeroy, V, Dean, D, Sykes, L, Faragher, B, Yates, M, Tyrrel, PJ, Moss, S, Tallis, RC. The unreliability of clinical measures of muscle tone: implications for stroke therapy. *Age and Ageing.* 2000;29:229-233.

35. Krebs, HI, Palazzolo, JJ, Dipietro, L, Ferraro, M, Krol, J, Rannekleiv, K, Volpe, BT, Hogan, N, Rehabilitation robotics: performance-based progressive robot-assisted therapy. *Autonomous Robots.* 2003;15:7-20.

36. Dipietro L, Ferraro M, Palazzolo JJ, Krebs HI, Volpe BT, Hogan N. Customized interactive robotic treatment for stroke: EMG-triggered therapy. *IEEE Trans Neural Syst Rehabil Eng.* 2005;13:325-334.

37. Principle Component Analysis [Online] http://www.mit.gov.in/download/ANNEX.PDF. Accessed November 2008.

Appendix C: MRI-Compatible Wrist Robot: Seal Redesign and Phantom Testing

In an effort to study brain plasticity, the ability of the brain to reorganize itself after an injury, doctors want to image the brain during rehabilitation. One common imaging method is fMRI, and in order for a device to be implemented in this environment it must not contain any ferrous metals, distort the fMRI signal, and fit within the restricted space of a full-body fMRI.

This Appendix details work completed to source and greatly reduce the internal leakage of a previously designed hydraulic vane motor, testing of the internal leakage and rotary friction after seal design changes, and phantom testing to validate material selection. For more extensive background information of the design development of this device, please see the theses of Mendelowitz [1] and Hanumara [2].

C1 Internal Leakage Troubleshooting

The current vane motor design had eliminated all outside, or external leakage, but a significant amount of internal leakage, or leakage inside the motor between the vane, stop, and inside surface remained. Greatly reducing this internal leakage is very important in order to be able to accurately control the device. If fluid is able to leak around the vane while either the outside pumps are driving or the patient is turning the motor, the torque will not be transmitted and there will not be a clear relationship between the angle of shaft rotation and the volume of fluid displaced. While addressing this problem, the relationship between the seals and the rotary friction must be considered. If thick, stiff seals are implemented to reduce the leakage, the force required to turn the motor will be increased. In order for the patients to have as natural a motion as possible and be able to backdrive the device, the rotary friction needs to be kept at a minimum. Maintaining a balance between the seals and rotary friction will be a key to improving this device.

The first step taken to identify the source(s) of internal leakage was to create a "window" to the problem. Figure C1 shows a copy of the original anodized aluminum cover made with clear Lexan.

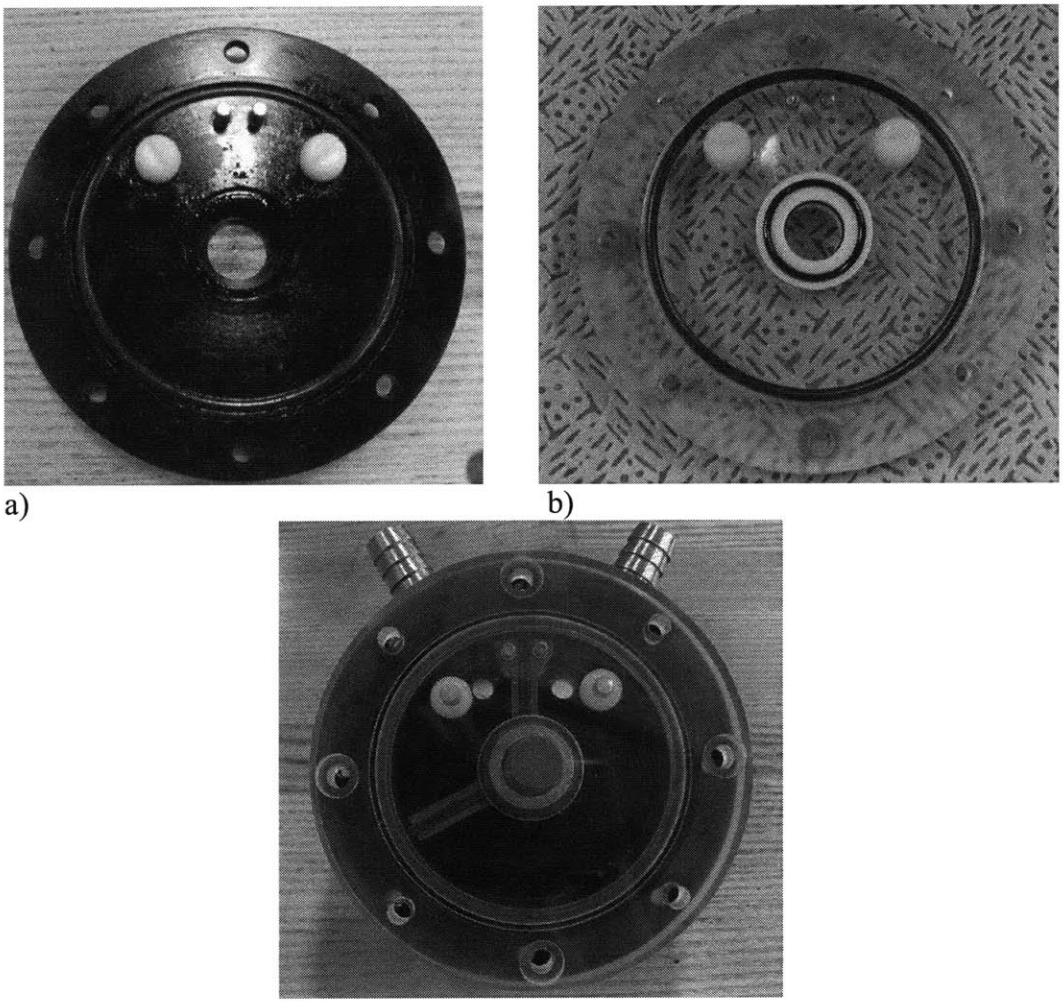

Figure C1. a) original aluminum cover, b) Lexan cover, c) rotary motor with Lexan cover.

The same test setup was used to identify leakage problem areas and the average internal leakage rate. The procedure followed set the vane of the motor to the six o'clock position, a tube was attached to the left motor inlet and connected to an adjustable pressure vessel with the same liquid, and a second tube was attached to the right outlet and emptied to a graduated beaker (Figure C2).

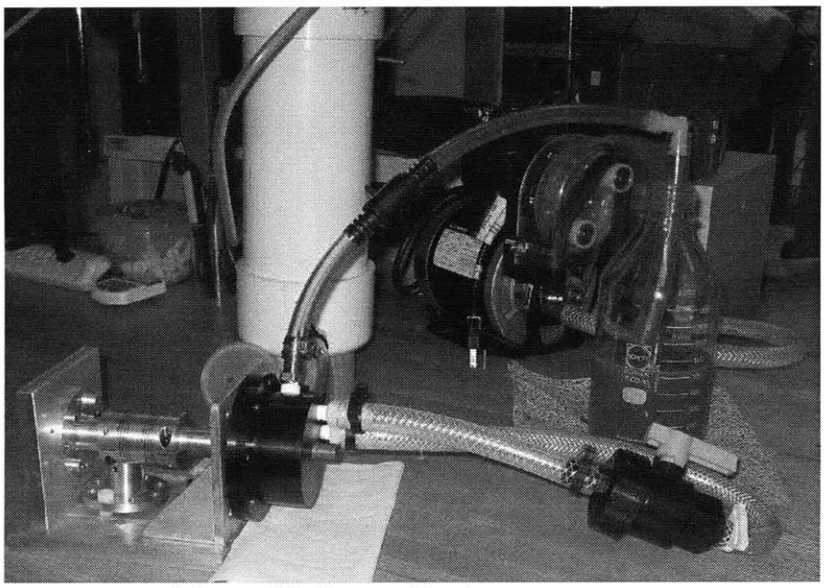

Figure C2. Internal leakage test setup

To check for areas of internal leakage the left side filled with fluid that was one part filtered water to one part antifreeze. The pressure at the inlet was slowly increased until streams of liquid could be seen flowing from the left side of the motor to the empty right side.

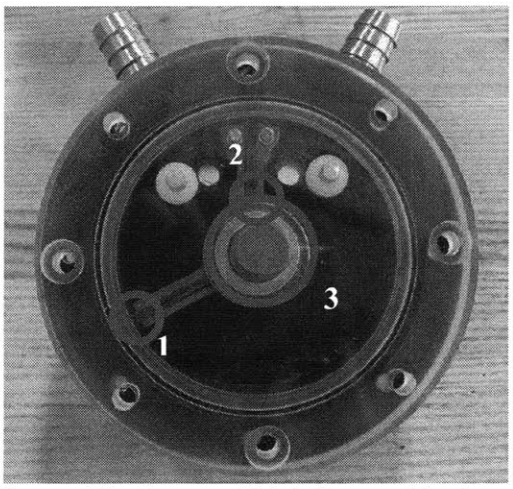

Figure C3. Areas of high internal leakage

Figure C3 shows the areas where the most fluid flow was observed. The intersections of the vane with the side of the motor and the stop with the shaft of the vane (shown as Areas 1 and 2) were expected sources because they were areas with seals intersecting at sharp corners. In contrast, the face seal between the vane shaft and the cover (Area 3) was not predicted and based on visual observation, this source had higher leakage rates than the other two areas.

The average leakage rate was determined by completely de-airing and filling both sides of the motor with fluid and measuring the amount of time required to fill the beaker 900 mL with a stopwatch. This was completed for pressures ranging from about 3 – 30 psi (0.02 – 0.2 MPa) and converted into a volumetric flow rate. This testing method is detailed in [2].

Before any redesign was completed, the internal leakage rate ranged from 0.78 in^3/sec at about 3 psi to 3.83 in^3/sec at about 30 psi, which equated to filling the 900 mL beaker in about 3 seconds. Calculating the maximum pressure that may occur across the vane:

$$P = \frac{2T}{L(R^2 - r^2)} \quad \text{(eq. C-1)}$$

Where T is the input torque, P is the resulting pressure, R is the bore radius of the motor (1.25 inches), r is the shaft radius (0.25 inches), and L is the vane height (1 inch). The motor must deliver at least 10.62 in-lb (1.2 Nm), and with a factor of safety of 2, the input torque will be 21.24 in-lb. The maximum resulting pressure is 32.4 psi (0.22 MPa). The motor seals must be able to withstand pressures in this range with minimum internal leakage and of course no external leakage.

C2 Seal Redesign

The original seals used in this design were quad seals and have the cross section shown in Figure C4.

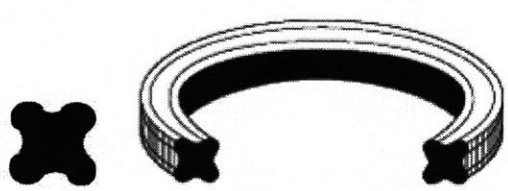

Figure C4. Quad seal cross section

In order for the seals to contact a maximum amount of surface, they must be deformed, which will increase the force between the vane and the motor wall. One of the problems with the

previous seal design was that it did not adequately compress the seals, which did not provide an a large enough sealing area.

Seals are available in almost infinite shapes and materials, but in order to maximize the sealing area under a given force, a hollow cross section is able to provide the necessary compliance with less force than a solid seal (Figure C5).

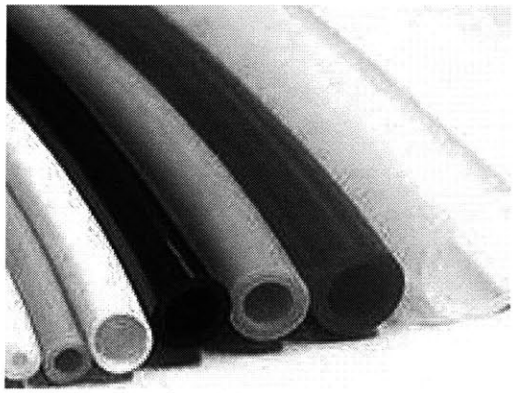

Figure C5. Seals with a hollow cross section

Sample hollow cross-section seals were obtained from Parker Hannifin's o-ring division and both silicone and nitrile were chosen for their compatibility with water and antifreeze and able to operate in temperatures up to 200°F, which is much higher than what will occur in the motor. These seals ranged in hardness from 60 to 70 Shore A, had outer diameters between 0.056" and 0.070". Figure C6 shows the sample seal leakage rates compared to the quad seal between 2 and 15 psi (0.01 – 0.1 MPa). All testing was completed using the 1:1 filtered water and antifreeze mixture.

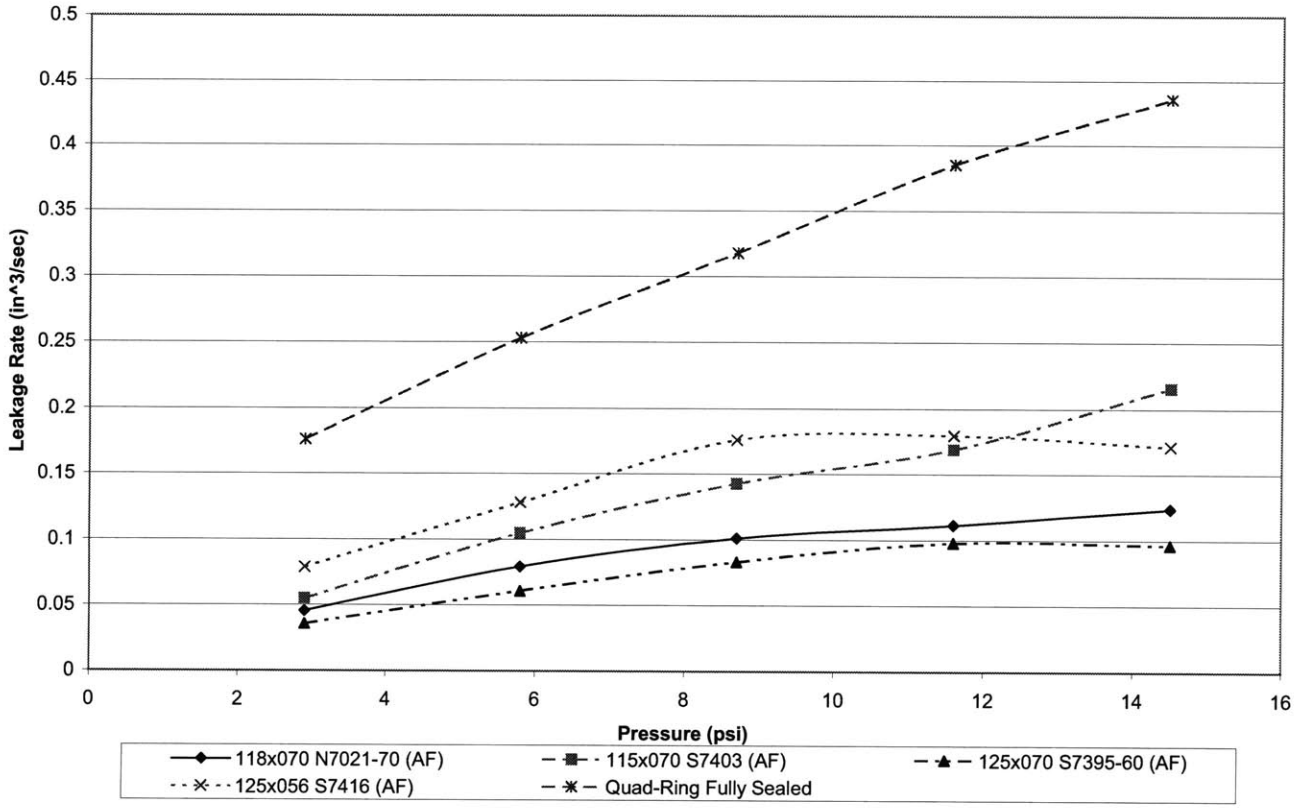

Figure C6. Hollow seal preliminary leakage tests.

Even before the seal glands were redesigned specifically for the dimensions of the new seals, the hollow seals have reduced the leakage rate by a factor of 2 to over 4.5 times. The silicone seal with an outer diameter of 0.070 inches and the softer durometer of 60 Shore A reduced the leakage the most and will be used in future experiments. These hollow seals were only used around the vane and stop and the redesign of the glands for all seals will be addressed for the next test.

In order to ensure that the seals around the vane, stop, shaft, and face seal were re-sized to provide the correct amount of deformation, the seal glands must be appropriately dimensioned and toleranced. This was done according to the Parker O-ring Handbook and Figure C7 shows the recommended design of the shaft and face seals. These seal glands are purposely undersized so that the seal is compressed 12%.

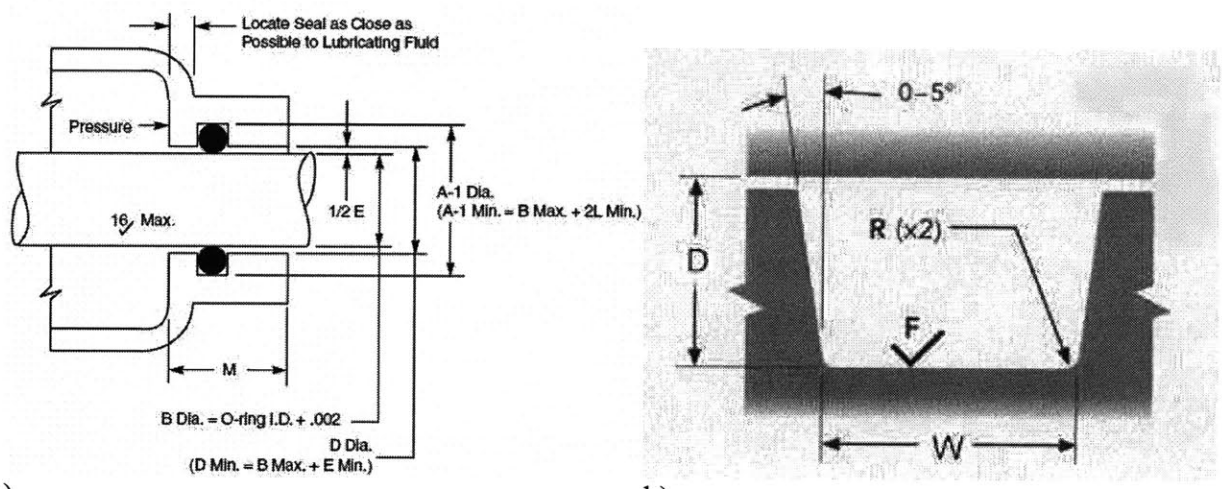

a) b)

Figure C7. Parker o-ring gland design specifications, a) shaft seal, b) face seal

Another area for redesign is the face seal on the shaft. Since this area was observed to have a high amount of leakage, redesigning this seal may be a solution. Figure C8 shows both the original configuration with a face seal and the proposed configuration with a wider vane and stop. Removing the face seal may also reduce the amount of rotary friction. Both configurations will be tested with hollow seals and new shaft seals.

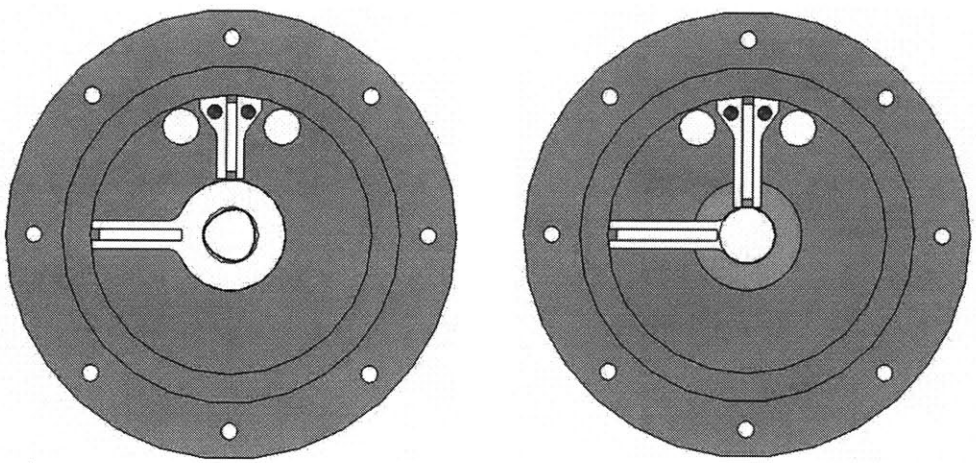

a) b)

Figure C8. Motor with, a) face and shaft seal, and b) only shaft seal

C3 Leakage and Friction Testing

The redesigned seal glands and both with and without a face seal were tested. Figure C9 shows the leakage rates for the configurations with and without the face seal.

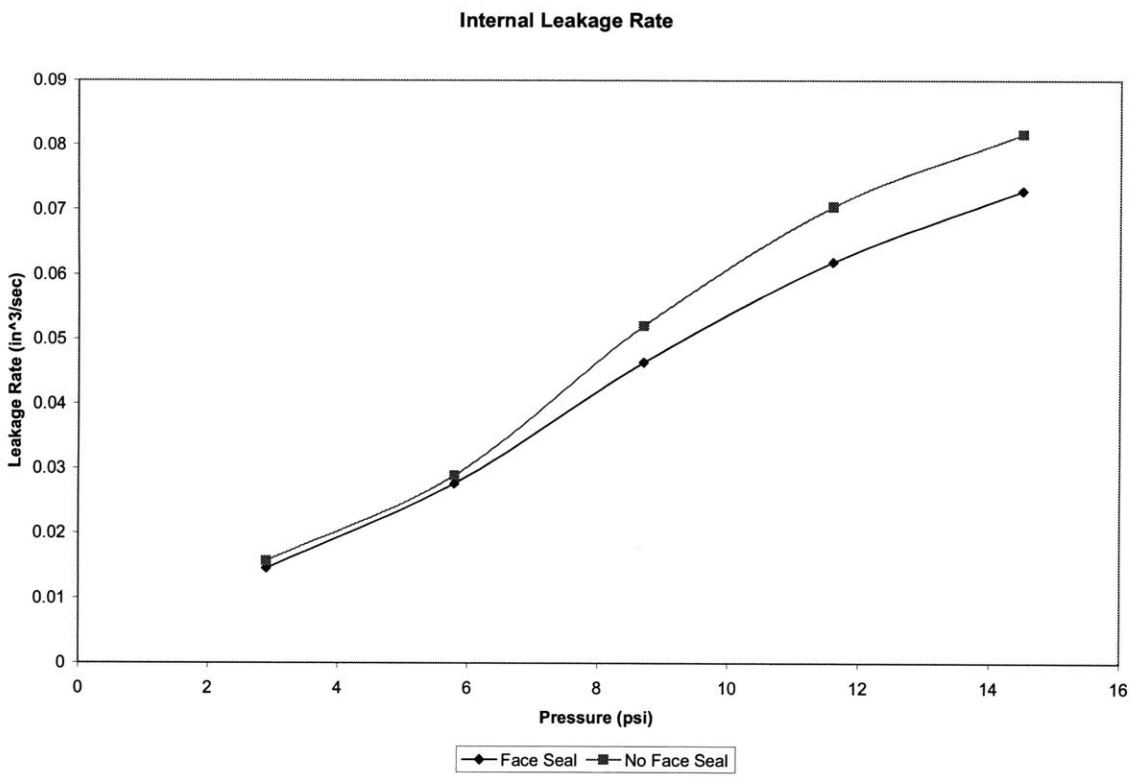

Figure C9. Internal leakage rates for redesigned seal glands.

Over this pressure range, both configurations are very comparable, with the face seal performing slightly better as the pressure increases. Table C1 shows the leakage rates at the predicted maximum of 32.4 psi (0.22 MPa) for the original design with quad seals, and the two redesigned configurations. These rates were interpolated from the test data using linear best fit with R values of 0.993, 0.997, and 0.994 respectively for the original design, the redesigned face seal, and the elimination of the face seal.

Configuration	Leakage Rate (in^3/sec)	Leakage Rate (cups/min)
Quad Ring	4.068	16.9
Face Seal	0.168	0.697
No Face Seal	0.172	0.713

Table C1. Leakage rates for sealing configurations.

Figure C10 shows the tested redesigned motor with hollow seals.

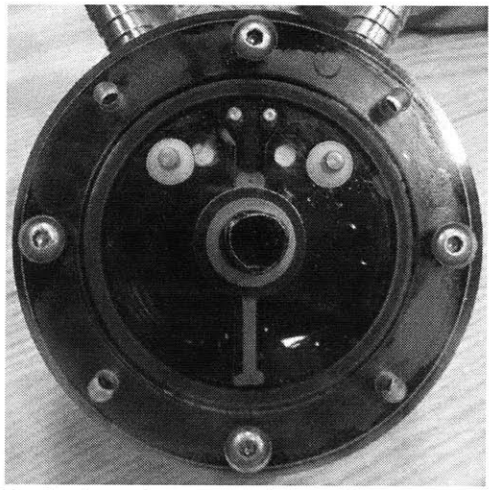

Figure C10. Redesigned motor with hollow seals and face seal.

The original design has a leakage rate of over 16 cups a minute which is over one gallon! Torque would not be able to be transmitted with this amount of leakage. Both the redesigned configurations leak less than 1 cup per minute, and their leakage rates are smaller by a factor of 24.2 and 23.7 respectively. The new seals were also tested up to 40 psi (0.28 MPa) to ensure that the shaft seals were able to withstand the pressure and prevent external leakage. No external leakage was detected. Next is to test if this significant reduction in leakage rate had a negative effect on the rotary friction.

The rotary friction was testing using the brushless 640 VDC Kollmorgen motor originally chosen to drive the rotary motors. All tests were completed with generous coating of Parker Super O-Lube on all seals. The test rotated the vane 120° both clockwise and counterclockwise from 1.5 rad/sec to 4.5 rad/sec. Figure C11 shows the resulting torque required to overcome the rotary friction.

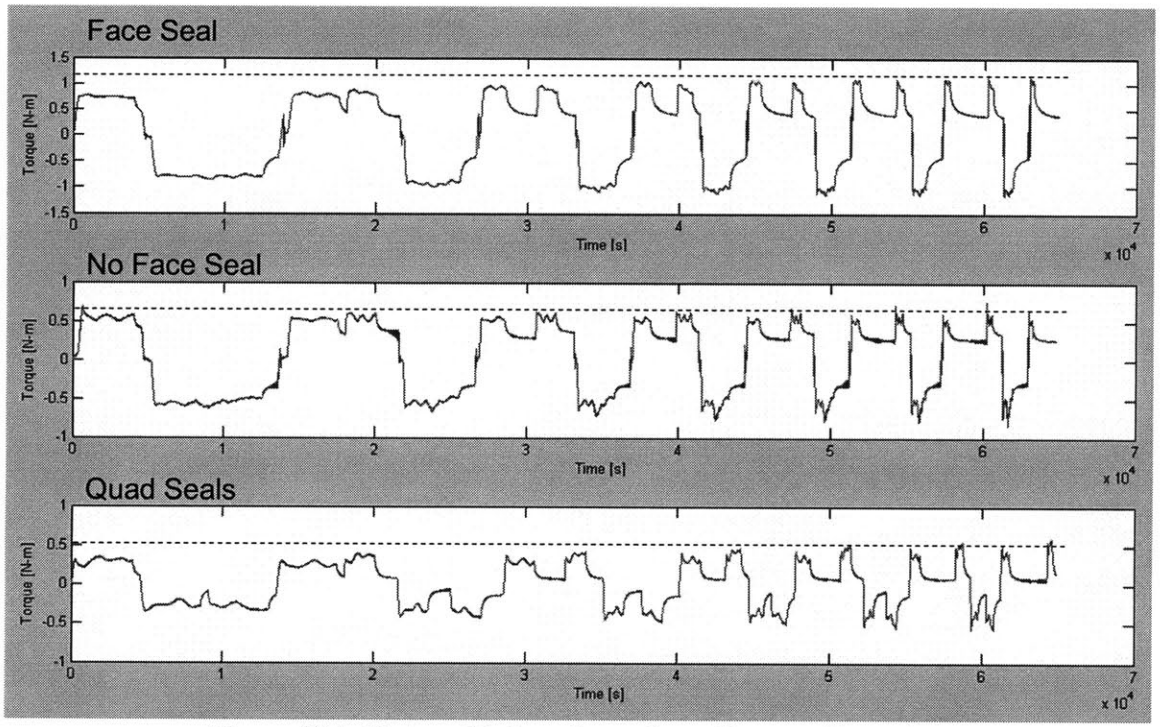

Figure C11. Rotary friction for each sealing configuration

The quad seals required a maximum torque of 4.4 in-lb (0.5 Nm), the redesigned motor with no face seals required about 5.49 in-lb (0.62 Nm), and the redesigned motor with face seals required about 10.6 in-lb (1.2 Nm). Removing the face seals did greatly reduce the friction with only a slight increase in leakage and the friction is very comparable to the original quad seal with about 24 times less internal leakage.

The redesigned motor with no face seal was also tested with the motor full of liquid to provide a more accurate measure of the total rotary friction, since the inertia of the fluid will increases the torque required. Figure C12 shows both the "dry" and "wet" test results.

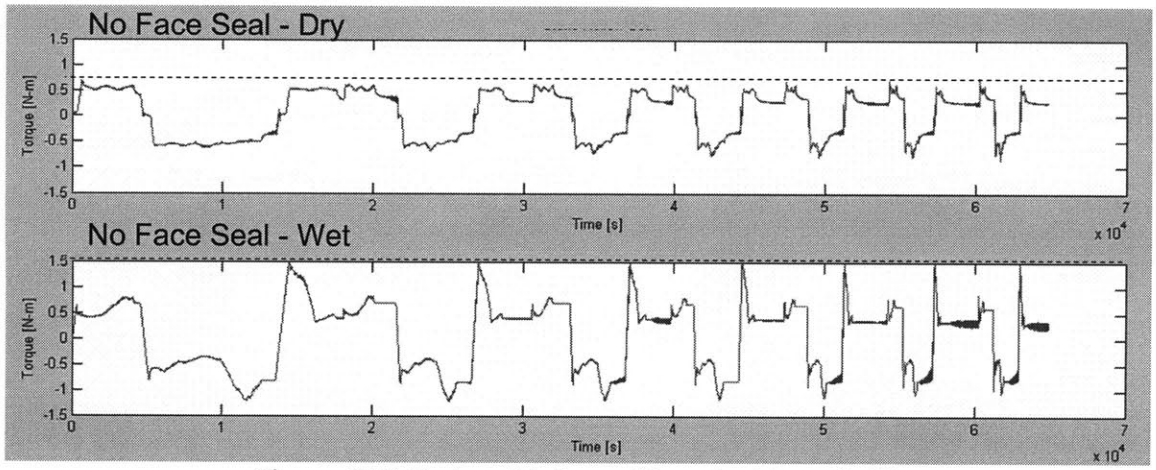

Figure C12. Rotary friction with and without fluid.

The addition of the fluid about doubled the torque required to 13.3 in-lb (1.5 Nm). This may impede natural wrist movements.

C4 Phantom Testing

In order for the wrist robot to be able to be used in an MRI, it not only cannot include ferrous materials which would be attracted to the magnet, but also the materials must not distort the MRI image. The current motor is made of 6061 aluminum and is black anodized. It was taken to a 4 Tesla MRI at McLean Hospital and a phantom test was completed.

A phantom is a volume of known shape and size filled with a fluid designed to approximate human tissue, commonly 1.24 g $NiSO_4 \times 6\ H_2O$/ 2.62 NaCl per 1000 g H_2O [3]. It is often used to assess the image quality of an MRI or for calibration. A spherical phantom, like the one in Figure C13, was used in this experiment.

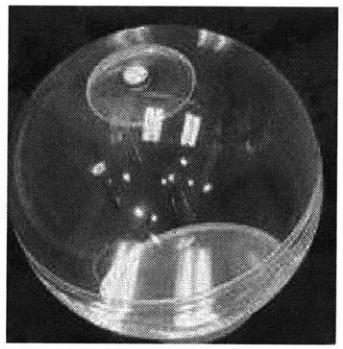
Figure C13. Typical phantom for MRI [3].

Three sets of images were taken: the first with only the phantom as a control, the second with the motor located 27 inches from the phantom along the MRI table, and third with the motor touching the phantom. The 27 inch distance was chosen as the approximate length between the head and hand of the 1% female, which would be the closest the motor would be to the subject's head while in use.

Matlab was used to process the images. The "imsubtract" command was used to compare the sagittal slice images taken when the motor was 27 inches from the phantom and touching the phantom to the control image (Figures C14 – C16). The dark circle that appears beginning in the third row of the control image in Figure C14 is an air bubble in the phantom fluid and does not indicate image distortion. If the subtracted image is completely black, that indicates that there is no difference or distortion of the image.

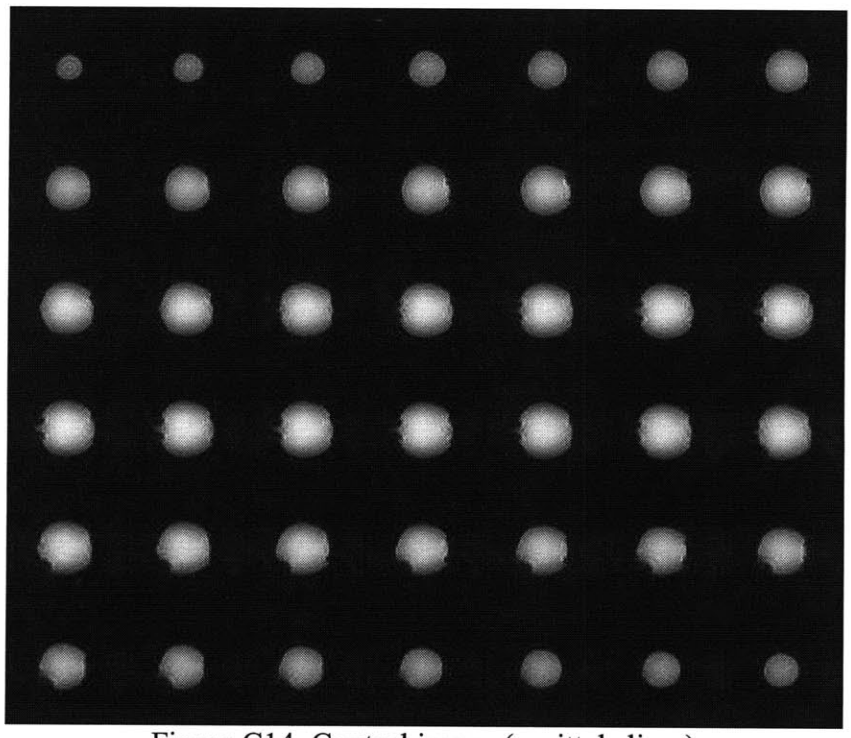

Figure C14. Control image (sagittal slices)

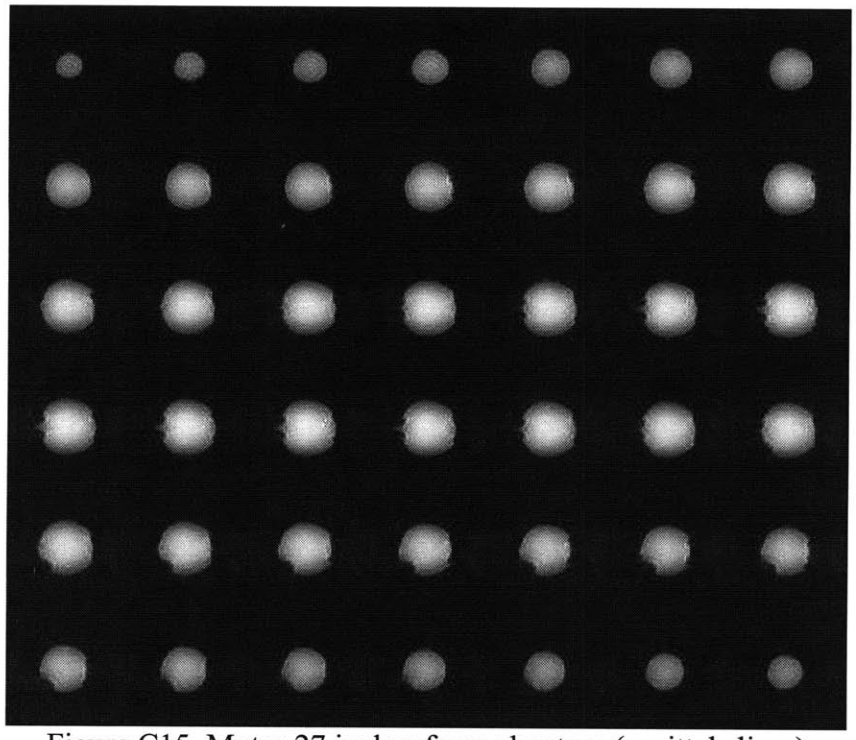

Figure C15. Motor 27 inches from phantom (sagittal slices)

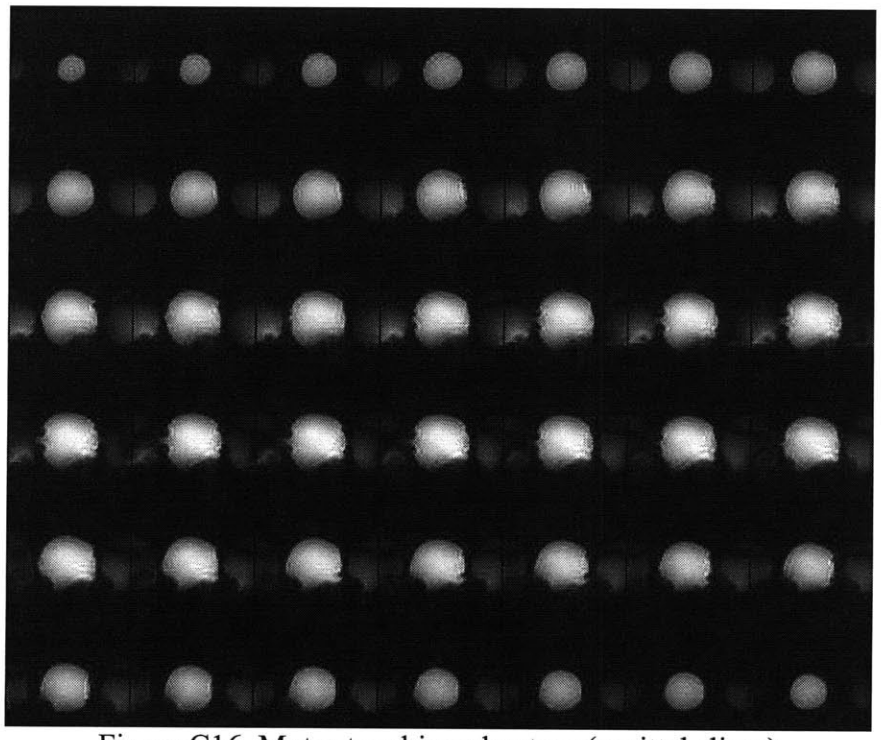

Figure C16. Motor touching phantom (sagittal slices)

Figures C17 and C18 show the subtracted images for the 27 inch distance and motor touching respectively. The completely black area for the distance of 27 inches shows that the material

selection of aluminum is acceptable at this distance. The distortion seen in Figure C18 when the motor is touch the phantom is not surprising. Even though aluminum is non-ferrous, the powerful magnetic field would be capable of producing eddy currents in the material. The dark shadows the block out sections of the sphere can be seen beginning by the end of the second row indicate an area of the image that was completely blocked by the motor.

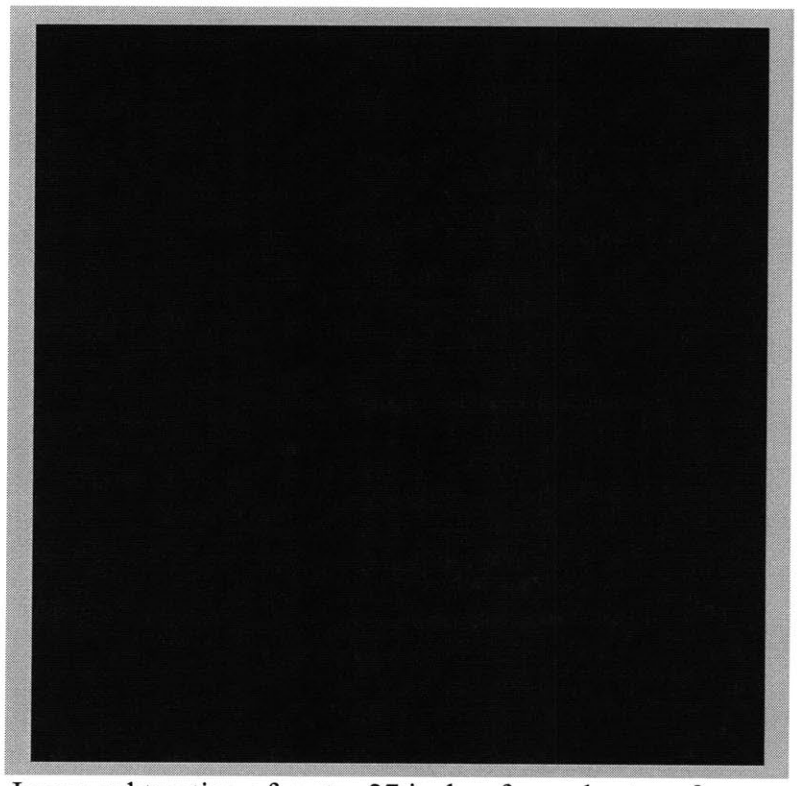

Figure C17. Image subtraction of motor 27 inches from phantom from control image.

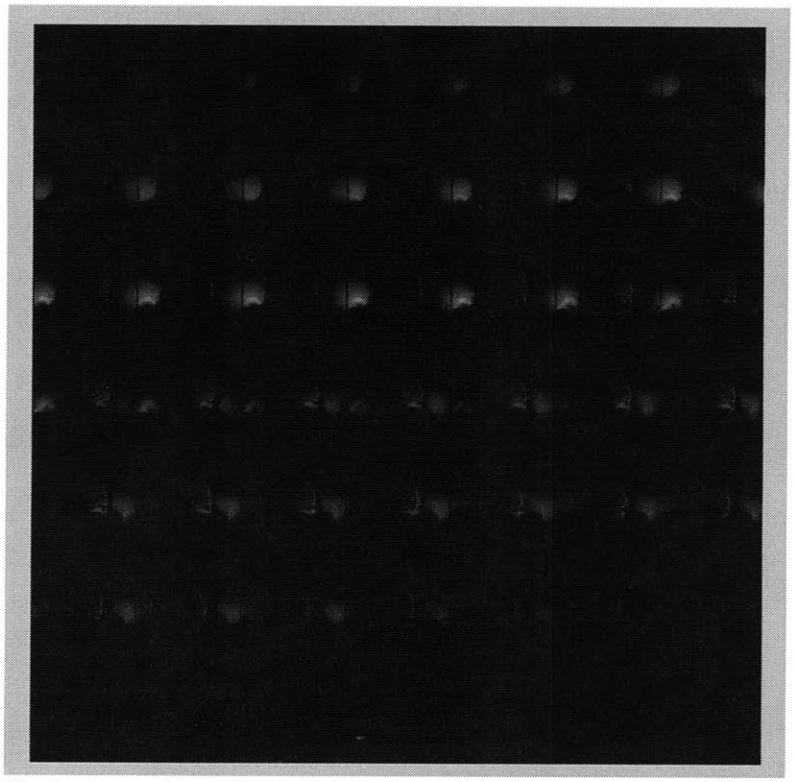

Figure C18. Image subtraction of motor touching phantom from control image.

C5 Conclusions

The redesign of the seal reduced the internal leakage rate by about 24 times without increasing the friction. If this hydraulic design is continued, a redesign of the inside of the motor with a larger radius where the vane and wall meet (circled in Figure C19) may reduce the leakage seen at the current sharp corners which are difficult to seal.

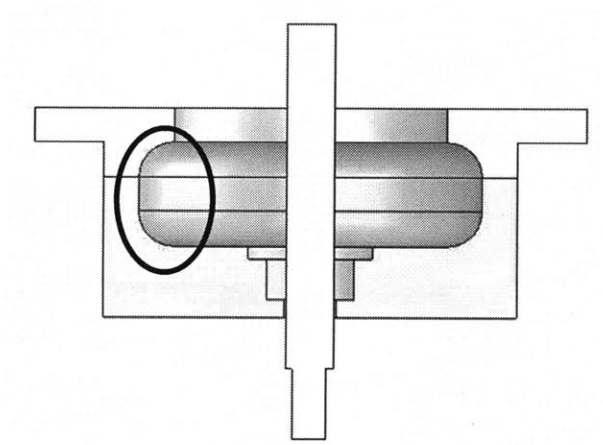

Figure C19. Proposed design with larger internal radii.

The current material selection is adequate and does not cause any image distortion at the shortest expected operating distance. This is a positive find because 6061 aluminum is straight forward to machine and readily available. If this device is used with a child, further testing is required to determine the absolute shortest acceptable distance from the image center. Also, extended testing should be done to ensure that the motors do not become uncomfortably hot due to eddy currents that are induced in the material.

Although the seal redesign significantly reduced the internal leakage, it must be further reduced while also decreasing the rotary friction. The system may be able to tolerate a level of internal leakage if it is recalibrated once during the testing to account for any vane misalignment. Because of the design conflict between seals and rotary friction, it may not be possible to achieve an acceptable balance. Additional designs that would not be sensitive to internal leakage, including a linkage driven by fluid filled bellows, should be considered.

Appendix C References

[1] Mendelowitz, S.E. *Design of an MRI Compatible Robot for Wrist Rehabilitation.* MSME Thesis, Massachusetts Institute of Technology, June 2005.

[2] Hanumara, N.C. *Characterization and Analysis of an MRI Compatible Robot Design for Wrist Psychophysics and Rehabilitation.* MSME Thesis, Massachusetts Institute of Technology, June 2006.

[3] Basics of MRI. [Online] http://www.cis.rit.edu/htbooks/mri/chap-9/chap-9.htm#9.8. Accessed November 2008.